

## INFORMATION TO USERS

This manuscript has been reproduced from the microfilm master. UMI films the text directly from the original or copy submitted. Thus, some thesis and dissertation copies are in typewriter face, while others may be from any type of computer printer.

The quality of this reproduction is dependent upon the quality of the copy submitted. Broken or indistinct print, colored or poor quality illustrations and photographs, print bleedthrough, substandard margins, and improper alignment can adversely affect reproduction.

In the unlikely event that the author did not send UMI a complete manuscript and there are missing pages, these will be noted. Also, if unauthorized copyright material had to be removed, a note will indicate the deletion.

Oversize materials (e.g., maps, drawings, charts) are reproduced by sectioning the original, beginning at the upper left-hand corner and continuing from left to right in equal sections with small overlaps.

ProQuest Information and Learning  
300 North Zeeb Road, Ann Arbor, MI 48106-1346 USA  
800-521-0600

UMI<sup>®</sup>

**University of Alberta**

**Experimental Investigation of Two Techniques to Reduce  
Limited Field-of-View Artifacts in Computed Tomography**

by

Anna Theresa Kress



A thesis submitted to the Faculty of Graduate Studies and Research in  
partial fulfillment of the requirements for the degree of Master of Science

in

**Medical Physics**

**Department of Physics**

**Edmonton, Alberta**

**Spring 2005**



Library and  
Archives Canada

Bibliothèque et  
Archives Canada

Published Heritage  
Branch

Direction du  
Patrimoine de l'édition

395 Wellington Street  
Ottawa ON K1A 0N4  
Canada

395, rue Wellington  
Ottawa ON K1A 0N4  
Canada

*Your file* *Votre référence*

*ISBN:*

*Our file* *Notre référence*

*ISBN:*

**NOTICE:**

The author has granted a non-exclusive license allowing Library and Archives Canada to reproduce, publish, archive, preserve, conserve, communicate to the public by telecommunication or on the Internet, loan, distribute and sell theses worldwide, for commercial or non-commercial purposes, in microform, paper, electronic and/or any other formats.

The author retains copyright ownership and moral rights in this thesis. Neither the thesis nor substantial extracts from it may be printed or otherwise reproduced without the author's permission.

**AVIS:**

L'auteur a accordé une licence non exclusive permettant à la Bibliothèque et Archives Canada de reproduire, publier, archiver, sauvegarder, conserver, transmettre au public par télécommunication ou par l'Internet, prêter, distribuer et vendre des thèses partout dans le monde, à des fins commerciales ou autres, sur support microforme, papier, électronique et/ou autres formats.

L'auteur conserve la propriété du droit d'auteur et des droits moraux qui protègent cette thèse. Ni la thèse ni des extraits substantiels de celle-ci ne doivent être imprimés ou autrement reproduits sans son autorisation.

In compliance with the Canadian Privacy Act some supporting forms may have been removed from this thesis.

Conformément à la loi canadienne sur la protection de la vie privée, quelques formulaires secondaires ont été enlevés de cette thèse.

While these forms may be included in the document page count, their removal does not represent any loss of content from the thesis.

Bien que ces formulaires aient inclus dans la pagination, il n'y aura aucun contenu manquant.

  
**Canada**

*for Aaron*

# Abstract

Computed tomography (CT) truncation artifacts caused by a limited field-of-view (FOV) can be reduced by merging two truncated fan-beam sinograms or by augmenting a truncated parallel-beam sinogram with estimates derived from an iterative procedure. To experimentally test these techniques, axial and spiral fan-beam sinograms of a phantom were acquired from a Picker PQ5000 CT scanner with the phantom positioned left and right of isocenter (for merging) and at the center (for augmenting). Fan-beam sinograms were artificially truncated to smaller FOVs. For the merging technique, the effect of positioning errors in the shift and longitudinal directions was investigated. Images reconstructed from the merged or augmented sinograms were compared to images reconstructed from non-truncated sinograms. Qualitative analysis consisted of viewing the images and comparing profiles through the images. Quantitative comparisons of images were also performed. For both axial and spiral data, both techniques substantially reduced the artifacts produced by the limited FOV.

# Acknowledgements

Thank you to my supervisors Dr. Hooper and Dr. Fallone for the opportunity to work on two very interesting and unique projects. I thank Dr. Hooper for his guidance, patience, and kindness throughout this work as well as his expertise in the techniques. I thank Dr. Fallone for all the work he has done in making the Medical Physics program at the University of Alberta an excellent one. I would also like to thank Murray Ingram and Dr. Robinson for their help in obtaining the raw data from the CT scanner. Without the raw data, there would not have been much of an experimental investigation.

I am so lucky to have made such wonderful friends during my studies here. Keith, thank you for always motivating me to get the job done. You amaze me with your ability to successfully deal with school and a growing family. Tara, thank you for your wonderful sense of humor and honesty. Steven, thank you for your creativity and willingness to help others with their projects. Your energy and enthusiasm is wonderful to be around. Lesley, thank you for planning fun activities for the group and for being the interesting exciting person that you are. Amr, thank you for always smiling and making us laugh. Also thank you to the many other awesome friends that I have made here including: Erin, Deluan, Alana, Sandra, Keith W., and Alasdair. Thank you for making my time here enjoyable and for being such great friends!

Thank you to my Mom and Dad for their support during my undergraduate studies. And thank you for 'cutting me off' when I decided to continue on to graduate studies. I appreciate all that you have done for me as a child, a teenager, and as an adult. To my sister, Melanie, thank you for being my best friend. Tommy, thank you for being such a great brother and friend.

And for Aaron, thank you for making everyday so special to me. Thank you so much for all your help, love, support, and advice. Also, thank you for all of those wonderful dinners you made for me while I was busy studying (or busy relaxing). Everyday, because of you, I smile, laugh, and love. Thank you.

# Table of Contents

<b>1</b>	<b>Thesis Overview .....</b>	<b>1</b>
<b>2</b>	<b>Background .....</b>	<b>5</b>
2.1	Reconstruction .....	5
2.1.1	Fourier Slice Theorem .....	6
2.1.2	Filtered Backprojection.....	9
2.1.2.1	Three-Dimensional Objects .....	12
2.1.2.2	Data Sufficiency Conditions .....	16
2.1.3	Maximum-Likelihood Expectation-Maximization .....	16
2.1.3.1	Ordered Subsets .....	21
2.2	Limited Projection Data.....	22
2.2.1	Limited-angle.....	24
2.2.1.1	Iterative Transform Methods .....	24
2.2.1.2	Shorter-Scan Filtered Backprojection.....	25
2.2.2	Limited-detector.....	25
2.2.2.1	Truncated detector data.....	26
2.2.2.1.1	Extrapolation.....	26
2.2.2.1.2	Local Tomography.....	27
2.2.2.1.3	Sinogram Augmentation .....	27
2.2.2.1.4	Offset Detector.....	28
2.2.2.1.5	Region-of-Interest Tomography .....	28
2.2.2.2	Missing detector data .....	29
2.2.2.2.1	Iterative Transform Methods .....	29
2.2.2.2.1.1	Constrained Fourier Reconstruction .....	29
2.2.2.2.1.2	Iterative Reconstruction Reprojection .....	30
2.2.2.2.2	Interpolation.....	31
2.2.3	Iterative Optimization Algorithms.....	31
2.2.3.1	Image Space Reconstruction Algorithm .....	32
2.3	Reconstruction of truncated detector data.....	32
2.3.1	Sinogram Merging .....	34

2.3.1.1	Net FOV.....	38
2.3.1.2	Phase Angle .....	39
2.3.2	Iterative Sinogram Augmentation.....	41
	References.....	44
<b>3</b>	<b>Materials and Methods.....</b>	<b>49</b>
3.1	Experimental Setup.....	50
3.1.1	Geometrical Parameters .....	50
3.1.2	Picker Sinogram File Format.....	53
3.1.3	Phantom .....	55
3.2	Data Preprocessing.....	57
3.3	Data Acquisition and Processing .....	60
3.3.1	Reference and Truncated Images.....	61
3.3.2	Sinogram Merging .....	61
3.3.2.1	Lateral Offset Distances.....	63
3.3.3	Iterative Sinogram Augmentation.....	64
3.3.3.1	Number of subsets.....	65
3.4	Analysis.....	66
	References.....	66
<b>4</b>	<b>Results and Discussion.....</b>	<b>69</b>
4.1	Experimental Setup and Parameters .....	69
4.1.1	Source-to-Axis Distance .....	69
4.1.2	Calibration Curve.....	71
4.2	Axial Results.....	72
4.2.1	Analysis.....	78
4.2.1.1	Profiles .....	78
4.2.1.2	Quantitative Analysis.....	80
4.2.1.3	Number of Subsets.....	81
4.2.2	Sinogram Merging Technique – Artifacts .....	83
4.2.2.1	General Artifacts.....	83
4.2.2.2	Positioning Error.....	83
4.2.2.3	Stationary Couch.....	85



4.2.3	Improving the Image.....	87
4.3	Spiral Results .....	88
4.3.1	Analysis.....	91
4.3.1.1	Profiles .....	91
4.3.1.2	Quantitative Analysis.....	91
4.3.2	Positioning Error.....	97
4.4	General Comments.....	101
	References.....	102
<b>5</b>	<b>Conclusions.....</b>	<b>103</b>
	<b>Bibliography .....</b>	<b>107</b>

# List of Tables

Table 2-1 – Summary of notation used in emission CT model. ....	17
Table 2-2 – Notation used to describe the fan-beam to parallel-beam merging procedure.....	36
Table 2-3 – List of input and output parameters required for fan-beam to parallel-beam merging algorithm. ....	38
Table 2-4 – List of notation used in the iterative sinogram augmentation technique.....	44
Table 3-1 – Geometrical parameters for Picker PQ5000 CT scanner .....	51
Table 3-2 – List of material used in the CIRS phantom 002LFC and their position in the phantom according to the labels in Figure 3-7.....	57
Table 4-1 – The image goodness-of-fit (GOF) and Bias measures for each type of axial image: truncated, merged, and augmented. The measures are calculated in a defined region, which is outlined in Figure 4-4, for each field-of-view (FOV): 24, 22, and 20 cm.....	81
Table 4-2 – The goodness-of-fit (GOF) and Bias measures for sagittal and coronal slices: truncated, merged, and augmented, at each pitch. The measures are calculated in a 19.5 cm wide x 10 cm high rectangular defined region, which is centered in the image.....	97
Table 4-3 – The image goodness-of-fit (GOF) and Bias measures for merged sagittal and coronal images with minimal positioning error, 2 mm lateral ( $x$ -direction) error, and 2 mm longitudinal ( $z$ -direction) error. The measures are calculated in a 19.5 cm wide x 10 cm high rectangular defined region, which is centered in the image.....	100

# List of Figures

Figure 2-1 – An object  $\mu(x, y)$  and its parallel projection,  $\lambda_\theta(t_1)$ , for an angle  $\theta$ . 6

Figure 2-2 – The Fourier Slice Theorem relates the one-dimensional Fourier transform of a projection to a slice in the two-dimensional Fourier transform of the object..... 8

Figure 2-3 – A fan projection  $R_\beta(\gamma)$  for an angle  $\beta$ . Each ray is given by its angle  $\gamma$ , measured from the central ray..... 12

Figure 2-4 – Linear interpolation (LI) algorithms in spiral CT. The couch increment per  $360^\circ$  source rotation is denoted by  $d$ . (a)  $360^\circ$  LI uses points  $z'$  and  $z'+d$  to estimate a point in planar geometry at  $z_u$ . (b)  $180^\circ$  LI uses points  $z''$  and  $z'+d$  to estimate  $z_u$ . Dashed line data is  $180^\circ$  apart, in the parallel angle  $\theta$ , from the solid line data..... 15

Figure 2-5 – For emission CT reconstruction, the image plane is divided into discrete source distribution pixels  $s_j$ , and the total number of photons are recorded at projection  $y_j$ ..... 17

Figure 2-6 – Illustration of limited-angle. The black dots denote the location of the x-ray source for each projection. The detector is assumed to be across from the x-ray source as in Figure 2-7. (a) Full  $360^\circ$  data available. (b) Limited angular data available..... 23

Figure 2-7 – Illustration of limited-detector. (a) Full extent of the object is visible in each projection. (b) Only a region inside the object is visible in each projection. Limited-detector may be a result of x-ray source collimation or reduced x-ray detector coverage..... 23

Figure 2-8 – The multileaf collimator (MLC) in tomotherapy limits the field-of-view (FOV) to 40 cm. The limited FOV of this system is defined by the x-ray source collimation not by the detector array. A special feature of this machine is that the detector array is focused on a point 18 cm below the x-ray source, rather than on the source as in most 3<sup>rd</sup> generation scanners. .... 34

Figure 2-9 – Overview of sinogram merging technique. (a) Scan the phantom at left and right offset locations. White circle indicates scanning FOV. (b) Acquire the truncated fan-beam sinograms and merge into a single parallel-beam sinogram in (c). Apply filtered backprojection to the parallel-beam sinogram to reconstruct an axial image (d). Net FOV is shown in (d). ..... 35

Figure 2-10 – Geometry of the fan-beam to parallel-beam merging procedure. The variables are defined in Table 2-2. .... 36

Figure 2-11 – Net FOV in sinogram merging technique. Dotted lines are FOVs for each individual scan and solid black line is net FOV in sinogram merging technique. Parallel-beam ray paths that intersect at a point,  $x$ , are shown as gray lines and  $180^\circ$  of parallel-beam data is required to reconstruct this point or any point. (a) Two overlapping FOV circles with net FOV outlined. (b) Two touching FOV circles with net FOV outlined. (c) Separate FOV circles, no net FOV. .... 39

Figure 2-12 – Effect of object shift distances  $(x_c, y_c)$  and phase angle  $\phi$  on measured projection data. Data at fan-beam source angles  $\beta$  is plotted as a function of parallel-beam offset  $t$  for a parallel-beam projection angle  $\theta = 30^\circ$  for a 40 cm object. (a)  $(x_c = 0 \text{ cm}, y_c = 0 \text{ cm})$  and  $\phi = 0^\circ$ . (b)  $(x_c = \pm 5 \text{ cm}, y_c = 0 \text{ cm})$  and  $\phi = 0^\circ$ . (c)  $(x_c = \pm 5 \text{ cm}, y_c = 0 \text{ cm})$  and  $\phi = 90^\circ$  ..... 41

Figure 2-13 – Overview of iterative sinogram augmentation technique. Use the start value model (a) to estimate a parallel-beam sinogram (b). Calculate the image (c) from the estimated sinogram (b) and the measured truncated sinogram (d) using the OS-ML-EM algorithm. (e) Iteratively apply the algorithm, going back and forth between the estimated sinogram and the image. A non-truncated parallel-beam sinogram (f) is estimated when iterations are complete. Copy the portion of (f) that is missing in (d) to form the augmented sinogram (g). Apply filtered backprojection to (g) to reconstruct an axial image (h). .... 42

Figure 3-1 - Geometry of a fourth generation CT scanner. The diameter of a circle at the axis, subtended by the fan-beam, is the field-of-view (FOV)... 51

Figure 3-2 – Setup used to determine source-to-axis distance ( $d$ ). Variables are described in the text. ....	52
Figure 3-3 – File format of Picker sinogram file. The number of 16-bit integers is indicated. ....	53
Figure 3-4 – A fan-beam in the Picker scanner. The diameter of the field-of-view (FOV) is 51 cm and is 1104 detectors wide. The direction of source rotation is counter clock-wise. The fixed locations of four of the 4800 detectors are shown. The source start angle $\beta_0$ can be determined from these fixed detector locations. ....	54
Figure 3-5 – CIRS phantoms used for collecting experimental data. Model (a) 002H5 (b) 002LFC. ....	55
Figure 3-6 – Acrylic plugs with variable step widths (2.0 cm, 1.0 cm, and 0.5 cm). These were used in spiral scans. Units are in cm. ....	56
Figure 3-7 – CIRS phantom 002LFC indicating arrangement of contrast plugs used for axial scanning. ....	57
Figure 3-8 – Frequency response of filters. ....	60
Figure 3-9 – Start value model used in iterative sinogram augmentation technique. The outer boundary is approximately the same as the CIRS phantom. The values inside the boundary are 1000 (HU plus 1000) and zero outside. ....	65
Figure 4-1 – Determination of source-to-axis distance, $D$ , by measuring the magnification, $M$ , of a known length of wire on film at a distance $r$ away. ....	70
Figure 4-2 – Effect of varying source-to-axis distance $D$ . Images are the difference between our image at a given $D$ and the Picker image. (a) $D = 62.9$ cm (b) $D = 64.5$ cm. ....	71
Figure 4-3 – The calibration curve derived from comparing our normalized image to the Picker image. Note that the error bars in the $x$ - and $y$ -axes are too small to see. ....	72
Figure 4-4 – Reference image of the CIRS 002LFC phantom positioned at the axis. The rectangular outline defines the region used in quantitative analysis. ....	74

Figure 4-5 – Truncated images for FOVs of (a) 24 cm (b) 22 cm and (c) 20 cm. Images are shown in a window of 400 and level of 1000 (HU + 1000). ..... 75

Figure 4-6 – Merged images for FOVs of (a) 24 cm (b) 22 cm and (c) 20 cm. (d)-(f) same as (a)-(c) but overlaid with net FOV. The offset distance is  $\pm 3.94$  cm. Images are shown in a window of 400 and level of 1000 (HU + 1000). ..... 76

Figure 4-7 – Augmented images for FOVs of (a) 24 cm (b) 22 cm and (c) 20 cm. (d)-(f) same as (a)-(c) but masked to FOV. Images are shown in a window of 400 and level of 1000 (HU + 1000). ..... 77

Figure 4-8 – Profiles through each axial image; reference, truncated, merged, and augmented for (a) 24 cm field-of-view (FOV), (b) 22 cm FOV, and (c) 20 cm FOV. Profiles are taken at line  $y = 255$ . ..... 79

Figure 4-9 – Sinogram goodness-of-fit ( $GOF_{\text{sinogram}}$ ) as a function of the number of full-iterations for various subsets investigated in the iterative sinogram augmentation technique. Legend indicates the number of sub-iterations per full-iteration followed by the number of sinograms rows used in each sub-iteration in parentheses. .... 82

Figure 4-10 – Artifacts produced by the sinogram merging technique. Image is a merged image,  $\pm 3.94$  cm offset and 24 cm field-of-view (FOV). Arrow points to ‘couch’ artifact. .... 84

Figure 4-11 – Artifacts produced by a lateral offset error in the sinogram merging technique. Image is a merged image,  $\pm 4.00$  cm offset and 24 cm field-of-view (FOV). Lateral error is  $\sim 0.12$  cm in total. .... 85

Figure 4-12 – Effect of the stationary couch in the sinogram merging technique. All images are merged images. Top row is 24 cm field-of-view (FOV), middle row is 22 cm FOV, and bottom row is 20 cm FOV. Transmission data normalized to (a) airscan without couch (b) airscan with couch. Images are shown in a window of 400 and level of 1000 (HU + 1000). ..... 86

Figure 4-13 – Effect of increasing the offset distance and the complementary use of iterative augmentation to sinogram merging. (a) Merged image,  $\pm 3.94$  cm offset, 20 cm field-of-view (FOV). (b) Merged image,  $\pm 5.91$  cm offset,

20 cm FOV. (c) Augmented image using parallel-beam sinogram from (a). (d) Augmented image using parallel-beam sinogram from (b). .....	88
Figure 4-14 – Sagittal slices of reference images at a pitch of (a) 2, (b) 1.5, and (c) 1.0. Images are displayed using window of 400 and a level of 1000. ....	93
Figure 4-15 – Sagittal slices of truncated images with a 20 cm FOV at a pitch of (a) 2, (b) 1.5, and (c) 1.0. Images are displayed using window of 400 and a level of 1000. ....	93
Figure 4-16 – Sagittal slices of merged images for 20 cm FOV and $\pm 5.93$ cm offset at a pitch of (a) 2, (b) 1.5, and (c) 1.0. Images are displayed using window of 400 and a level of 1000.....	94
Figure 4-17 – Sagittal slices of augmented images with a 20 cm FOV at a pitch of (a) 2, (b) 1.5, and (c) 1. Images are displayed using window of 400 and a level of 1000. ....	94
Figure 4-18 – Coronal slices of merged images at a pitch of 1.5. (a) Reference image. (b) Truncated image, 20 cm field-of-view (FOV). (c) Merged image, $\pm 5.93$ cm offset, 20 cm FOV. (d) Augmented image, 20 cm FOV. Images are displayed using window of 400 and a level of 1000.....	95
Figure 4-19 – Profiles through (a) sagittal and (b) coronal slices for each image type: reference, truncated, merged, and augmented, at a pitch of 1.5. Profile locations are illustrated in Figure 4-20. ....	96
Figure 4-20 – Profiles in Figure 4-19 are taken at line $z = 25$ and $z = 46$ for sagittal and coronal slices, respectively. ....	97
Figure 4-21 – Effect of positioning error in the sinogram merging technique. Sagittal and coronal slices at a pitch of 1.5 for merged images with (a) minimal positioning error, $\pm 5.93$ cm offset, 20 cm field-of-view (FOV), (b) 0.2 cm lateral error in right scan, and (c) 0.2 cm longitudinal error in right scan. Images are displayed using window of 400 and a level of 1000. ....	99

# List of Abbreviations

CT	Computed Tomography
DR	Defined Region
FBP	Filtered Backprojection
FOV	Field of View
GOF	Goodness of Fit
ISRA	Image Space Reconstruction Algorithm
kV	kilovoltage
LI	Linear Interpolation
mA	milliamperes
MLC	Multi Leaf Collimator
ML-EM	Maximum Likelihood-Expectation Maximization
MV	megavoltage
OS-ML-EM	Ordered Subset-Maximum Likelihood-Expectation Maximization
ROI	Region of Interest
ROIT	Region of Interest Tomography



# 1 Thesis Overview

Computed tomography (CT) is the process of reconstructing cross-sectional images of a patient from a set of projection data measured by the transmission of x-rays. The images display the spatial distribution of the x-ray attenuation coefficients within a patient. The cross-section of a patient can be reconstructed from the set of projection data using the filtered backprojection (FBP) algorithm. Most applications of CT utilize the FBP algorithm because of its speed and accuracy. The mathematical basis of FBP requires that the projection data be acquired over the full width of the patient and over a complete angular range. If these requirements are not met then the quality of the reconstructed image is reduced. Image quality in CT refers to the ability of an observer to distinguish the shape and structure of internal organs, to accurately determine tissue densities, and to detect disease.

Projection data may be truncated if the measurements cannot be made over the full width of the patient. Truncation may occur in tomotherapy based imaging because the irradiated field-of-view (FOV), the range over which projection data can be measured, is smaller than in conventional CT. For patients that exceed the FOV the measured projection data will be truncated. Commercial CT scanners typically employ an extrapolation procedure in the reconstruction algorithm to handle cases where the patient exceeds the FOV, but such procedures only perform adequately if the degree of truncation is small. If there are large amounts of truncation, which can occur in tomotherapy imaging, then better techniques for determining the missing projection data are required.

Images reconstructed from truncated projections using the method of FBP will not show the patient's full extent and pixel values within the visible image will be incorrect. In order to improve the quality of the images, the missing projection data should either be measured or estimated prior to reconstruction. This can be accomplished by the use of either the sinogram merging or the iterative sinogram augmentation technique. The first technique combines two sets

of truncated projection data to form a non-truncated set of data, while the second estimates the missing projection data.

The main goal of this thesis is to experimentally investigate the sinogram merging and the iterative sinogram augmentation techniques using raw projection data obtained from a conventional CT scanner. Although the main motivation for developing these techniques originated from the limited FOV in tomotherapy, such a system was not available for experimental work at the time of this study. This investigation includes qualitative and quantitative analysis of the improved images in comparison to images reconstructed from truncated projection data.

This thesis is organized into the following chapters.

## **Chapter 2: Background**

An overview of the relevant background material to the thesis is presented in Chapter 2. The topics include methods of reconstructing an image from a set of projection data, types of projection data (parallel and fan), details of spiral scanning, and data sufficiency conditions for FBP (angular and detector conditions). Previously published techniques for improving insufficient data in the context of the FBP conditions are reviewed in detail. Finally, the sinogram merging and iterative sinogram augmentation techniques, which this thesis experimentally investigates, are described.

## **Chapter 3: Materials and Methods**

Chapter 3 is a description of the materials and methods used in experimentally investigating the sinogram merging and iterative sinogram augmentation techniques. The experimental setup is described and includes the geometrical parameters of the CT scanner, the raw data file format, and the phantom used for generating projection data. Preliminary steps that were used to prepare the data for subsequent analysis are described. The acquisition of data and processing methods are described for each technique. A description of the qualitative and quantitative methods used in evaluating the techniques is given.

## **Chapter 4: Results and Discussion**

In Chapter 4, the experimental results of the sinogram merging and iterative sinogram augmentation techniques are presented. Axial and spiral results are evaluated qualitatively and quantitatively. The impact of positioning errors and the stationary couch on the merging technique is illustrated and discussed. The advantages and disadvantages of each technique are considered and remarks on their clinical implementation are made.

## **Chapter 5: Conclusions**

Major results of this study are summarized in Chapter 5.

No text.

# 2 Background

## 2.1 Reconstruction

In this section, the mathematical basis of CT is presented. Three methods of reconstructing a cross-sectional image of an object from a set of projection data are covered. These are the Fourier Slice Theorem, Filtered Backprojection (FBP), and Maximum Likelihood-Expectation Maximization (ML-EM).

The Fourier Slice Theorem, which relates the Fourier transform of a projection to a ray in the Fourier transform of the object, provides the foundation of CT. It is derived for parallel projection data below. The method of FBP is derived by simply rewriting the fundamental expressions of the Fourier Slice Theorem. Currently, most applications of transmission CT use FBP to reconstruct images from projections because of its accuracy and speed. As the name suggests, the projection data is first filtered and then backprojected across the image plane. Backprojection is a process in which each value in the projection data is added to all the image elements along the path that formed the projection data value.

The third reconstruction algorithm, ML-EM, iteratively reconstructs an image from a set of projection data and is based upon the Poisson probability function. This method is typically used in emission CT where the quality of the reconstructed image can be improved by incorporating the Poisson nature of decay into the reconstruction algorithm. In the context of this thesis, the ML-EM algorithm is described not as a method to reconstruct an image directly from a set of projections but rather as a method to iteratively estimate missing projection data. The iterative sinogram augmentation technique (see Section 2.3.2), one of the techniques this thesis experimentally investigates, uses the ML-EM algorithm to estimate missing projection data but then uses FBP to reconstruct the image.

## 2.1.1 Fourier Slice Theorem

A cross sectional image of an object can be obtained from a set of projections. The object is represented by a two-dimensional (or three-dimensional) distribution of x-ray attenuation coefficients,  $\mu(x, y)$ . A parallel projection is formed by combining a set of line integrals,  $\lambda_{\theta}(t)$ , for each offset location,  $t$ , at a given gantry angle  $\theta$ . The coordinate system used for collecting the projection data is shown in Figure 2-1 (Kak 1979).

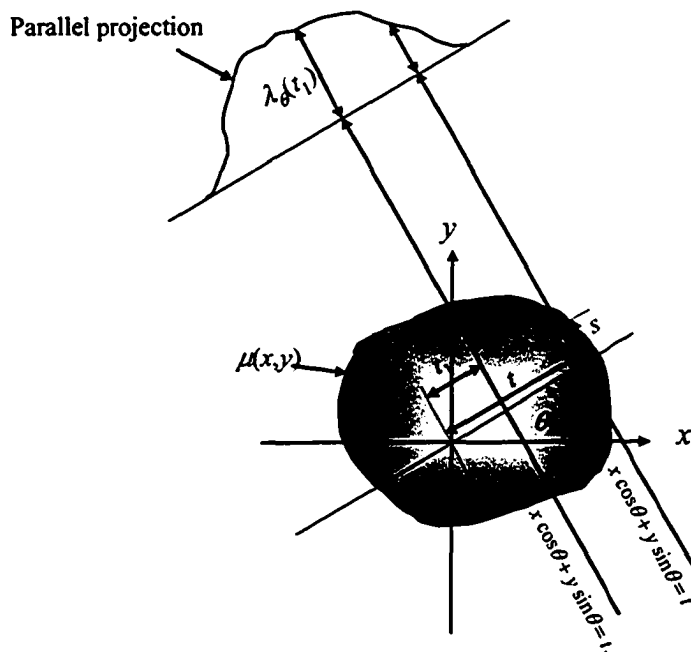


Figure 2-1 – An object  $\mu(x, y)$  and its parallel projection,  $\lambda_{\theta}(t)$ , for an angle  $\theta$ .

The stationary coordinate system,  $(x, y)$ , is transformed into a rotating coordinate system,  $(t, s)$ , using,

$$\begin{aligned} t &= x \cos(\theta) + y \sin(\theta) \\ s &= -x \sin(\theta) + y \cos(\theta) \end{aligned} \quad (2.1)$$

The line integral is defined as,

$$\lambda_{\theta}(t) = \int_{-\infty}^{\infty} \mu(t, s) ds, \quad (2.2)$$

and is known as the Radon transform of the object (Radon 1917). The Fourier Slice Theorem states that a one-dimensional Fourier transform of a parallel projection is equal to a slice of the two-dimensional Fourier transform of the object (Kak and Slaney 1987). The image of the object is then found by taking the two-dimensional inverse Fourier transform.

The two-dimensional Fourier transform of the object is defined as,

$$M(u, v) = \int_{-\infty}^{\infty} \int_{-\infty}^{\infty} \mu(x, y) e^{-j2\pi(ux+vy)} dx dy. \quad (2.3)$$

Similarly, a projection at an angle  $\theta$ ,  $\lambda_{\theta}(t)$ , and its Fourier transform is,

$$\Lambda_{\theta}(w) = \int_{-\infty}^{\infty} \lambda_{\theta}(t) e^{-j2\pi wt} dt. \quad (2.4)$$

Using the definition of a projection in the above equation gives,

$$\Lambda_{\theta}(w) = \int_{-\infty}^{\infty} \left[ \int_{-\infty}^{\infty} \mu(t, s) ds \right] e^{-j2\pi wt} dt. \quad (2.5)$$

This result is transformed into the  $(x, y)$  coordinate system by using the relationships in Eq. (2.1) giving,

$$\Lambda_{\theta}(w) = \int_{-\infty}^{\infty} \int_{-\infty}^{\infty} \mu(x, y) e^{-j2\pi w(x \cos \theta + y \sin \theta)} dx dy. \quad (2.6)$$

The above equation states that the one-dimensional Fourier transform of a projection (left-hand side) is equal to the two-dimensional Fourier transform of the object at a frequency of  $(u = w \cos \theta, v = w \sin \theta)$  (right-hand side) or,

$$\Lambda_{\theta}(w) = M(w \cos \theta, w \sin \theta) \quad (2.7)$$

and therefore proves the Fourier Slice Theorem.

The Fourier Slice Theorem is illustrated in Figure 2-2 (Pan and Kak 1983). Taking the one-dimensional Fourier transform of a parallel projection of an object  $\mu(x, y)$  acquired at an angle  $\theta$ ,  $\lambda_{\theta}(t)$ , results in a slice of the two-dimensional

Fourier transform,  $M(u, v)$ , that subtends an angle  $\theta$  with respect to the  $u$ -axis. In other words, the values of  $M(u, v)$  along the radial line  $AB$  are determined from the one-dimensional Fourier transform of  $\lambda_\theta(t)$ .

In theory, by taking projections of an object at many angles, and Fourier transforming each of these, the values of  $M(u, v)$  on radial lines are determined. The object,  $\mu(x, y)$ , is then found by taking the two-dimensional inverse Fourier transform of  $M(u, v)$ . Unfortunately, the implementation of this technique is difficult in practice as it requires interpolating from the radial points in frequency space to points on a square grid (Stark, Woods et al. 1981) and a complicated interpolation scheme is necessary to reduce errors (Walden 2000). Also, all of the projection data must be collected before image reconstruction can begin.

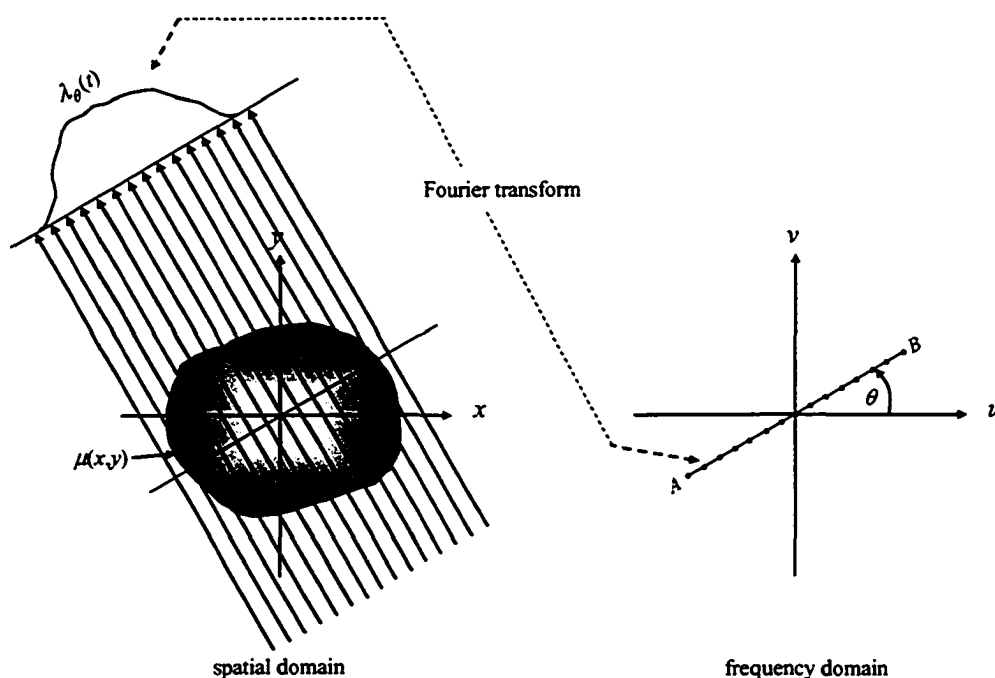


Figure 2-2 – The Fourier Slice Theorem relates the one-dimensional Fourier transform of a projection to a slice in the two-dimensional Fourier transform of the object.



## 2.1.2 Filtered Backprojection

Most applications of CT use the filtered backprojection (FBP) algorithm due to its speed and accuracy. It is derived for parallel projections using the Fourier Slice Theorem.

The inverse Fourier transform of the object is defined as,

$$\mu(x, y) = \int_{-\infty}^{\infty} \int_{-\infty}^{\infty} M(u, v) e^{j2\pi(ux+vy)} du dv. \quad (2.8)$$

This equation can be transformed from Cartesian to polar coordinates using the substitutions,

$$\begin{aligned} u &= w \cos \theta \\ v &= w \sin \theta \\ du dv &= w dw d\theta \end{aligned} \quad (2.9)$$

resulting in,

$$\mu(x, y) = \int_0^{2\pi} \int_0^{\infty} M(w, \theta) e^{j2\pi w(x \cos \theta + y \sin \theta)} w dw d\theta. \quad (2.10)$$

By considering  $\theta$  from 0 to  $\pi$  and then  $\pi$  to  $2\pi$  and using the property,

$$M(w, \theta + \pi) = M(-w, \theta) \quad (2.11)$$

Eq. (2.10) may be written as,

$$\mu(x, y) = \int_0^{\pi} \int_{-\infty}^{\infty} M(w, \theta) |w| e^{j2\pi w(x \cos \theta + y \sin \theta)} dw d\theta. \quad (2.12)$$

By the Fourier Slice Theorem in Eq. (2.7), the formula for FBP is expressed as,

$$\mu(x, y) = \int_0^{\pi} \int_{-\infty}^{\infty} \Lambda_{\theta}(w) |w| e^{j2\pi w(x \cos \theta + y \sin \theta)} dw d\theta. \quad (2.13)$$

This result may be considered to have two distinct steps,

$$Q_{\theta}(t) = \int_{-\infty}^{\infty} \Lambda_{\theta}(w) |w| e^{j2\pi w(x \cos \theta + y \sin \theta)} dw \quad (2.14)$$

and

$$\mu(x, y) = \int_0^{\pi} Q_{\theta}(x \cos \theta + y \sin \theta) d\theta. \quad (2.15)$$

The first step, Eq. (2.14), represents the filtering operation of the projection data and the second step, Eq. (2.15), represents the backprojection of the filtered data. The frequency response of the filter is  $|w|$  and is referred to as a ramp filter because of its shape. It corrects for the blurring that would otherwise appear in the reconstructed image (Redpath and Kehoe 1999). Additional filtration of the projection data may be performed to attenuate high frequency components of the projection data and reduce noise. The ramp filter is apodized, or rolled-off at high frequencies, by the additional filtration.

The equations thus far have been continuous functions representing an infinite set of projections and an infinite sampling range for each projection. In reality, the projections are formed at a finite number of angles and each projection is sampled by a finite number of detectors. Computer implementation of the FBP algorithm therefore requires digital approximations of the continuous functions. To faithfully represent the object, which is a continuous function, sampling in both the radial (number of detectors) and azimuthal (number of projections) directions need to be considered.

The method of FBP is preferred to the direct Fourier inversion method for two main reasons. The reconstruction algorithm can begin upon measuring the first projection data which increases speed and reduces the amount of data that needs to be stored at one time. Although interpolation is necessary to compute the contribution of a projection to an image point on a square matrix, a simple linear interpolation scheme is adequate whereas more complicated interpolation schemes are required for direct Fourier inversion.

The line integrals in Eq. (2.2) are determined from the law of exponential attenuation,

$$I_{\theta}(t) = I_{\theta}^0(t) \exp\left(-\int \mu(t,s) ds\right), \quad (2.16)$$

where  $I_{\theta}(t)$  is the intensity of the x-ray beam after passing through an object  $\mu(t,s)$ ,  $I_{\theta}^0(t)$  is the incident intensity,  $\theta$  and  $t$  define the position of the measurement, and  $\int \mu(t,s) ds$  is the Radon transform of the object along the path

of the beam (Swindell and Webb 1988). This represents an ideal situation where no radiation is scattered and the x-ray beam is monoenergetic and narrow. In CT,  $I(t)$  and  $I^0(t)$  are collected by the detector array at an angle,  $\theta$ , and the line integral is given as,

$$\lambda_{\theta}(t) = \int \mu(t,s) ds = \ln \frac{I_{\theta}^0(t)}{I_{\theta}(t)}. \quad (2.17)$$

By assembling a set of line integrals at many angles, the data is assembled into an array called a sinogram. The columns in the sinogram are the detectors at each distance,  $t$ , and the rows are the angles,  $\theta$ , at which the data is acquired. The value in the array is the line integral  $\lambda_{\theta}(t)$  at a particular offset  $t$  and angle  $\theta$ .

In parallel-beam geometry, which has been discussed thus far, a source-detector combination is translated over the length of a projection and then rotated by an angular interval. This translate/rotate scanning motion is repeated to acquire projection data at each angle. In all commercial CT systems, however, a fan-beam geometry is used rather than a parallel-beam geometry. A fan-beam geometry permits faster acquisition time by generating a set of line integrals (i.e. projection data) at one time. The source is collimated to form a fan that is usually wide enough to encompass the patient area and is incident on an array of detectors. The source rotates either simultaneously with the detector array (3<sup>rd</sup> generation scanner) or inside a stationary ring of detectors (4<sup>th</sup> generation scanner). The projection measurements are collected by the detector array along the divergent lines in the fan.

Figure 2-3 illustrates a fan projection which consists of a set of line integrals,  $R_{\beta}(\gamma)$  (Kak and Slaney 1987). The angles  $\beta$  and  $\gamma$  are the source and detector fan angles, respectively. The angle  $\beta$  is measured from the  $+y$ -axis and  $\gamma$  from the central ray in the fan. The maximum range of the fan angle is  $\pm\gamma_{\max}$ . Here, the line integral is defined as,

$$R_{\beta}(\gamma) = \int \mu(x,y) dl = \ln \frac{I_{\beta}^0(\gamma)}{I_{\beta}(\gamma)} \quad (2.18)$$

where  $l$  is a line in the fan-beam over which the integral is calculated.

The image from a set of fan projections  $R_{\beta}(\gamma)$  is reconstructed by first re-binning the fan projection data into an equivalent set of parallel projection data  $\lambda_{\theta}(t)$  using the relations,

$$\begin{aligned}\theta &= \beta + \gamma \\ t &= D \sin(\gamma)\end{aligned}\tag{2.19}$$

where  $D$  is the source-to-axis distance. Since these relations are non-linear, as a result of the  $\sin(\gamma)$  term, the parallel projections obtained are not uniformly sampled. A bilinear interpolation is used to estimate the parallel projection data from the fan data. After this re-binning, the FBP algorithm for parallel projection data is used to reconstruct the image. A divergent ray FBP algorithm may also be used to reconstruct images from fan projection data (Kak and Slaney 1987).

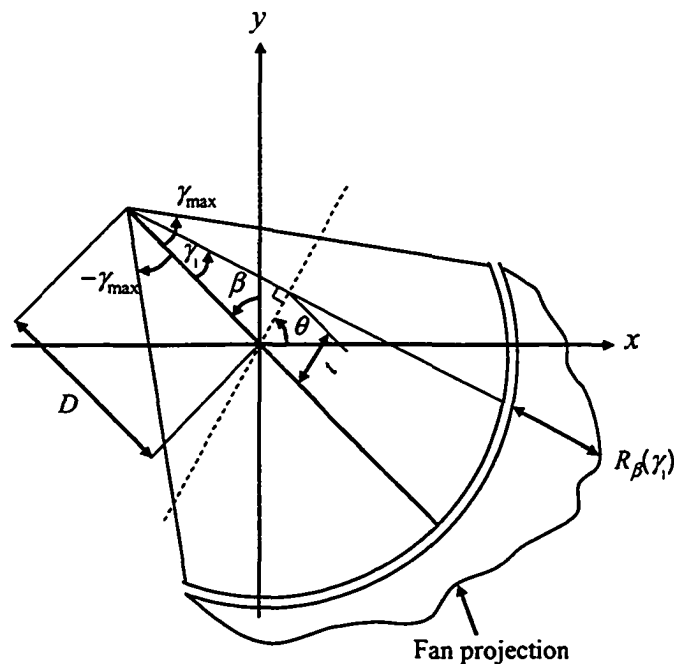


Figure 2-3 – A fan projection  $R_{\beta}(\gamma_i)$  for an angle  $\beta$ . Each ray is given by its angle  $\gamma$ , measured from the central ray.

### 2.1.2.1 Three-Dimensional Objects

To reconstruct a three-dimensional object the x-ray attenuation coefficients are required for  $\mu(x, y, z)$ . This is accomplished by reconstructing the two-

dimensional distribution,  $\mu(x, y)$ , at fixed  $z$  locations within the object, called axial slices. In fact, for each axial slice, the values  $\mu(x, y)$  represent an average x-ray attenuation coefficient over the longitudinal direction. The region of averaging is determined by the slice thickness.

There are two methods to obtain a set of axial slices in CT: sequential CT or spiral CT. In sequential CT, the images are acquired successively slice by slice. A complete set of projection data is acquired in the  $x-y$  plane, known as the slice plane, at fixed  $z$  locations for each slice. During the data acquisition, the couch on which the object lies remains stationary. The couch is indexed to each slice location to acquire another set of projection data. By acquiring projection data in this manner, the projections at each  $z$  location are collected within the same plane through the object.

In spiral CT, the couch is continually translated while the projection data is acquired. The term spiral refers to the path that the source traces out along the  $z$ -axis. Pitch is a term used in spiral CT to describe the couch translation per source rotation normalized to the slice thickness. Pitch,  $P$ , is defined as,

$$P = \frac{d}{S} \quad (2.20)$$

where  $d$  is the distance the couch moves per  $360^\circ$  source rotation and  $S$  is the slice thickness. Spiral CT with a pitch of zero is equivalent to sequential CT.

The continuous data acquisition in spiral CT results in a linear relationship between the source angle  $\beta$  and the intersection point  $z_{pr}$  of the fan projection with the scanning axis  $z$ ,  $z_{pr}(\beta) = (d/360^\circ)\beta + z_0$ , where  $z_0$  denotes an offset. Here, each line integral in each projection is measured at a different  $z_{pr}$ . To estimate a set of projection data that would have been obtained in the  $x-y$  plane at a given  $z$  location, a linear interpolation (LI) scheme in the  $z$ -axis is required.

Planar data at a slice location,  $z_a$ , is estimated by linearly interpolating projection values from both sides of the slice plane (Figure 2-4) (Yen, Yan et al.

1999). A fan projection value  $R(\gamma, \beta, z_a)$  for detector fan angle  $\gamma$ , source angle  $\beta$ , at a slice location  $z_a$ , is calculated by,

$$R(\gamma, \beta, z_a) = (1-w)R(\gamma, \beta, z') + wR(\gamma, \beta + 360^\circ, z' + d) \quad (2.21)$$

where the weight  $w$  is given as  $(z_a - z')/d$  for  $360^\circ$  LI and  $0 \leq w \leq 1$ . The linear interpolation can be carried out by using either  $360^\circ$  LI or  $180^\circ$  LI (Crawford and King 1990; Kalender, Seissler et al. 1990). These interpolation schemes differ in the amount of data used to generate the axial slice.

In  $360^\circ$  LI, projection data for an axial slice at a  $z$  location,  $z_a$ , is estimated by interpolating from data points that are  $360^\circ$  apart. This method exploits the fact that in the absence of longitudinal motion, data that is  $360^\circ$  apart is identical. Spiral data with a  $\beta$  range of  $2 \cdot 360^\circ$  is used to approximate stationary data with a  $\beta$  range of  $360^\circ$ . As a result of the broad range of  $\beta$  data accessed, this interpolation method causes a broadening of the effective slice thickness compared to sequential CT (Polacin, Kalender et al. 1992).

The redundancy of the fan data can be utilized to reduce the range of data accessed by  $360^\circ$  LI. The method of  $180^\circ$  LI makes use of the fact that each line integral is measured twice in a  $360^\circ$  rotation of the source. A complementary set of data that is  $180^\circ$ , in the parallel angle  $\theta$ , from the measured data is generated by making use of this data redundancy. Projection data for the axial slice at  $z_a$  is estimated by interpolating from data points that are  $180^\circ$  apart in  $\theta$ . Spiral data with a  $\beta$  range of  $2 \cdot (180^\circ + 2\gamma_{\max})$  is used to approximate stationary data with a  $\beta$  range of  $180^\circ + 2\gamma_{\max}$ . The advantage of using less data is that the couch and patient motion will be decreased during the data acquisition. A narrower interpolating function, however, permits high frequency noise components in the interpolated data and results in an increase in image noise. The  $180^\circ$  LI method provides a good tradeoff between slice thickness broadening and image noise (Kalender, Seissler et al. 1990; Kalender and Polacin 1991; Polacin, Kalender et al. 1992; Wang and Vannier 1994).

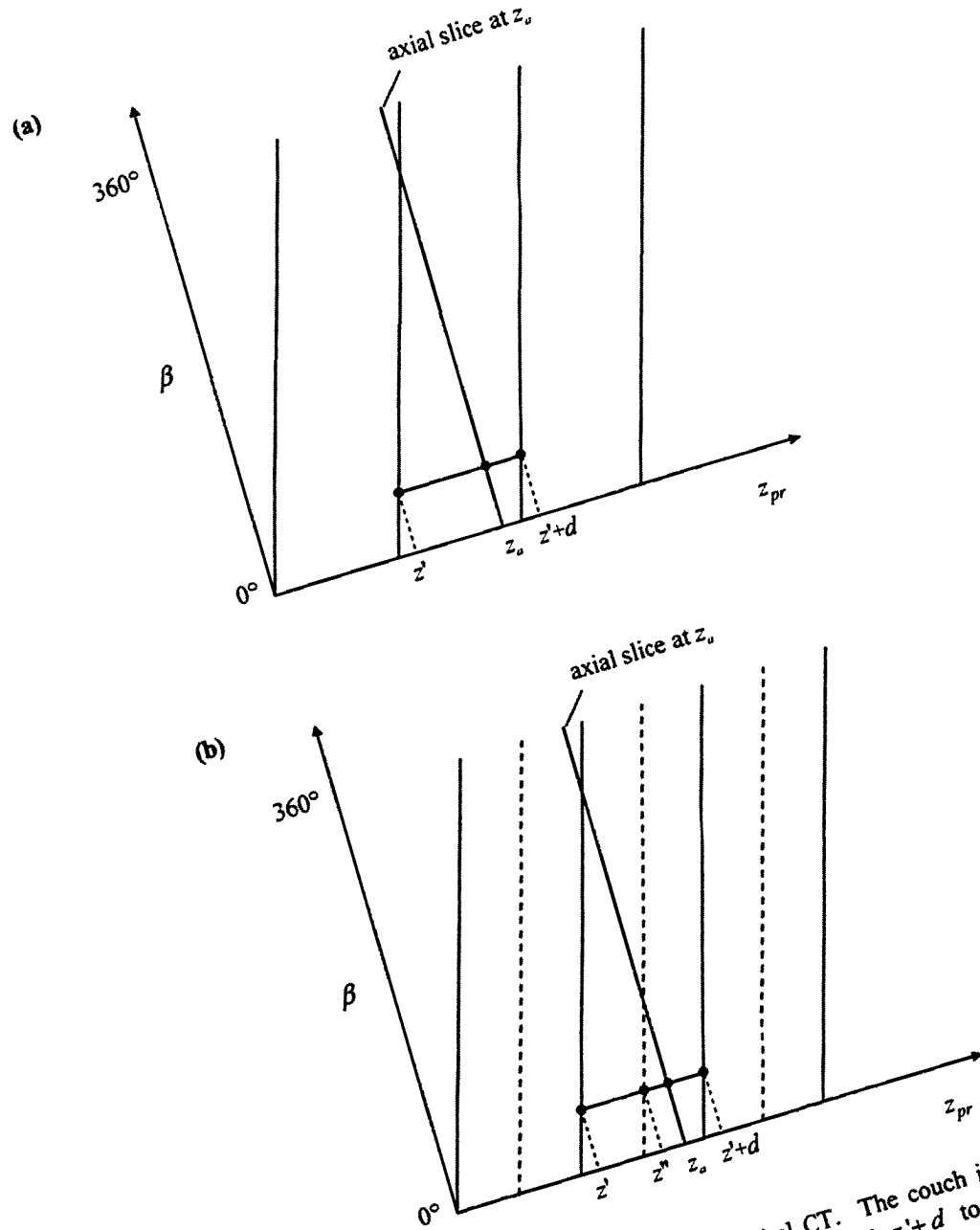


Figure 2-4 – Linear interpolation (LI) algorithms in spiral CT. The couch increment per  $360^\circ$  source rotation is denoted by  $d$ . (a)  $360^\circ$  LI uses points  $z'$  and  $z'+d$  to estimate a point in planar geometry at  $z_a$ . (b)  $180^\circ$  LI uses points  $z''$  and  $z'+d$  to estimate  $z_a$ . Dashed line data is  $180^\circ$  apart, in the parallel angle  $\theta$ , from the solid line data.

Note that the fan projection data obtained from spiral CT is still a two-dimensional array, made up of line integrals  $R_\beta(\gamma)$ , except that here the source angle  $\beta$  is a function of  $z$ . The columns in the sinogram array represent the detectors at each angle,  $\gamma$ , and the rows correspond to the  $z_{pr}$ -location that is a function of the source angle  $\beta$ .

### 2.1.2.2 Data Sufficiency Conditions

The object,  $\mu(x, y)$ , is completely represented by a set of parallel projections,  $\lambda_\theta(t)$ , if the projections are known for the subset,

$$\theta_0 \leq \theta < \theta_0 + \pi \quad (2.22)$$

and

$$-t_{\max} \leq t \leq t_{\max} \quad (2.23)$$

where  $t_{\max}$  is the value of  $t$  for which  $\lambda_\theta(t) = 0$  for  $|t| \geq t_{\max}$  for all  $\theta$  projections (Kak and Slaney 1987). To produce a complete set of equivalent parallel projections from a set of fan projections,  $R_\beta(\gamma)$ , the fan projections must be known for,

$$\beta_{\max} - \beta_{\min} \geq \pi + 2\gamma_{\max}, \quad (2.24)$$

where  $\beta_{\max}$  and  $\beta_{\min}$  are the maximum and minimum source angles, respectively, and  $\gamma_{\max} = \sin^{-1}(t_{\max}/D)$  (Parker 1982). The finite range  $-t_{\max} \leq t \leq t_{\max}$  will include all nonzero values of  $\lambda_\theta(t)$  so that sampling over this range gives non-truncated projections. The method of FBP requires that the projections be non-truncated and acquired over a complete angular range (Oppenheim 1977). This allows for an accurate reconstruction of the whole object using FBP.

### 2.1.3 Maximum-Likelihood Expectation-Maximization

The maximum-likelihood expectation-maximization (ML-EM) method of reconstruction is derived from emission CT (Shepp and Vardi 1982; Lange and Carson 1984) and applied to transmission CT by variable substitution (Nuyts, De



Man et al. 1998; Ruchala, Olivera et al. 1999). In emission CT a radioactive source that decays via photon emission is administered to the patient. The goal is to reconstruct the source distribution  $s_j$  at each point  $j$  in the patient by counting the total number of photon emissions  $y_i$  at projections  $i$  (with both detector location and projection angle being indexed by  $i$ ). Table 2-1 summarizes the notation used in the emission CT model and Figure 2-5 illustrates the image plane and a projection.

Table 2-1 – Summary of notation used in emission CT model.

$i$	Projection subscript
$j$	Image pixel subscript
$s_j$	Source distribution in pixel $j$
$x_{ij}$	Number of photons emitted by pixel $j$ that contribute to projection $i$
$y_i$	Total number of photons recorded in projection $i$
$p_{ij}$	Probability that photon emitted from pixel $j$ is detected in projection $i$

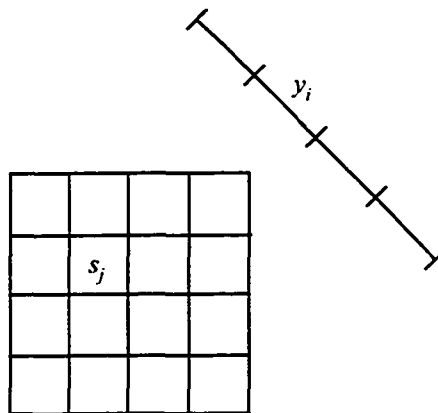


Figure 2-5 – For emission CT reconstruction, the image plane is divided into discrete source distribution pixels  $s_j$  and the total number of photons are recorded at projection  $y_i$ .

The measured counts  $y_i$  are based on a corresponding random variable  $Y_i$  that follows a Poisson probability distribution. The mean value of  $Y_i$  is modeled as,

$$\sum_j p_{ij} s_j \quad (2.25)$$

where  $p_{ij}$  is the probability that a photon emitted by pixel  $j$  is counted by projection  $i$ . The advantage of this statistical approach is that the Poisson nature of photon counting can be incorporated into the ML-EM framework. In addition, the physical properties of the detector geometry, the decay rate of the source, and the attenuation can be specified in terms of  $p_{ij}$ . The aim of emission CT is to estimate the source distribution parameters  $s_j$  from the observed counts  $y_i$ . In the method of ML, the parameters are estimated by maximizing the likelihood function (joint probability of the observations). The EM algorithm is the iterative computation of the ML estimates.

The basic idea of the EM algorithm is to embed the measured data into a larger set of data where the ML estimate is easier to obtain. In the case of emission CT the larger set of data is chosen as  $x_{ij}$  where,

$$y_i = \sum_j x_{ij} . \quad (2.26)$$

The term  $x_{ij}$  is the number photons emitted from pixel  $j$  and recorded at projection  $i$ . The total number of photons recorded for projection  $i$  is  $y_i$ . The samples  $x_{ij}$  are taken on corresponding random variables  $X_{ij}$  which also follow a Poisson distribution. The mean of  $X_{ij}$  is,

$$p_{ij} s_j . \quad (2.27)$$

The likelihood of the sample,  $L(x_{ij} | s_j)$ , given that  $X_{ij}$  depends on  $s_j$ , is defined to be the joint probability of  $x_{ij}$ . Since  $X_{ij}$  are independent the joint probability is the product of each probability function. The log likelihood function is given by,

$$\ln L(x_{ij} | s_j) = \sum_i \sum_j \left\{ -p_{ij}s_j + x_{ij} \ln(p_{ij}s_j) - \ln x_{ij}! \right\}. \quad (2.28)$$

The E-step of the EM algorithm requires the conditional expectation of  $X_{ij}$  given the measured data  $Y_i = y_i$  using the current estimate  $s_j^n$ . This conditional expectation is simply the binomial distribution with sample size  $y_i$  and probability parameter  $p_{ij}s_j / \sum_j p_{ij}s_j$  (McLachlan and Krishnan 1997) and is therefore,

$$E(X_{ij} | Y_i = y_i, s_j^n) = x_{ij}^n,$$

where

$$x_{ij}^n = y_i \frac{p_{ij}s_j^n}{\sum_j p_{ij}s_j^n}. \quad (2.29)$$

With  $x_{ij}$  replaced with  $x_{ij}^n$  in the log likelihood function of Eq. (2.28), the E-step results in,

$$E(\ln L | Y_i = y_i, s_j^n) = \sum_i \sum_j \left\{ -p_{ij}s_j + y_i \frac{p_{ij}s_j^n}{\sum_j p_{ij}s_j^n} \ln(p_{ij}s_j) \right\} + R \quad (2.30)$$

where  $R$  does not depend on  $s_j$ .

In the M-step the conditional expectation is maximized with respect to  $s_j$  holding  $s_j^n$  constant. Taking the partial derivative,

$$\frac{\partial}{\partial s_j} E(\ln L | Y_i = y_i, s_j^n) = -\sum_i p_{ij} + \sum_i y_i \frac{p_{ij}s_j^n}{\sum_j p_{ij}s_j^n} s_j^{-1}, \quad (2.31)$$

setting it equal to zero and solving for the new estimate  $s_j^{n+1}$  gives the final result,

$$s_j^{n+1} = \frac{s_j^n}{\sum_i p_{ij}} \sum_i p_{ij} \frac{y_i}{\sum_j p_{ij}s_j^n}, \quad (2.32)$$

where  $\sum_j p_{ij} s_j^n = y_i^n$ . This result is used to reconstruct the source distribution  $s_j^{n+1}$  at  $n+1$  iterations by observing photon emissions  $y_i$ , given an initial estimate  $s_j^0$ .

The advantages of the ML-EM reconstruction method are that it incorporates the Poisson nature of photon emission, produces only non-negative (realistic) values, and can utilize *a priori* information such as boundary information. However, a major disadvantage of the technique is its slow convergence rate. Also, for noisy data, the mean square error first decreases but then increases for large numbers of iterations.

The reconstruction formula of Eq. (2.32) can be directly applied to the case of transmission CT on the basis of the following variable substitutions,

$$\begin{aligned} \text{emission} &\rightarrow \text{transmission} \\ y_i &\rightarrow \lambda_i \\ s_j &\rightarrow \mu_j \\ p_{ij} &\rightarrow c_{ij} \end{aligned} \quad (2.33)$$

where  $\lambda_i$  is the line integral measured at projection  $i$  (again both detector and angle are being indexed by  $i$ ),  $\mu_j$  is the average attenuation coefficient at pixel  $j$ , and  $c_{ij}$  is the contribution of the pixel  $j$  to projection  $i$ . The new estimate  $\mu_j^{n+1}$  is arrived at iteratively from the old estimate  $\mu_j^n$  by,

$$\mu_j^{n+1} = \frac{\mu_j^n}{\sum_i c_{ij}} \sum_i c_{ij} \frac{\lambda_i}{\sum_j c_{ij} \mu_j^n}. \quad (2.34)$$

where  $\sum_j c_{ij} \mu_j^n = \lambda_i^n$  and represents the estimated projection. This direct substitution assumes that the observed samples  $\lambda_i$  are based on a Poisson variable. This assumption is not true since the line integrals are obtained from the log converted intensity values given as,

$$\lambda_i = \sum_j c_{ij} \mu_j = \ln \frac{I_i^0}{I_i}. \quad (2.35)$$

Although the statistical model is inaccurate, the ML-EM proves to be a robust algorithm in transmission CT (Nuyts, De Man et al. 1998).

The reconstruction algorithm in Eq. (2.34) can be interpreted as follows (Ruchala, Olivera et al. 1999): for each pixel  $j$ , the measured projection  $\lambda_i$  is compared to the estimated projection  $\lambda_i^n$  that is calculated from the current image estimate  $\sum_j c_{ij} \mu_j^n$ . The ratio of the measured to estimated projection is weighted by the contribution term  $c_{ij}$  and summed over all projections  $i$ . The sum is normalized to the total contributions by dividing by  $\sum_i c_{ij}$  and then applied as a multiplicative correction to the current pixel estimate  $\mu_j^n$  to obtain the new pixel estimate  $\mu_j^{n+1}$ .

### 2.1.3.1 Ordered Subsets

An ordered subset approach is used in the implementation of the ML-EM technique to improve the rate of convergence (Hudson and Larkin 1994). The ordered subset method processes subsets or groups of projection data by applying the ML-EM algorithm to each subset. This method, referred to as OS-ML-EM, has the same benefits as ML-EM but with accelerated convergence by a factor proportional to the number of subsets.

In the OS-ML-EM method, Eq. (2.34) is modified to handle each subset,  $S_k$ , at each sub-iteration  $k$ ,

$$\mu_j^{k+1} = \frac{\mu_j^k}{\sum_{i \in S_k} c_{ij}} \sum_{i \in S_k} c_{ij} \frac{\lambda_i}{\sum_j c_{ij} \mu_j^k}. \quad (2.36)$$

The algorithm above is applied to each of the subsets in turn using the current estimated pixel values in the processing of the next subset. Once all of the specified subsets have been processed a full-iteration has been completed. Additional full-iterations may be performed by repeating each of the sub-iterations beginning with the pixel values provided by the previous full-iteration.

The choice of grouping the projection data into subsets depends on subset balance and the level of noise in the projection data (Hudson and Larkin 1994). The pixel attenuation should contribute equally to any subset to provide a

balanced subset and this is generally achieved by using less subdivision (i.e. larger groups). Also, less subdivision should be used for noisier data. However, more subdivisions should be selected to realize the benefit of an accelerated convergence rate. Still, there is an effective limit to the degree of subdivision that is desirable to avoid magnification of the noise artifact commonly seen in ML-EM. The order of processing the projections within a subset is arbitrary, though it may be beneficial to the quality of the image to begin with the projection that corresponds to the largest variability in the image.

## 2.2 Limited Projection Data

Most applications of transmission CT use the method of FBP to reconstruct cross-sectional images of an object from a set of projection data because of its accuracy and speed. The mathematical formulation of FBP requires the knowledge of line integrals for all lines passing through the object in order to accurately reconstruct the object. This section discusses methods of reconstructing images from projection data that does not meet this requirement.

As stated in Section 2.1.2.2, all of the required line integrals will be measured if the parallel projection data is acquired for  $180^\circ$  of source rotation and if each parallel projection spans the full width of the object. These two data sufficiency conditions for parallel projection data are stated mathematically in Eqs. (2.22) and (2.23). It should be noted that both conditions require the sampling of the data to be uniform and sufficiently fine in the given range of  $\theta$  and  $t$ .

The parallel projection data is considered to be *limited* if the data fails to obey either one of the above criteria. If Eq. (2.22) is not met then the projection data is considered to be *limited-angle*, whereas failing to meet Eq. (2.23) results in data that is *limited-detector*. Figure 2-6 and Figure 2-7 illustrate these two types of limited data in comparison to complete data (Siltanen, Kolehmainen et al. 2003). A number of methods are described in the literature for dealing with either limited-angle or limited-detector projection data. These are discussed in the following sections.

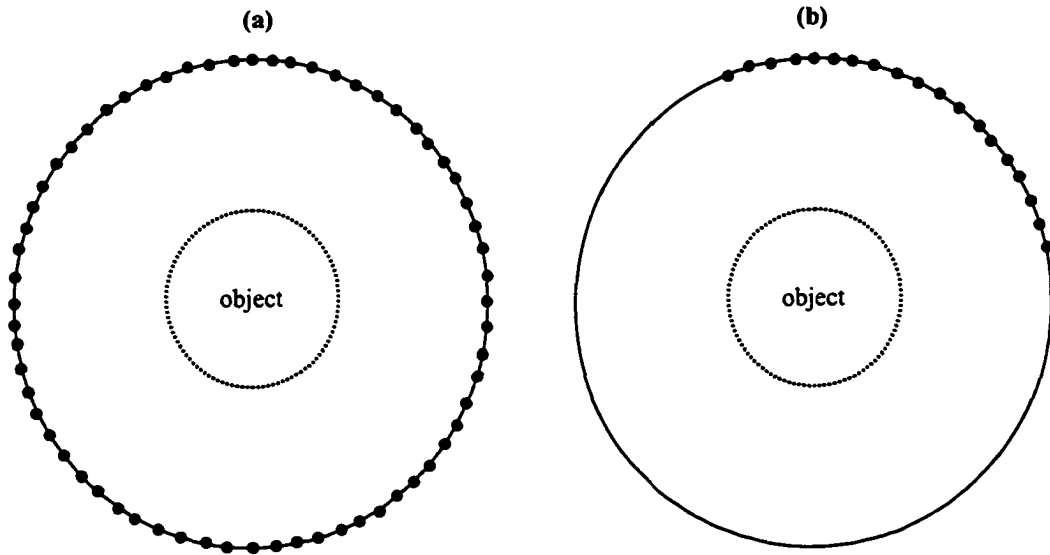


Figure 2-6 – Illustration of limited-angle. The black dots denote the location of the x-ray source for each projection. The detector is assumed to be across from the x-ray source as in Figure 2-7. (a) Full 360° data available. (b) Limited angular data available.

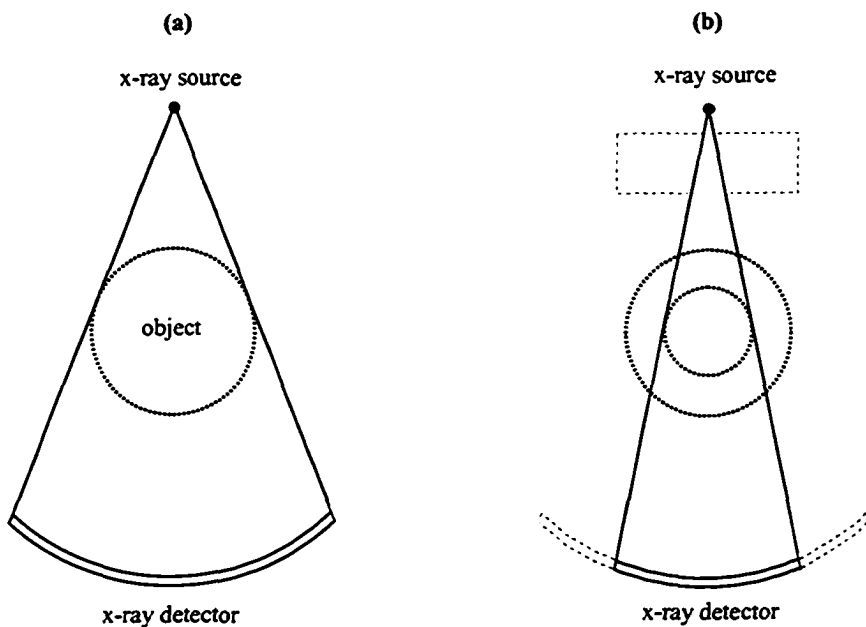


Figure 2-7 – Illustration of limited-detector. (a) Full extent of the object is visible in each projection. (b) Only a region inside the object is visible in each projection. Limited-detector may be a result of x-ray source collimation or reduced x-ray detector coverage.

## 2.2.1 Limited-angle

The geometry of the object and the imaging device may restrict the angular range of the acquired projection data. For example, in some industrial applications the objects may attenuate x-rays too highly at some angles to be useful or the physical dimensions of the object may restrict scanning at some projection angles (Tam, Eberhard et al. 1990). Also, reducing the number of projection angles may be used to decrease the scan time and patient dose. The following two methods aim to accurately reconstruct an object from a set of projection data that has a limited angular range but not a limited detector range.

### 2.2.1.1 Iterative Transform Methods

Iterative transform methods for limited-angle projection data estimate the missing data by repeatedly transforming between the image and the transform space and by applying a priori object information at each iteration (Sato, Norton et al. 1981; Tam and Perez-Mendez 1981a; Tam and Perez-Mendez 1981b; Tam, Eberhard et al. 1990). A consequence of the Fourier Slice Theorem, which states that the one-dimensional Fourier transform of a projection from a two-dimensional object is a line in the two-dimensional Fourier transform of the object, is that  $180^\circ$  of parallel projection data ( $180^\circ + 2\gamma_m$  of fan projection data) are required to uniquely reconstruct the image. If the angular range of the projection is less than this requirement then the two-dimensional Fourier transform of the object is known only in a limited angular range or wedge. The missing wedge data in Fourier space is effectively filled in by iteratively using a priori object information in the image space.

The method begins by taking the two-dimensional Fourier transform of an initial estimate of the image,  $\mu_0$ , which specifies the object boundaries, to obtain  $M_0$ . Next, the values in  $M_0$  are replaced with the Fourier transforms of the measured projections in the regions of Fourier space where data is available resulting in the augmented transform  $G_0$ . The image is obtained by performing a two-dimensional inverse Fourier transform on  $G_0$  where a priori object



information can be applied again. These steps are repeated until a suitable reconstruction is obtained.

The main limitation of this method is that the Fourier transform is computed in polar coordinates and must be re-sampled onto a rectangular grid prior to inversion. The process of re-sampling leads to significant reconstruction errors.

### **2.2.1.2 Shorter-Scan Filtered Backprojection**

A new framework of FBP is presented in the work of Noo, Defrise et al. (2002) and Chen (2003). This new method allows the angular condition to be relaxed if only a region-of-interest (ROI) within an object needs to be reconstructed. The detector condition, however, must still be met. That is, all of the line integrals in the fan containing the whole object must be measured. The sufficient condition for the accurate reconstruction of an ROI is stated in terms of the x-ray source path as: any line passing through the ROI must intersect the x-ray source path at least once. This condition is relaxed from the standard short-scan condition for fan projections (i.e.  $180^\circ + 2\gamma_m$ ) (Parker 1982), namely that all lines passing through the support of the object, not only the ROI, should intersect the x-ray source path at least once. These algorithms permit a shorter scan path to be chosen for an accurate reconstruction of an ROI.

### **2.2.2 Limited-detector**

As is the case with limited-angle data, here again the geometry of the object and the imaging device may limit the detector data. The category of limited-detector projection data may be further subdivided into two types: truncated or missing.

Imaging hardware may impose constraints on the lateral range of the collected projection data and the reconstruction of this type of data may not show the full extent of the object. For example, the multi-leaf collimator in tomotherapy imaging restricts the lateral range of the fan-beam (Ruchala, Olivera et al. 2002b). For objects that exceed the available fan-beam or detector range,

the measured projection data will not include all nonzero values of  $\lambda_{\theta}(t)$ . This type of limited-detector data is termed *truncated*.

Even if projection data is measured within the required range (i.e. meets the condition of  $\lambda_{\theta}(t) = 0$  for  $|t| \geq t_{\max}$ ) there may be missing projection data within this range as a result of gaps between detectors or from malfunctioning detectors. For example, the hexagonal arrangement of detectors in a type of PET scanner results in gaps between detector arrays and it is not possible to collect data along lines that fall between detectors (Karp, Muehllehner et al. 1988; Ollinger and Karp 1988). The missing data will appear as distinct gaps that run diagonally in the acquired sinogram. A dead detector in a 3<sup>rd</sup> or 4<sup>th</sup> generation CT scanner will result in a vertical or diagonal line in the sinogram, respectively. This type of limited-detector data is termed *missing*.

Errors that result from reconstructing a sinogram that has either type of limitation are related to the degree of truncation or missing data. The following limited-detector methods assume that the projection data meets the condition of complete angular range (i.e.  $180^{\circ}$  for parallel data or  $180^{\circ} + 2\gamma_m$  for fan data).

## **2.2.2.1 Truncated detector data**

### **2.2.2.1.1 Extrapolation**

Extrapolation procedures use a portion of the measured truncated projection to extend the projection, forming a complete detector projection which meets the condition of  $\lambda_{\theta}(t) = 0$  for  $|t| \geq t_{\max}$ . After this preprocessing step, the image is reconstructed using FBP. One such method (Lewitt 1979; Herman and Lewitt 1981) uses linear regression to fit measured data points that are just inside the boundary of the detector range. Ohnesorge and Flohr et al. (2000) developed a method that produces a mirror image of measured data in the interval between the projection edge and twice the value of the projection edge.

A recent method (Hsieh, Chao et al. 2004) uses the property that the total attenuation of each parallel projection remains constant for all angles when the

projections are non-truncated. Provided that truncation occurs only over a limited angular range, this property can be utilized to identify truncated projections and estimate the amount of truncation. Fitted water cylinders are used to estimate the projection data that extends beyond the measured truncated projection range.

In general, extrapolation procedures only work well for objects with fairly homogeneous density at the boundary and for small amounts of truncation.

#### **2.2.2.1.2 Local Tomography**

Conventional tomography (i.e. FBP) is a global procedure in that to reconstruct a single point in the object, all line integrals for all lines passing through a plane containing the point must be measured. Local tomography only requires the line integral for lines that pass very near the point and was initially developed by Faridani, Ritman et al. (1992; 1997). This method is similar to FBP but uses a slightly modified filter to directly reconstruct an image from a set of truncated projections. The image displays a localized region for which the projection data is acquired and is useful if the shape and location of a localized structure is of primary interest. However, the image pixel values are not related to the x-ray attenuation coefficients of the object.

Local tomography produces images with enhanced edges and boundaries compared to images reconstructed using conventional FBP but the images are not quantitatively useful. For procedures that require the anatomic outline of a localized structure rather than x-ray attenuation measurements this method is sufficient. This method has been investigated for truncated MV CT projections where the primary motivation is limiting the dose (Anastasio, Shi et al. 2003) and is currently a standard procedure for defining lung edges in the study of the coronary arterial tree (Faridani, Ritman et al. 1992).

#### **2.2.2.1.3 Sinogram Augmentation**

These methods use *a priori* information to complete the truncated projection data. A priori information can specify information about the boundary of the object and structures inside the boundary that are missing from the truncated data. Wagner et al. (1979) used glancing light rays to estimate the boundary of the object.

Artificial projection data was computed by ray tracing through the object outline (i.e. reprojection) assuming a uniform x-ray attenuation coefficient inside. The value of the coefficient was determined from the mean value in the measured data. The truncated data was augmented with the artificial data to produce a complete set that was reconstructed into an image using FBP.

A more sophisticated approach developed by Ruchala, Olivera, et al. (2002b) augments truncated tomotherapy projection data with planning CT data. The planning CT image is required to be reconstructed from a set of non-truncated projection data and can therefore be used to complete the truncated tomotherapy data. The tomotherapy image is aligned with the planning CT image using image fusion techniques and the latter image is reprojected to estimate the projection data. A complete set of projection data is formed by augmenting the tomotherapy truncated data with the reprojected planning CT data. This method relies on the success of aligning the images, which becomes difficult if the projection data is severely truncated.

#### **2.2.2.1.4 Offset Detector**

To circumvent the problem of truncated projection data the detector array can be laterally offset to collect half-fan projections (Cho, Johnson et al. 1995; Midgley, Millar et al. 1998). An electronic portal image device (EPID) area detector is used to produce cone beam tomographic reconstructions. The limited active area of the EPID prevents the measurement of full object projection data. By using a laterally offset detector combined with a full 360° source rotation, a complete set of data can be measured. The complete cone beam data is reconstructed using a Feldkamp type of algorithm which is an extension of fan-beam FBP (Feldkamp, Davis et al. 1984).

#### **2.2.2.1.5 Region-of-Interest Tomography**

In region-of-interest tomography (ROIT) (Nalcioglu, Sankar et al. 1979; Sankar, Nalcioglu et al. 1983), the complete projection data is available so the entire object or patient may be viewed, but it is desirable to view only a selected area within the object or patient. For example, a previous study may have determined

the disease to be well-localized and a follow-up scan of only the area of interest is required. ROIT reconstructs an ROI within a patient using a variable sampling scheme. The external region is sampled coarsely while the ROI is sampled finely. The coarsely sampled data is interpolated to generate data that has the same sampling interval as the finely sampled data and appended to the finely sampled data. This complete set of projection data can then be properly filtered using the conventional ramp filter. The ROI image is obtained by backprojecting the filtered ROI projection data. Although this technique reconstructs a small area within the patient or object, it requires the complete projection data to be available.

### **2.2.2.2 Missing detector data**

#### **2.2.2.2.1 Iterative Transform Methods**

Iterative transform methods iteratively estimate the missing projection data values by transforming the projection data between the projection space and a transform space (ex. Fourier, FBP). An inverse transform algorithm (ex. inverse Fourier, Radon) is used to obtain the complete projection data set which is reconstructed into an image using FBP. Two iterative transform methods that estimate missing projection data are discussed below.

##### **2.2.2.2.1.1 Constrained Fourier Reconstruction**

This method of dealing with missing projection data iteratively applies constraints to the 2-D Fourier transform of the measured projection data (Karp, Muehllehner et al. 1988; Ollinger and Karp 1988). Gaps in the projection data that appear as diagonal lines in the projection array will have Fourier coefficients that lie outside of a defined wedge, which is determined from the object radius. These coefficients outside of the defined wedge are set to zero by multiplying by a mask matrix, and an inverse Fourier transform of the remaining coefficients produces an estimate of a complete set of projection data. The measured projection data is inserted into the estimated data set and the process can be repeated. The image is obtained by applying FBP to the final data set.

Mathematically, this algorithm is described by Ollinger and Karp (1988) as,

$$\lambda_e^{(k+1)} = F^{-1} \left[ I_c \cdot F \left( \lambda^{(k)} \right) \right] \quad (2.37)$$

where  $\lambda^{(k)}$  denotes the current projection data at iteration  $k$ ,  $F$  and  $F^{-1}$  denote the Fourier and inverse Fourier transforms, respectively,  $I_c$  denotes the mask matrix with elements equal to zero in the constrained region and one elsewhere, and  $\lambda_e^{(k+1)}$  denotes the estimated projection data at iteration  $k+1$ . The current complete data set  $\lambda^{(k+1)}$  is formed by inserting the measured data  $\lambda$  into the estimated data by multiplying by  $I_e$ ,

$$\lambda^{(k+1)} = I_e \lambda_e^{(k+1)} + \lambda \quad (2.38)$$

where  $I_e$  is a matrix equal to one at all elements where projection data is estimated and zero where projection data is measured.

Since the missing projection data are estimated from all of the data, this method is most appropriate when the amount of missing data is small.

#### 2.2.2.2.1.2 Iterative Reconstruction Reprojection

Another iterative transform algorithm for estimating missing projection data is the iterative reconstruction reprojection algorithm (Medoff, Brody et al. 1983; Kim, Kwak et al. 1985; Ollinger and Karp 1988). This algorithm estimates the missing projection values by calculating them from the reconstructed image. It can be repeated as necessary by successively reconstructing images using FBP and reprojecting the image to determine the missing projections. Mathematically, the algorithm can be stated as,

$$\lambda_e^{(k+1)} = R \left[ \text{FBP} \left( \lambda^{(k)} \right) \right] \quad (2.39)$$

where  $R$  denotes the Radon transform of the image (i.e. reprojection) (Ollinger and Karp 1988). The next step is to insert the measured data into the estimated data to obtain the complete data set,

$$\lambda^{(k+1)} = I_e \lambda_e^{(k+1)} + \lambda \quad (2.40)$$

This technique is only successful if the first FBP step results in an acceptable reconstruction since the calculated projection values depend on the accuracy of the image. In the case of severely missing data, the FBP method will not produce an image that can be accurately inverted into projection data.

#### **2.2.2.2.2 Interpolation**

Instead of using an iterative transform algorithm to estimate the missing projection, the simple method of linear interpolation can be used. The holes in the projection data are estimated by linearly interpolating the value from the surrounding data. This requires knowing the exact location of the missing data and which surrounding data is acceptable to interpolate from. For small amounts of missing projection data this method is acceptable.

### **2.2.3 Iterative Optimization Algorithms**

Iterative optimization algorithms that reconstruct images from limited data (angular or detector) do not rely on the method of FBP and therefore do not require the data sufficiency conditions stated in Eqs. (2.22) and (2.23) to be met. There are numerous iterative algorithms which aim to converge upon the best estimate of the image pixel values using an optimized method of estimation. These methods include versions of ML-EM (Shepp and Vardi 1982; Lange and Carson 1984; Ollinger and Karp 1988) and image-space-reconstruction-algorithm (ISRA) (Daube-Witherspoon and Muehllehner 1986; De Pierro 1987; Titterington 1987; Ollinger and Karp 1988). The main advantage of these algorithms over FBP is that they are capable of operating in limited data conditions.

The method of ML-EM, discussed in Section 2.1.3, computes the maximum likelihood estimate of the image values based on the measured projection data. The computation involves a comparison between the measured projection data and the calculated projection data, the result is weighted and summed and then multiplied by the current image values to obtain the updated pixel values.

### **2.2.3.1 Image Space Reconstruction Algorithm**

The image space reconstruction algorithm (ISRA) is a modification of the ML-EM algorithm described above (Daube-Witherspoon and Muehllehner 1986). It is formulated by reversing the ordering of the comparison and the backprojection steps. Instead of comparing the measured projection data to the calculated projection data as in ML-EM, ISRA compares the backprojected image from the measured projection data to the backprojected image from the calculated data. The input to the algorithm is not the array of projection data but rather the reconstructed image(s) from the projection data. The reason for this modification is to increase the processing speed and decrease the memory requirements of the ML-EM algorithm in the case of spiral scanning where the projection data can be large.

Despite the above equation being similar to the ML algorithm this method does not compute the ML estimate of the image values. It can be derived from minimizing the squared-error criterion which is an inferior method of estimating parameters compared to the ML method (De Pierro 1987; Titterton 1987).

## **2.3 Reconstruction of truncated detector data**

The area covered by all projections (fan or parallel projections) at all angles is defined as the field-of-view (FOV) (Huang, Phelps et al. 1977). The FOV is a circle if the source-detector combination follows a circular trajectory and if the projections are acquired over a complete angular range (Noo, Defrise et al. 2002). On the condition that the object density is zero outside this FOV, then an accurate reconstruction of the object is feasible using FBP (Gore and Leeman 1980). However, if the object density outside the FOV is non-zero, then the acquired projections will be truncated.

Images reconstructed from a set of truncated projections using FBP will not show the full extent of the object and will contain an artifact, referred to as a “bowl” artifact (Huang, Phelps et al. 1977; Oppenheim 1977; Gore and Leeman 1980; Tofts and Gore 1980). The bowl-shaped artifact is a quantitative distortion



of pixel values that is flat near the center of the FOV and rises sharply at the edge. Structures that are outside the FOV are not reconstructed properly and produce the bowl artifact within the FOV.

One situation in which the projection data may be truncated is in tomotherapy imaging (TomoTherapy Hi-Art System, TomoTherapy Inc., Middleton, WI) (Figure 2-8). The FOV for this system is limited by the aperture size of the multileaf collimator (MLC) which allows a FOV of only 40 cm compared to a conventional (kV) CT FOV of 50 cm or larger. For objects that are larger than the FOV the acquired sinograms will be truncated resulting in the bowl artifact in the reconstructed images. The severity of the artifact depends on the amount of truncation. The artifact may impose limitations on various imaging tasks such as visual examination, patient positioning and verification (Ruchala, Olivera et al. 2002a), delivery verification (Kapatoes, Olivera et al. 1999), and dose reconstruction (Kapatoes, Olivera et al. 2001).

The method of FBP requires that all line integrals passing through the object be known. If the projections are truncated, i.e. some line integrals are not known, it is necessary to measure or estimate the missing projection values. By completing the projection measurements, in a manner that is consistent with the measured values, the bowl artifact may be eliminated or at least reduced.

Two novel techniques that reduce truncation artifacts as a result of a limited FOV have been developed. These are the sinogram merging (Hooper and Fallone 2002) and iterative sinogram augmentation (Hooper and Fallone 2003) techniques. The former combines two or more sets of truncated projection data to produce a non-truncated set of data, while the latter estimates the missing projection data. These techniques are unique in that they deal with raw sinogram data and have the ability to handle large amounts of truncation. This work is the experimental investigation of these techniques.

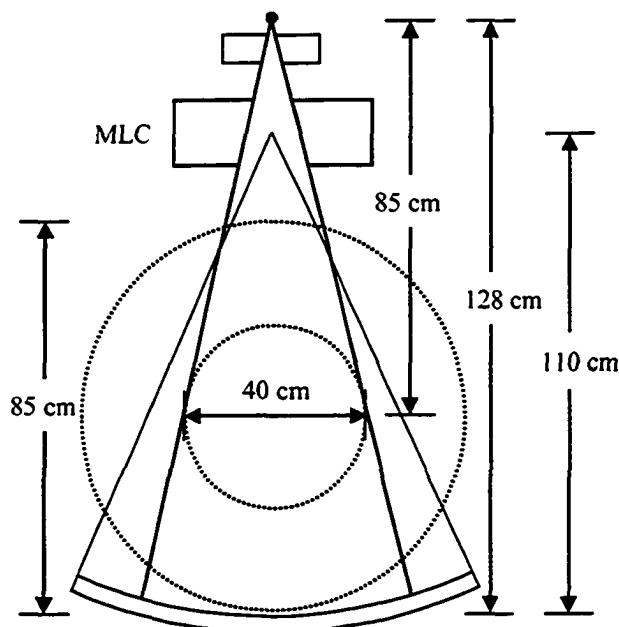


Figure 2-8 – The multileaf collimator (MLC) in tomotherapy limits the field-of-view (FOV) to 40 cm. The limited FOV of this system is defined by the x-ray source collimation not by the detector array. A special feature of this machine is that the detector array is focused on a point 18 cm below the x-ray source, rather than on the source as in most 3<sup>rd</sup> generation scanners.

### 2.3.1 Sinogram Merging

The sinogram merging technique uses two or more sets of truncated data to measure all of the sinogram data. The limited FOV in tomotherapy can often cover the full extent of the object with only two overlapping FOV circles. Hence, for the remainder of this work we will only consider the merging of two data sets.

An overview of the sinogram merging technique is illustrated in Figure 2-9. Two truncated fan-beam sinograms are acquired with the object shifted to the left and the right within the gantry. A non-truncated parallel-beam sinogram (multiple for spiral) is generated from the truncated fan-beam sinograms. An axial image is reconstructed by applying FBP to the parallel-beam sinogram. The resulting image has an increased FOV, referred to as the net FOV, which is discussed in more detail in Section 2.3.1.1. The net FOV is outlined in the axial image displayed in the figure.

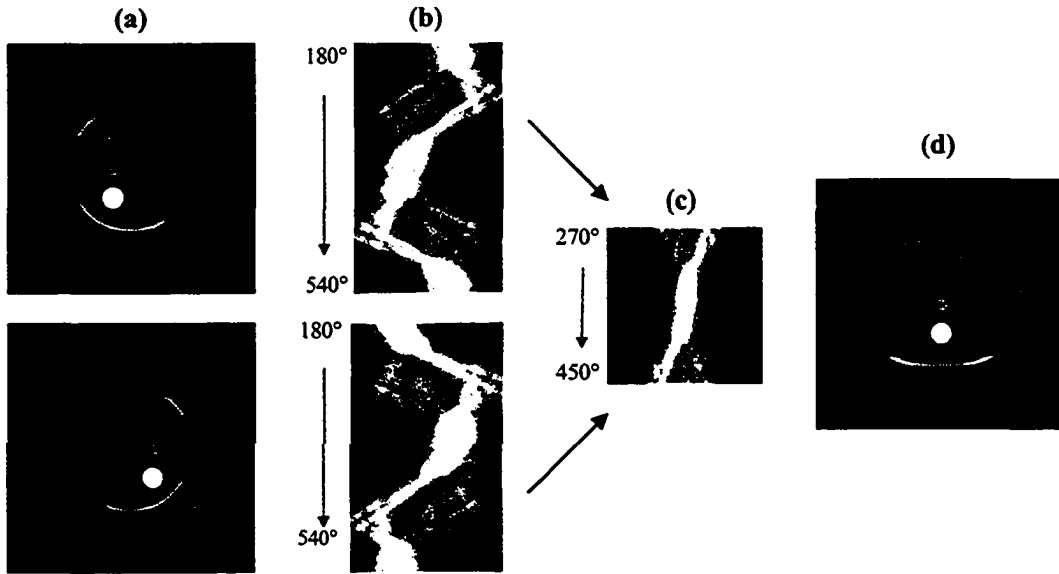


Figure 2-9 – Overview of sinogram merging technique. (a) Scan the phantom at left and right offset locations. White circle indicates scanning FOV. (b) Acquire the truncated fan-beam sinograms and merge into a single parallel-beam sinogram in (c). Apply filtered backprojection to the parallel-beam sinogram to reconstruct an axial image (d). Net FOV is shown in (d).

The fan-beam to parallel-beam geometry is illustrated in Figure 2-10 and uses the notation defined in Table 2-2 (Hooper and Fallon 2002). The fan-beam to parallel-beam merging algorithm is performed by calculating  $\beta$  and  $\gamma$  (source and detector fan angles for fan-beam sinograms) for each of the required values of  $\theta$  and  $t$  (projection angle and offset for parallel-beam sinograms). From the geometry shown in Figure 2-10 the following relations are obtained,

$$\theta = \beta + \gamma \quad (2.41)$$

$$\beta = \cos^{-1} \left( \frac{y_s - y_c}{D} \right) \text{ for } x_s \leq x_c \quad (2.42)$$

$$\beta = -\cos^{-1} \left( \frac{y_s - y_c}{D} \right) \text{ for } x_s > x_c \quad (2.43)$$

For  $\sin \theta = 0$ ,

$$x_s = t \cos \theta \quad (2.44)$$

$$y_s = y_c \pm \sqrt{D^2 - (x_s - x_c)^2} \quad (2.45)$$

For  $\sin \theta \neq 0$ ,

$$x_s = b \pm \sqrt{b^2 - c} \quad (2.46)$$

$$y_s = \frac{t - x_s \cos \theta}{\sin \theta} \quad (2.47)$$

where  $b$  and  $c$  are given as,

$$b = x_c \sin^2 \theta + t \cos \theta - y_c \sin \theta \cos \theta \quad (2.48)$$

$$c = (x_c^2 + y_c^2 - D^2) \sin^2 \theta + t^2 - 2ty_c \sin \theta \quad (2.49)$$

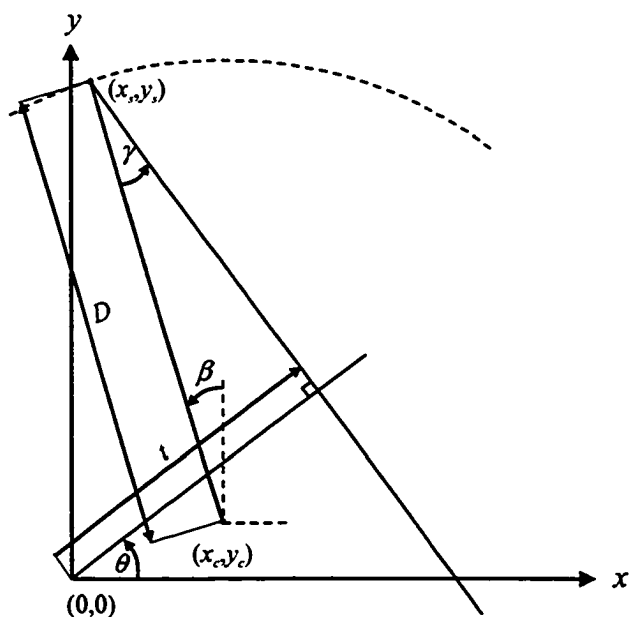


Figure 2-10 – Geometry of the fan-beam to parallel-beam merging procedure. The variables are defined in Table 2-2.

Table 2-2 – Notation used to describe the fan-beam to parallel-beam merging procedure.

$(x_s, y_s)$	X-ray source location
$(x_c, y_c)$	Axis of rotation for fan-beam
$(0, 0)$	Center for parallel-beam sinogram
$D$	Source-to-axis distance
$\beta, \gamma$	Source and detector fan angles for fan-beam sinograms
$\beta_{\min}, \beta_{\max}$	Minimum and maximum source angles for fan-beam sinograms
$\gamma_{\max}$	Maximum fan angle
$\theta, t$	Projection angle and offset for parallel-beam sinograms

In order to meet the data sufficiency conditions stated in Section 2.1.2.2, the object being imaged must be completely covered by the net FOV, which is discussed in Section 2.3.1.1. This will ensure that a complete set of parallel-beam projection data meeting Eqs. (2.22) and (2.23) can be generated from the two acquired fan-beam sinograms.

The algorithm for generating the parallel-beam sinogram from a set of fan-beam sinograms is:

1. Enter the specific input and output values for the parameters listed in Table 2-3.
2. Calculate the average  $\beta$  value in the first axial slice and then the first  $\theta$  angle for that slice.
3. Begin to fill the parallel-beam sinogram with the line integral  $\lambda_{\theta}(t)$  by starting with the first detector element,  $t$ , of the first row,  $\theta$ .
4. For each required  $\lambda_{\theta}(t)$  calculate the fan-beam angles  $(\gamma, \beta)$  using Eqs. (2.41)-(2.49).
5. Locate two  $\beta$  angles that are  $180^{\circ}$  apart, in  $\theta$ , and on opposite sides of the slice plane.
6. Interpolate the required parallel-beam pixel value,  $\lambda_{\theta}(t)$ , from the fan-beam sinograms,  $R_{\rho}(\gamma)$  using  $180^{\circ}$  LI and two-dimensional LI.
7. Assemble the parallel-beam sinogram on a pixel-by-pixel basis by repeating steps (4)-(7).
8. Repeat step (7) for each axial slice.
9. Reconstruct each parallel-beam sinogram using FBP.

Table 2-3 – List of input and output parameters required for fan-beam to parallel-beam merging algorithm.

Input Parameters for Fan-beam	
<u>Parameters required for each fan-beam <math>i</math></u>	
$(x_c^{(i)}, y_c^{(i)})$	Axis of rotation
$\beta_0^{(i)}$	Start source angle
$z_0^{(i)}$	Start $z$ -axis location
$N_m$	Number of x-ray source revolutions
<u>Global Parameters</u>	
$\Delta\beta$	Source angle increment
$d$	Couch increment per 360° source rotation
$D$	Source-to-axis distance
$N_f$	Number of detector elements in half of fan-beam
<u>Output Parameters for Parallel-beam and Axial Images</u>	
$r_p$	Physical detector spacing for parallel-beam
$N_p$	Number of detector elements in half of parallel-beam
$z_{u,m}$	Start axial slice location
$z_{e,m}$	End axial slice location
$\Delta z_u$	Axial slice increment

### 2.3.1.1 Net FOV

The sinogram merging technique is used to combine two truncated fan-beam sinograms to form a non-truncated parallel-beam sinogram corresponding to a larger net FOV. The net FOV produced by merging two sets of data is formed from the individual FOV circles and is illustrated in Figure 2-11. It is possible to reconstruct a particular point in the image,  $\mathbf{x}$ , provided any and all lines through  $\mathbf{x}$  intersect at least one of the FOV circles. If the individual FOV circles are overlapping, Figure 2-11(a), or just touching, Figure 2-11(b), then the point  $\mathbf{x}$ , either within or between the FOV circles, can be properly reconstructed. In the case where the individual FOV circles are separated as in Figure 2-11(c), it is not possible to accurately reconstruct the points lying between the individual FOVs since a complete 180° set of parallel projection data cannot be generated.

Note that the FOV is only increased in the offset direction and is not increased in the direction orthogonal to this. The width of the net FOV is the truncated FOV plus the sum of the offset distances.

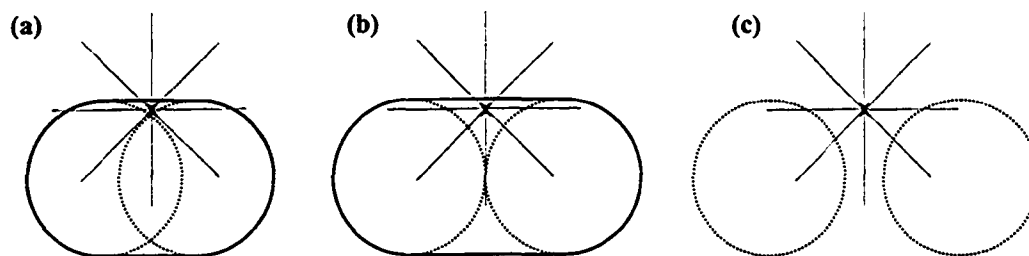


Figure 2-11 – Net FOV in sinogram merging technique. Dotted lines are FOVs for each individual scan and solid black line is net FOV in sinogram merging technique. Parallel-beam ray paths that intersect at a point,  $x$ , are shown as gray lines and  $180^\circ$  of parallel-beam data is required to reconstruct this point or any point. (a) Two overlapping FOV circles with net FOV outlined. (b) Two touching FOV circles with net FOV outlined. (c) Separate FOV circles, no net FOV.

### 2.3.1.2 Phase Angle

In step (5) of the fan-beam to parallel-beam merging algorithm, the required pixel values on opposite sides of the slice plane can be found in one or both of the fan-beam sinograms. In the region of overlap, there exist two data sets in which the required pixel value  $\lambda_g(t)$  can be obtained. If the two fan-beams begin at the same  $z$  location ( $z_0^{(1)} = z_0^{(2)}$ ) then the difference between the source start angles specifies a phase angle  $\phi = |\beta_0^{(1)} - \beta_0^{(2)}|$ . If the phase angle between the two sets of data is  $90^\circ$  then for any given  $\beta$  there will exist a data set from which the pixel value can be interpolated that will be closer to the given  $\beta$  than had the phase angle not been  $90^\circ$ .

This concept is illustrated in Figure 2-12, in which two sets of measured projection data for a 40 cm diameter object are displayed. The projection data at an angle  $\beta$  is plotted as a function of parallel-beam offset position  $t$  for a particular parallel-beam projection angle  $\theta$  (in this case  $\theta = 30^\circ$ ). In Figure 2-12(a) the projection data for both sets is identical since the fan-beam data is acquired at the same axis of rotation, where  $(x_c^{(1)} = 0 \text{ cm}, y_c^{(1)} = 0 \text{ cm})$  and

$(x_c^{(2)} = 0 \text{ cm}, y_c^{(2)} = 0 \text{ cm})$ . When the object is scanned at different offset locations the available data is pulled apart as seen in Figure 2-12(b). Here the object is scanned at  $(x_c^{(1)} = 5 \text{ cm}, y_c^{(1)} = 0 \text{ cm})$  and  $(x_c^{(2)} = -5 \text{ cm}, y_c^{(2)} = 0 \text{ cm})$  with a phase angle of  $0^\circ$  and the data now covers a larger offset position range or FOV. The FOV is increased from 40 cm to 50 cm in the direction in which the object is shifted. In this case the phantom is shifted in the  $x$ -axis so the FOV is increased in the  $x$ -axis only. The maximum increase in FOV would be apparent at  $\theta = 0^\circ$  where the projection data would have a  $t$  range of -25 to 25 cm.

If the shifted data in Figure 2-12(b) is acquired with a phase angle of  $90^\circ$  as in Figure 2-12(c), the available projection data is evenly distributed over the  $\beta$  range. For any required  $\beta$ , the data sets will provide a more accurate interpolation in the overlap region since one or both of the data sets will lie closer to the required  $\beta$ . The accuracy of the interpolation is only improved in the region of overlap where there exist two different data sets to interpolate from. This same result is achieved if the source start angles are equal but the start  $z$  locations are separated by  $1/4$  of the couch increment per  $360^\circ$  source rotation  $d$ .



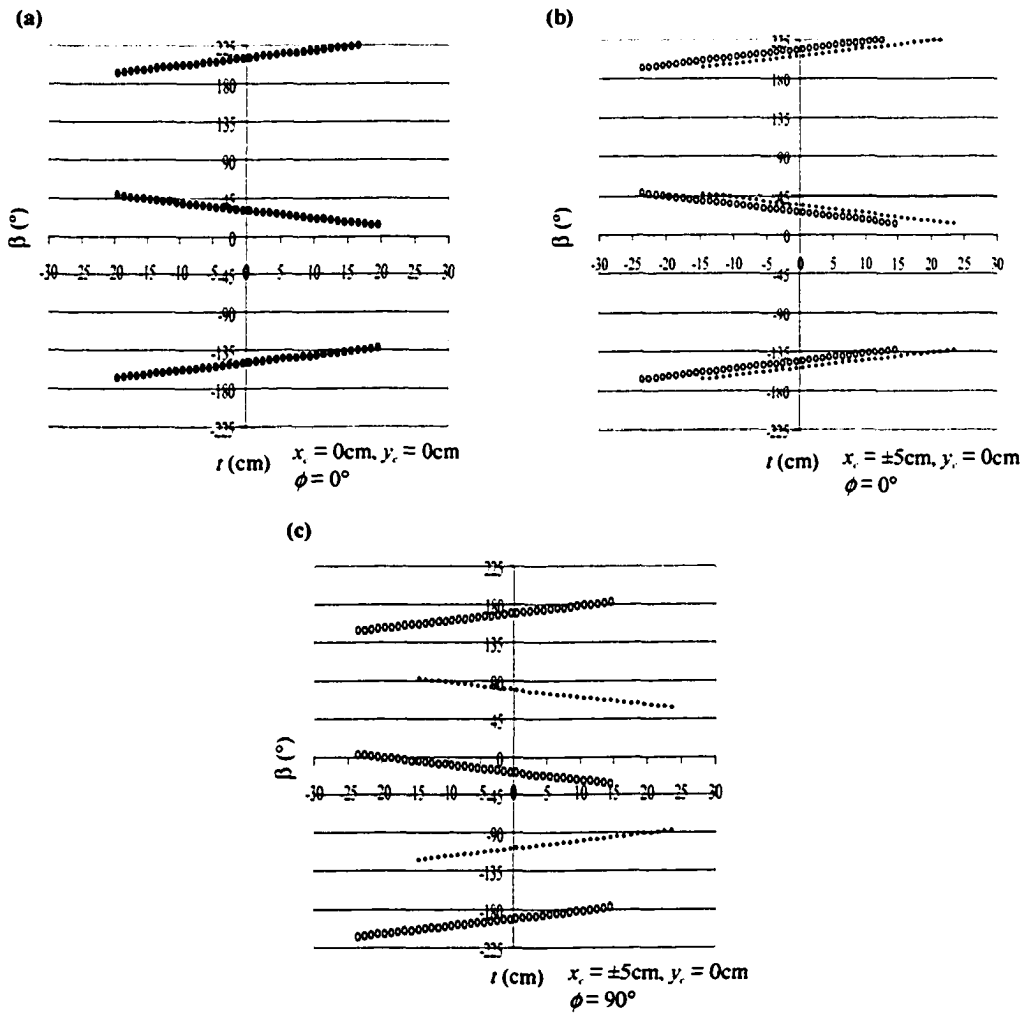


Figure 2-12 – Effect of object shift distances  $(x_c, y_c)$  and phase angle  $\phi$  on measured projection data. Data at fan-beam source angles  $\beta$  is plotted as a function of parallel-beam offset  $t$  for a parallel-beam projection angle  $\theta = 30^\circ$  for a 40 cm object. (a)  $(x_c = 0 \text{ cm}, y_c = 0 \text{ cm})$  and  $\phi = 0^\circ$ . (b)  $(x_c = \pm 5 \text{ cm}, y_c = 0 \text{ cm})$  and  $\phi = 0^\circ$ . (c)  $(x_c = \pm 5 \text{ cm}, y_c = 0 \text{ cm})$  and  $\phi = 90^\circ$ .

### 2.3.2 Iterative Sinogram Augmentation

The iterative sinogram augmentation technique is based on the OS-ML-EM algorithm. The missing projection data is estimated by utilizing the measured but truncated parallel-beam data and *a priori* information. The estimated data is appended to the truncated data set to produce a non-truncated parallel-beam sinogram, which is subsequently reconstructed using FBP. By appending the

estimated data to the truncated data, both the discontinuity at the edge of the FOV and the bowl artifact in the reconstructed images are reduced.

An overview of the iterative sinogram augmentation technique is illustrated in Figure 2-13. The technique uses the measured but truncated  $180^\circ$  parallel-beam sinogram (series of parallel-beam sinograms for spiral) and a start value model that specifies the external boundaries of the phantom. Using several iterative steps based on the OS-ML-EM algorithm, the missing sinogram data is estimated and appended to the edges of the truncated data to create an augmented sinogram. This augmented sinogram is reconstructed using standard FBP.

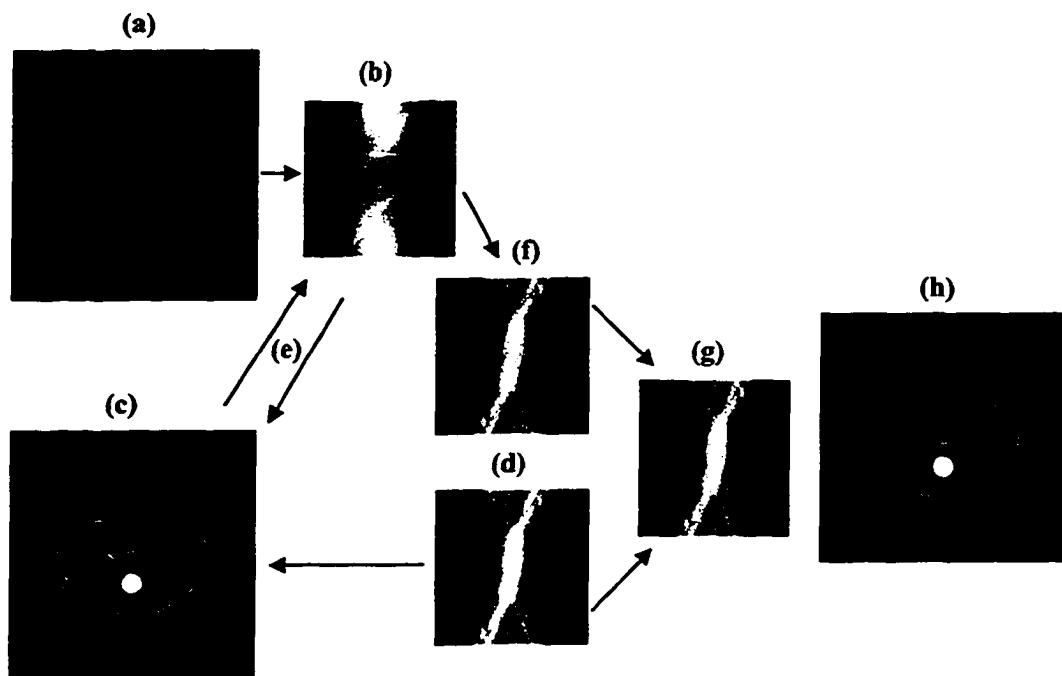


Figure 2-13 – Overview of iterative sinogram augmentation technique. Use the start value model (a) to estimate a parallel-beam sinogram (b). Calculate the image (c) from the estimated sinogram (b) and the measured truncated sinogram (d) using the OS-ML-EM algorithm. (e) Iteratively apply the algorithm, going back and forth between the estimated sinogram and the image. A non-truncated parallel-beam sinogram (f) is estimated when iterations are complete. Copy the portion of (f) that is missing in (d) to form the augmented sinogram (g). Apply filtered backprojection to (g) to reconstruct an axial image (h).

The iterative sinogram augmentation algorithm is described using the notation listed in Table 2-4:

1. Begin with  $k = 0$  and an initial estimate of the image (start model) that specifies  $\mu_j^0$  for all values of  $j$ .
2. Group projection data into subsets,  $S_k = S_0, S_1, \dots, S_m$ .
3. Calculate the line integrals  $\lambda_i^k$  using the equation,

$$\lambda_i^k = \sum_j c_{ij} \mu_j^k$$

for projections  $i \in S_k$  for all values of  $j$ .

4. Calculate the pixel values  $\mu_j^{k+1}$  using the equation,

$$\mu_j^{k+1} = \frac{\mu_j^k}{\sum_{i \in S_k} c_{ij}} \sum_{i \in S_k} c_{ij} \frac{\lambda_i^k}{\lambda_i^k}$$

for all values of  $j$ . The summations are for those values of  $i$  contained in the subset  $S_k$  and for which  $\lambda_i$  is defined (i.e.  $I_i$  has been measured).

5. Increment  $k$  by 1.
6. Repeat steps (3)-(5) for  $m$  number of sub-iterations.
7. Repeat steps (3)-(6) for  $M$  number of full-iterations.
8. Calculate the line integrals  $\lambda_i^{k=m \cdot M}$  for all values of  $i$  using the equation in step (3).
9. Replace the estimated data  $\lambda_i^{k=m \cdot M}$  with the measured data  $\lambda_i$  if  $\lambda_i$  exists.

That is,

$$\text{If } \lambda_i \text{ is defined, then } \lambda_i^{k=m \cdot M} = \lambda_i \text{ for all values of } i.$$

10. Repeat steps (1)-(9) for each parallel-beam sinogram.
11. Reconstruct each image from the corresponding augmented sinogram  $\lambda_i^{k=m \cdot M}$  using FBP.

Table 2-4 – List of notation used in the iterative sinogram augmentation technique.

---

$i$	Projection subscript (both detector and angle being indexed by $i$ )
$j$	Pixel subscript
$I_i^0$	Incident intensity of x-ray beam measured at projection $i$
$I_i$	Intensity of the x-ray beam after passing through an object measured at projection $i$ .
$\lambda_i$	$= \ln I_i^0 / I_i$ , for values of $i$ provided $I_i$ has been measured. This is the parallel-beam line integral obtained from the log converted intensity value at projection $i$ .
$\lambda_i^k$	Estimate of $\lambda_i$ at sub-iteration $k$
$\mu_j$	Average attenuation coefficient in pixel $j$
$\mu_j^k$	Estimate of $\mu_j$ at projection $i$
$c_{ij}$	Contribution of pixel $j$ to projection $i$
$k$	Sub-iteration index
$m$	Number of sub-iterations in a full-iteration
$M$	Number of full-iterations

---

## References

- Anastasio, M. A., D. Shi, X. Pan, C. Pelizzari and P. Munro (2003). "A preliminary investigation of local tomography for megavoltage CT imaging." Med Phys **30**(11): 2969-80.
- Chen, G. H. (2003). "A new framework of image reconstruction from fan beam projections." Med Phys **30**(6): 1151-61.
- Cho, P. S., R. H. Johnson and T. W. Griffin (1995). "Cone-beam CT for radiotherapy applications." Phys Med Biol **40**(11): 1863-83.
- Crawford, C. R. and K. F. King (1990). "Computed tomography scanning with simultaneous patient translation." Med Phys **17**(6): 967-82.
- Daube-Witherspoon, M. E. and G. Muehllehner (1986). "An Iterative Image Space Reconstruction Algorithm Suitable for Volume ECT." IEEE Trans Med Imag **MI-5**(2): 61-6.
- De Pierro, A. R. (1987). "On the Convergence of the Iterative Image Space Reconstruction Algorithm for Volume ECT." IEEE Trans Med Imag **MI-6**(2): 174-75.
- Faridani, A., D. Finch, E. Ritman and K. Smith (1997). "Local tomography II." J Appl Math **57**(4): 1095-127.

- Faridani, A., E. Ritman and K. Smith (1992). "Local tomography." J Appl Math 52(2): 459-84.
- Feldkamp, L. A., L. C. Davis and J. W. Kress (1984). "Practical cone-beam algorithm." J Opt Soc Am 1: 612-9.
- Gore, J. C. and S. Leeman (1980). "The reconstruction of objects from incomplete projections." Phys Med Biol 25(1): 129-36.
- Herman, G. T. and R. M. Lewitt (1981). "Evaluation of a preprocessing algorithm for truncated CT projections." J Comput Assist Tomogr 5(1): 127-35.
- Hooper, H. R. and B. G. Fallone (2002). "Technical note: Sinogram merging to compensate for truncation of projection data in tomotherapy imaging." Med Phys 29(11): 2548-51.
- Hooper, H. R. and B. G. Fallone (2003). An Iterative Procedure to Reduce Truncation Artifacts in Tomotherapy Imaging - A Simulation Study. Alberta Cancer Board Annual Research Meeting, Banff, Alberta.
- Hsieh, J., E. Chao, J. Thibault, B. Grekowicz, A. Horst, S. McOlash and T. J. Myers (2004). "A novel reconstruction algorithm to extend the CT scan field-of-view." Med Phys 31(9): 2385-91.
- Huang, S. C., M. E. Phelps and E. J. Hoffman (1977). Effect of out-of-field objects in transaxial reconstruction tomography. Reconstruction Tomography in Diagnostic Radiology and Nuclear Medicine. M. M. Ter-Pogossian, M. E. Phelps, G. L. Brownell, J. R. Cox, D. O. Davis and R. G. Evens. Baltimore, University Park Press.
- Hudson, H. M. and R. S. Larkin (1994). "Accelerated Image Reconstruction Using Ordered Subsets of Projection Data." IEEE Trans Med Imag 13(4): 601-9.
- Kak, A. C. (1979). "Computerized tomography with x-ray emission and ultrasound sources." Proc IEEE 67: 1245-72.
- Kak, A. C. and M. Slaney (1987). Principles of Computerized Tomographic Imaging. New York, IEEE Press.
- Kalender, W. A. and A. Polacin (1991). "Physical performance characteristics of spiral CT scanning." Med Phys 18(5): 910-5.
- Kalender, W. A., W. Seissler, E. Klotz and P. Vock (1990). "Spiral volumetric CT with single-breath-hold technique, continuous transport, and continuous scanner rotation." Radiology 176(1): 181-3.

Kapatoes, J. M., G. H. Olivera, P. J. Reckwerdt, E. E. Fitchard, E. A. Schloesser and T. R. Mackie (1999). "Delivery verification in sequential and helical tomotherapy." Phys Med Biol 44(7): 1815-41.

Kapatoes, J. M., G. H. Olivera, K. J. Ruchala, J. B. Smilowitz, P. J. Reckwerdt and T. R. Mackie (2001). "A feasible method for clinical delivery verification and dose reconstruction in tomotherapy." Med Phys 28(4): 528-42.

Karp, J. S., G. Muehllehner and R. M. Lewitt (1988). "Constrained Fourier Space Method for Compensation of Missing Data in Emission Computed Tomography." IEEE Trans Med Imag 7(1): 21-5.

Kim, J. H., K. Y. Kwak, S. B. Park and Z. H. Cho (1985). "Projection Space Iteration Reconstruction-Reprojection." IEEE Trans Med Imag MI-4(3): 139-43.

Lange, K. and R. Carson (1984). "EM reconstruction algorithms for emission and transmission tomography." J Comput Assist Tomogr 8(2): 306-16.

Lewitt, R. M. (1979). "Processing of incomplete measurement data in computed tomography." Med Phys 6(5): 412-7.

McLachlan, G. J. and T. Krishnan (1997). The EM Algorithm and Extensions. New York, John Wiley & Sons, Inc.

Medoff, B. P., W. R. Brody, M. Nassi and A. Macovski (1983). "Iterative Convolution Backprojection Algorithms for Image Reconstruction from Limited Data." J Opt Soc Am 73(11): 1493-500.

Midgley, S., R. M. Millar and J. Dudson (1998). "A feasibility study for megavoltage cone beam CT using a commercial EPID." Phys Med Biol 43(1): 155-69.

Nalcioglu, O., P. V. Sankar and J. Sklansky (1979). "Region-of-interest x-ray tomography (ROIT)." SPIE 206: 98-102.

Noo, F., M. Defrise, R. Clackdoyle and H. Kudo (2002). "Image reconstruction from fan-beam projections on less than a short scan." Phys Med Biol 47(14): 2525-46.

Nuyts, J., B. De Man, P. Dupont, M. Defrise, P. Suetens and L. Mortelmans (1998). "Iterative reconstruction for helical CT: a simulation study." Phys Med Biol 43(4): 729-37.

Ohnesorge, B., T. Flohr, K. Schwarz, J. P. Heiken and K. T. Bae (2000). "Efficient correction for CT image artifacts caused by objects extending outside the scan field of view." Med Phys 27(1): 39-46.

- Ollinger, J. M. and J. S. Karp (1988). "An Evaluation of Three Algorithms for Reconstructing Images from Data with Missing Projections." IEEE Trans Nucl Sci **35**(1): 629-34.
- Oppenheim, B. E. (1977). Reconstruction Tomography from Incomplete Projections. Reconstruction Tomography in Diagnostic Radiology and Nuclear Medicine. M. M. Ter-Pogossian, M. E. Phelps, G. L. Brownell, J. R. Cox, D. O. Davis and R. G. Evens. Baltimore, University Park Press.
- Pan, S. X. and A. C. Kak (1983). "A computational study of reconstruction algorithms for diffraction tomography: Interpolation vs. filtered-backpropagation." IEEE Trans Acoust Speech Signal Processing ASSP-31: 1262-75.
- Parker, D. L. (1982). "Optimal short scan convolution reconstruction for fanbeam CT." Med Phys **9**(2): 254-7.
- Polacin, A., W. A. Kalender and G. Marchal (1992). "Evaluation of section sensitivity profiles and image noise in spiral CT." Radiology **185**(1): 29-35.
- Radon, J. (1917). "Über die Bestimmung von Funktionen durch ihre Integralwerte längs gewisser Mannigfaltigkeiten." Berichte über die Verhandlungen der Sächsischen Akademien der Wissenschaften, Leipzig. Mathematisch-physische Klasse **69**: 262-7.
- Redpath, A. T. and T. M. Kehoe (1999). Simulator Computed Tomography. The Modern Technology of Radiation Oncology. J. Van Dyk. Madison, Medical Physics Publishing.
- Ruchala, K. J., G. H. Olivera and J. M. Kapatoes (2002a). "Limited-data image registration for radiotherapy positioning and verification." Int J Radiat Oncol Biol Phys **54**(2): 592-605.
- Ruchala, K. J., G. H. Olivera, J. M. Kapatoes, P. J. Reckwerdt and T. R. Mackie (2002b). "Methods for improving limited field-of-view radiotherapy reconstructions using imperfect a priori images." Med Phys **29**(11): 2590-605.
- Ruchala, K. J., G. H. Olivera, E. A. Schloesser and T. R. Mackie (1999). "Megavoltage CT on a tomotherapy system." Phys Med Biol **44**(10): 2597-621.
- Sankar, P. V., O. Nalcioglu and J. Sklansky (1983). "Undersampling Errors in Region-of-Interest Tomography." IEEE Trans Med Imag **MI-1**(3): 168-73.
- Sato, T., S. J. Norton, M. Linzer, O. Ikeda and M. Hirama (1981). "Tomographic image reconstruction from limited projections using iterative revisions in image and transform spaces." Appl Opt **20**(3): 395-99.

- Shepp, L. A. and Y. Vardi (1982). "Maximum Likelihood Reconstruction for Emission Tomography." IEEE Trans Med Imag **MI-1**(2): 113-123.
- Siltanen, S., V. Kolehmainen, S. Jarvenpaa, J. P. Kaipio, P. Koistinen, M. Lassas, J. Pirttila and E. Somersalo (2003). "Statistical inversion for medical x-ray tomography with few radiographs: I. General theory." Phys Med Biol **48**(10): 1437-63.
- Stark, H., J. W. Woods, I. Paul and R. Hingorani (1981). "An investigation of computerized tomography by direct Fourier inversion and optimum interpolation." IEEE Trans Biomed Eng **28**(7): 496-505.
- Swindell, W. and S. Webb (1988). X-ray Transmission Computed Tomography. The Physics of Medical Imaging. S. Webb. Bristol, Institute of Physics Publishing.
- Tam, K. C., J. W. Eberhard and K. W. Mitchell (1990). "Incomplete-Data CT Image Reconstructions in Industrial Applications." IEEE Trans Nucl Sci **37**(3): 1490-99.
- Tam, K. C. and V. Perez-Mendez (1981a). "Tomographical imaging with limited-angle input." J Opt Soc Am **71**(5): 582-92.
- Tam, K. C. and V. Perez-Mendez (1981b). "Limited-angle three-dimensional reconstructions using Fourier transform iterations and Radon transform iterations." Opt Eng **20**(4): 586-89.
- Titterton, D. M. (1987). "On the Iterative Image Space Reconstruction Algorithm for ECT." IEEE Trans Med Imag **MI-6**(1): 52-6.
- Tofts, P. S. and J. C. Gore (1980). "Some sources of artefact in computed tomography." Phys Med Biol **25**(1): 117-27.
- Wagner, W. (1979). "Reconstructions from restricted region scan data - new means to reduce the patient dose." IEEE Trans Nucl Sci **NS-26**(2): 2866-9.
- Walden, J. (2000). "Analysis of the direct Fourier method for computer tomography." IEEE Trans Med Imaging **19**(3): 211-22.
- Wang, G. and M. W. Vannier (1994). "Longitudinal resolution in volumetric x-ray computerized tomography--analytical comparison between conventional and helical computerized tomography." Med Phys **21**(3): 429-33.
- Yen, S. Y., C. H. Yan, G. D. Rubin and S. Napel (1999). "Longitudinal sampling and aliasing in spiral CT." IEEE Trans Med Imaging **18**(1): 43-58.



# 3 Materials and Methods

To re-bin the acquired fan projection data into equivalent parallel projection data, the Picker CT scanner fan-beam geometry must be determined. The raw sinogram data obtained from the scanner consists of projection data for each detector element in the fan-beam (columns) for a given fan-beam angle (rows). The fan-to-parallel re-binning algorithm, which is used for merging two truncated fan-beam sinograms into a single non-truncated fan-beam sinogram and also for re-binning a single fan-beam sinogram into a parallel-beam sinogram, calculates the  $(\gamma, \beta)$  coordinates for each fan-beam that corresponds to the parallel-beam  $(t, \theta)$  coordinates, and then interpolates between the measured  $(\gamma, \beta)$  sinogram values to estimate the  $(t, \theta)$  sinogram values.

In order to locate the actual projection value in the raw sinogram data, which is in the form  $(\text{detector}, \beta)$  rather than  $(\gamma, \beta)$ , the calculated  $\gamma$  value must be converted to a detector location. The process of converting the calculated  $\gamma$  value to a detector location is formulated in this chapter. The formulation requires the geometrical parameters of the Picker CT scanner. These parameters are the source-to-axis distance, the axis-to-detector-distance, the detector dimension, the total number of detectors in the ring and in the fan-beam, the number of projections per  $360^\circ$  source rotation, the angular increment, and the source start angle. The method of determining these parameters is discussed.

This chapter describes the phantoms and additional materials that were used for generating projection data. A description of the data pre-processing, acquisition, and post-processing steps used for reconstructing the various images in this experimental evaluation of the sinogram merging and iterative sinogram augmentation techniques is presented. Included in this description are methods for determining the offset locations for the merging technique and the optimal number of subsets to use in the iterative augmentation technique.

## 3.1 Experimental Setup

### 3.1.1 Geometrical Parameters

Since a tomotherapy unit was not available at the time of this work, the experiments were performed on a conventional (kV) CT scanner (Picker PQ5000, Phillips Medical Systems, Andover, MA). This is a fourth generation scanner consisting of a single array of stationary equispaced detectors on an outer circle, and an x-ray tube rotating on an inner circle. The geometry of the Picker scanner is shown in Figure 3-1. The detector array is focused on the axis. The angle  $\alpha$  may be found in terms of the detector fan angle  $\gamma$  by,

$$\alpha = \pi - \left[ \cos^{-1}(\sin(\gamma)) + \cos^{-1}\left(\frac{D \sin(\gamma)}{E}\right) \right], \quad (2.50)$$

where  $D$  is the source-to-axis distance and  $E$  is the axis-to-detector distance. The detector number  $n$  may then be found from,

$$n = \frac{E\alpha}{\tau} \quad (2.51)$$

where  $\tau$  is the fan-beam detector spacing, measured at the detector.

The diameter of the FOV circle at the axis is given by,

$$\text{FOV} = 2D \sin \left[ \pi/2 - \tan^{-1} \left( \frac{D/E + \cos(N_f \tau/E)}{\sin(N_f \tau/E)} \right) \right], \quad (2.52)$$

where  $N_f$  is the number of detectors in half of the fan-beam. The maximum detector fan angle is expressed as,

$$\gamma_{\max} = \sin^{-1} \left( \frac{\text{FOV}}{2D} \right). \quad (2.53)$$

The geometrical parameters for the Picker scanner are summarized in Table 3-1. For fan-beam geometry, the source-to-axis distance  $D$  is experimentally measured. The axis-to-detector distance  $E$  is calculated from the physical detector spacing  $\tau$  and the number of detectors in the ring. The fan-beam array dimension is determined from the raw sinogram data file, which is

described in Section 3.1.2. From the raw data file, the source start angle  $\beta_0$  and the source angle increment  $\Delta\beta$  are determined. The parallel-beam parameters are chosen so that the images reconstructed by our algorithms are consistent with the images reconstructed by the Picker scanner.

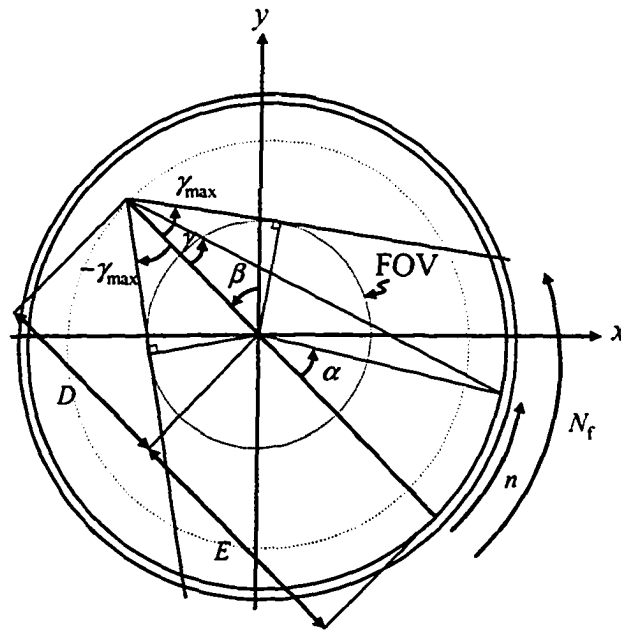


Figure 3-1 - Geometry of a fourth generation CT scanner. The diameter of a circle at the axis, subtended by the fan-beam, is the field-of-view (FOV).

Table 3-1 - Geometrical parameters for Picker PQ5000 CT scanner

	Parameter	Definition	Value
Fan-Beam	$D$	Source-to-axis distance	64.5 cm
	$E$	Axis-to-detector distance	81.8 cm
	$\tau$	Physical detector spacing (at detector)	0.107 cm
	$N$	Number of detectors in ring	4800
	$2N_f$	Number of detectors in fan-beam	1024*
	$\beta_0$	Source start angle	variable†
	$\Delta\beta$	Source angle increment	0.15° (360° per 2400 projections)
	$\gamma_{max}$	Maximum fan angle	21.8°
Parallel-Beam	$\tau_p$	Physical detector spacing	0.09375 cm*
	$2N_p$	Number of detectors in parallel-beam	512
	$\Delta\theta$	Projection angle increment	0.15° (180° per 1200 projections)

\*48 cm field-of-view

†user controlled for axial only

The source-to-axis  $D$  distance is determined by placing a known length of wire,  $l_1$  (6 cm), at the axis and measuring its magnification on film,  $l_2$ , a distance  $r$  from the axis (Figure 3-2). The wire is taped to a block and positioned at the axis using the alignment lasers in the CT scanner bore. The number of blocks is increased to vary the magnification distance  $r$  from the film which is placed under the blocks at distances of 5, 10, 15.1, and 20.3 cm from the central axis. A pilot scan at an appropriate kV to distinguish the wire on film is then performed for each distance  $r$ . The magnified length of the wire  $l_2$  is measured off of the film.

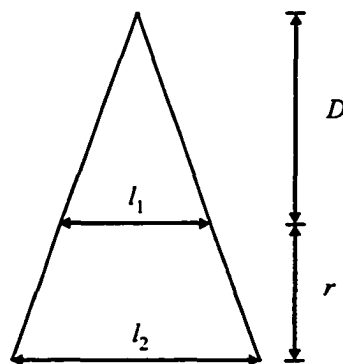


Figure 3-2 – Setup used to determine source-to-axis distance ( $D$ ). Variables are described in the text.

From similar triangles the magnification  $M$  may be expressed as,

$$M = \frac{l_2}{l_1} = \frac{1}{D}r + 1. \quad (2.54)$$

Plotting  $M$  as a function of  $r$  and using simple linear regression to fit the data, the source-to-axis distance  $D$  may be found from the inverse slope. The error in the magnification,  $\sigma_M$ , can be expressed as  $\sigma_{l_2}/l_1$ , where  $\sigma_{l_2}$  is the error in  $l_2$ .

Solid-state detectors are used to detect x-rays in the Picker scanner and each detector consists of a scintillator in contact with a photodiode. Optical photons are emitted by the scintillator when it is struck by x-rays. These optical photons reach the photodiode where the intensity of the photons is converted to an electrical signal proportional to the intensity. The physical detector width of the

photodiode,  $\tau$ , measured at the detector, is approximately 0.107 cm. From this value and the number of detectors in the detector ring,  $N$ , the axis-to-detector distance  $E$  is determined.

### 3.1.2 Picker Sinogram File Format

The file format of the raw sinogram data obtained from the Picker scanner is shown in Figure 3-3. The number format is 16-bit unsigned with big-endian byte ordering. The header is followed by a row of data for each projection measurement in a fan-beam. Each non-header row consists of predata containing the couch position and the detector starting address for the fan-beam, and the 1104 projection measurement data. The projection measurement data includes 40 reference detector values at the start and end. The number of non-header rows indicates the number of angles at which projection data is acquired. The format of the non-header portion of the sinogram file is  $\beta \times \gamma$  (rows x columns).

Header (4096)			
8 predata	40 ref	1024 data	40 ref
8 predata	40 ref	1024 data	40 ref
...	...	...	...
8 predata	40 ref	1024 data	40 ref

Figure 3-3 – File format of Picker sinogram file. The number of 16-bit integers is indicated.

An example of a fan-beam in the Picker scanner is illustrated in Figure 3-4. The width of the fan-beam is 1104 detectors and using Eq. (2.52) this corresponds to a 51 cm FOV. Each quadrant of the detector ring contains 1200 detectors. The locations of these detectors are indicated in the figure.

The detectors in the ring remain fixed while the source rotates inside the detector ring. In axial scanning mode, the user may specify the start-of-field (SOF) detector which indicates the detector that the central ray points to in the first fan-beam projection. The source start angle  $\beta_0$  is then found from,

$$\beta_0 \approx (\text{SOF}) \frac{90^\circ}{1200} + 90^\circ. \quad (2.55)$$

When it is not possible to specify the SOF, as is the case in spiral scanning mode, the source start angle  $\beta_0$  can be calculated from the detector starting address in the predata. The relation between the detector starting address and the SOF was determined in axial scanning mode.

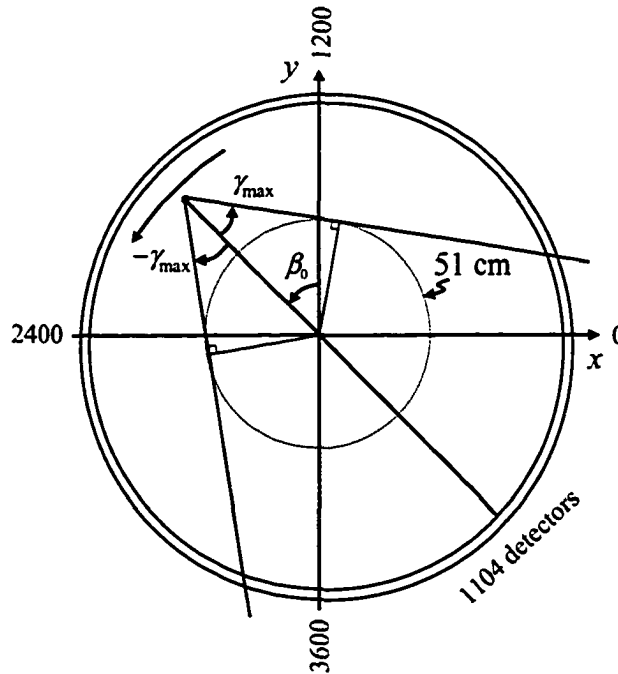


Figure 3-4 – A fan-beam in the Picker scanner. The diameter of the field-of-view (FOV) is 51 cm and is 1104 detectors wide. The direction of source rotation is counter clock-wise. The fixed locations of four of the 4800 detectors are shown. The source start angle  $\beta_0$  can be determined from these fixed detector locations.

The angular increment between each detector is  $0.075^\circ$  given that there are 4800 detectors in  $360^\circ$ . However, each data point in the fan-beam projection is an average of the data acquired from two adjacent detectors from two consecutive source angles. Since two fan-beam projection measurements are averaged together the effective angular increment is  $0.15^\circ$ . In a  $360^\circ$  x-ray source rotation there are 2400 projection measurements in the sinogram which corresponds to an angular increment of  $0.15^\circ$ .

The parallel-beam geometrical parameters listed in Table 3-1 are selected so that the images reconstructed from our algorithms can be compared to the images reconstructed from the Picker scanner. The Picker scanner reconstructs its images at a 48 cm FOV and we have chosen the parallel-beam parameters accordingly.

### 3.1.3 Phantom

Experimental data was generated using model 002H5 and 002LFC phantoms (CIRS, Norfolk, VA). These phantoms are illustrated in Figure 3-5. Both phantoms are elliptical in shape and represent a typical human torso. The former phantom is homogenous in structure and made of water equivalent material. The latter phantom is heterogeneous and manufactured from water, bone and lung equivalent materials with interchangeable rod inserts (2.5 cm diameter). Both phantoms are 30 cm wide x 20 cm thick x 15 cm long.

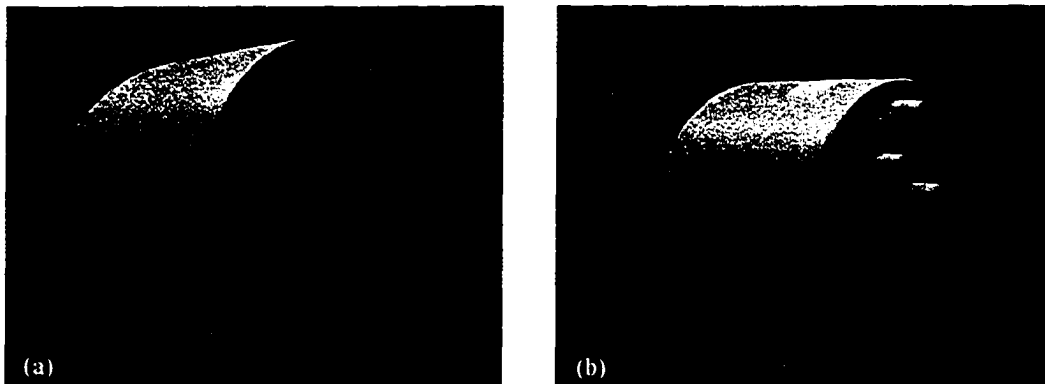


Figure 3-5 – CIRS phantoms used for collecting experimental data. Model (a) 002H5 (b) 002LFC.

Additional inserts were manufactured in-house from acrylic, nylon, and Delron rods. Some of the acrylic plugs varied in structure along the longitudinal axis, with 2 cm, 1 cm, and 0.5 cm air gaps as illustrated in Figure 3-6. These special plugs were positioned in the vertical, central holes of the 002LFC phantom, and were used for spiral scanning.

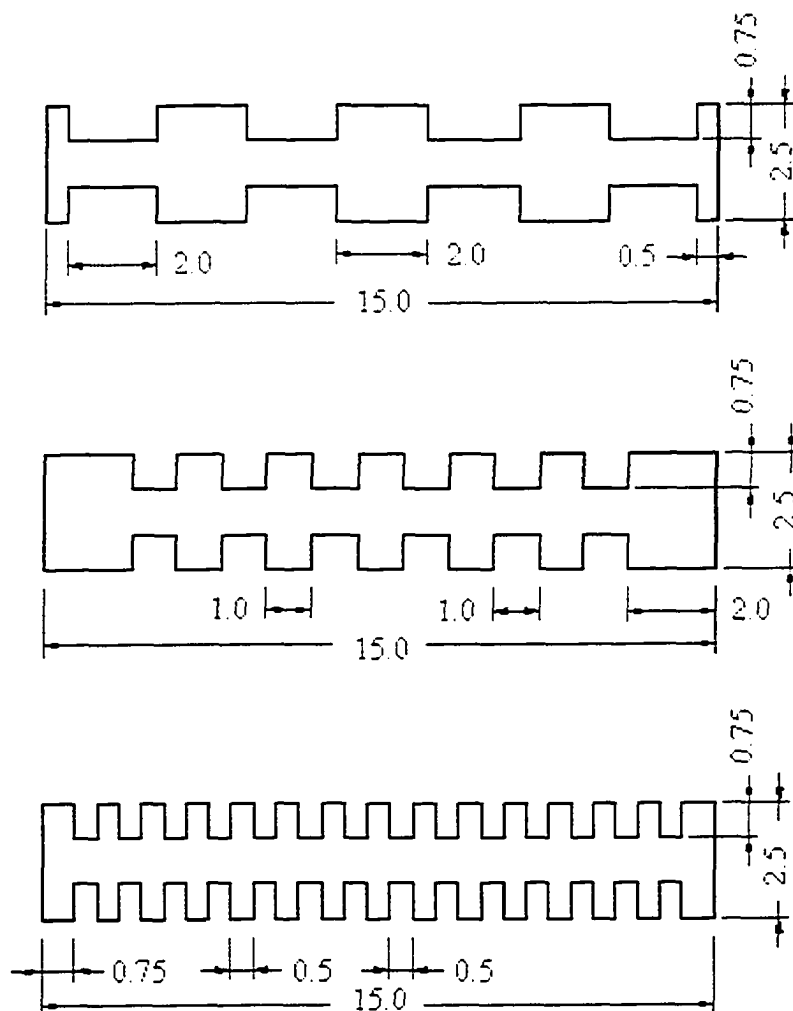


Figure 3-6 – Acrylic plugs with variable step widths (2.0 cm, 1.0 cm, and 0.5 cm). These were used in spiral scans. Units are in cm.

The phantom and plug materials are illustrated in Figure 3-7 and listed in Table 3-2. In this table, the physical contrast can be defined as,

$$\%contrast = 100 \left( \frac{\rho - \rho^w}{\rho^w} \right), \quad (2.56)$$

where  $\rho$  is the physical density of the material, and  $\rho^w$  is the physical density of the water equivalent material used in the CIRS phantoms.



Table 3-2 – List of material used in the CIRS phantom 002LFC and their position in the phantom according to the labels in Figure 3-7.

Material	Position in phantom	Physical density (g cm <sup>-3</sup> )	%contrast
-CIRS phantom			
Water equivalent		1.039	0.0
Lung equivalent		0.21	-79.8
Bone equivalent	f	1.60	54.0
Water equivalent rod	a	1.039	0.0
Air hole	b	1.205 x 10 <sup>-3</sup>	-99.9
Acrylic rod	c	1.203	15.8
Nylon rod	d	1.168	12.4
Delron rod	e	1.424	37.0

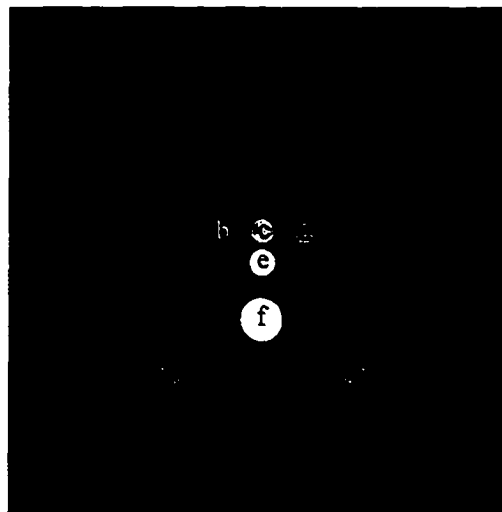


Figure 3-7 – CIRS phantom 002LFC indicating arrangement of contrast plugs used for axial scanning.

## 3.2 Data Preprocessing

The raw sinogram data that is collected from the Picker scanner represents the negative logarithm of the x-ray beam intensity measured along a fan. In order to obtain the  $\int \mu(x, y) dl$  sample from the transmission data, it is necessary to subtract the airscan data from the transmission data as,

$$(-\ln I) - (-\ln I_0) = \int \mu(x, y) dl, \quad (2.57)$$

which is derived from Eq. (2.18) by taking the logarithm of both sides. The airscan data,  $-\ln(I_0)$ , may be acquired with or without the couch in the path of the x-ray source. The significance of the couch in the sinogram merging technique will be discussed in Section 4.2.2.3.

Each fan-beam consists of 1104 detectors. The central 1024 detectors are used for collecting transmission data and the 40 reference detectors on either side are used for dynamic air calibration and rotor ripple correction (Van Dyk and Taylor 1999). The 1104 detectors correspond to a FOV of approximately 51 cm, and the central 1024 detectors have a FOV of about 48 cm. Provided that the patient does not exceed the 48 cm FOV the reference detectors on either side of the central 1024 detectors will properly measure airscan data throughout the scan procedure. Note that a full FOV is defined hereafter as 48 cm or 1024 detectors in the fan-beam.

In order to reconstruct an image from the raw sinogram data, the Picker scanner may perform an extensive list of pre-processing steps. These are listed for completeness and are; dark current subtraction; rotor ripple correction; bad detector replacement; air normalization; centering corrections; spectrum correction; and focal spot distance to detector correction (McDavid, Waggener et al. 1977; Crawford, Gullberg et al. 1988; Redpath and Kehoe 1999; Ruchala, Olivera et al. 1999). Dark current subtraction is performed by the Picker scanner prior to the start of the scan. In order to perform many of the other pre-processing steps, further proprietary information about the Picker scanner would be required. Since it was not the purpose of this project to reproduce the image quality of the Picker scanner, only the air normalization step was done in this work.

A 360° axial airscan was acquired each day an experiment was performed. By acquiring this airscan data and subtracting it from the transmission data using Eq. (2.57), detector variations were removed. We ignored the 80 reference detectors and only used the central 1024 detectors (48 cm FOV) for reconstructions.

After the airscan corrected fan-beam sinogram has been calculated, the data is re-binned into a parallel-beam sinogram and reconstructed using a FBP

algorithm. Our reconstructed values are converted to CT numbers or Hounsfield units (HU) by normalizing to the value of water equivalent material in the CIRS phantom using the equation,

$$CT(x, y) = 1000 \left( \frac{\mu(x, y) - \mu^w}{\mu^w} \right) (\text{HU}), \quad (2.58)$$

where  $\mu(x, y)$  is the mean x-ray attenuation coefficient in the pixel at location  $(x, y)$  and  $\mu^w$  is the x-ray attenuation coefficient of water for the quality of the x-ray beam used. CT numbers typically range from -1000 to +3000, -1000 corresponding to air, 0 to water, and dense bone +3000. Since our reconstruction program deals with unsigned integers, a value of 1000 is added to the HU values, so that 0 corresponds to air and 1000 to water. A calibration curve was generated to compare our images to the Picker images using the various materials in the phantom. The mean pixel value was calculated in a region-of-interest in each of the materials in both the Picker image and our reconstructed image. These mean values were used to construct the calibration curve. In both images the couch was present as a result of normalizing the transmission data to an airscan that does not include the couch. All further reconstructions utilized the calibration curve to generate correctly scaled pixel values in our images. This allows our images to be compared with the Picker images.

An additional apodizing or smoothing filter was used in the FBP algorithm in conjunction with the ramp filter. The frequency response of the Hann filter is shown in comparison to the ramp filter in Figure 3-8. By using the Hann filter with the ramp filter, high spatial frequency components can be attenuated. This results in decreased noise at high spatial frequencies at the cost of poorer spatial resolution (Redpath and Kehoe 1999).

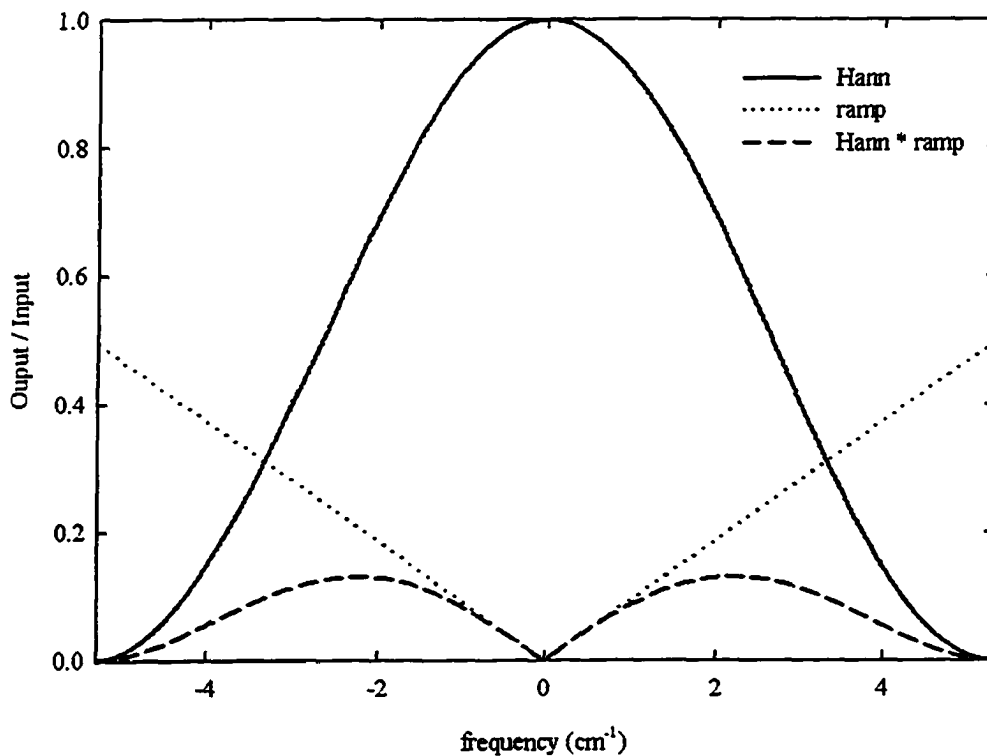


Figure 3-8 – Frequency response of filters.

### 3.3 Data Acquisition and Processing

Experimental verification of the artifact reduction techniques required the acquisition of fan-beam projection data for both sequential (axial) and spiral scanning modes. The scanning parameters used for both modes were: a nominal tube potential of 130 kV, a tube current of 200 mA, and a slice thickness of 0.3 cm. For spiral scanning, three pitches were investigated, 2, 1.5, and 1, and the scan length was 10 cm. The axial image dimensions were 512 x 512 pixels (48 cm x 48 cm). A series of axial images were used to generate sagittal and coronal images which have dimensions of 512 x 100 pixels (48 cm x 10 cm). The scan times for a 360° source rotation were 2 seconds for axial scanning mode and 1 second for spiral. An airscan, which was used for normalization of the transmission data, was acquired each time an experiment was performed with the scan times chosen according to the scan mode.

Since the acquired sinograms from the Picker scanner are physically non-truncated (48 cm FOV), the required truncated projections were simulated by deletion of the appropriate projection values. Using Eq. (2.52), the required FOV may be found for a given number of detectors,  $N_f$ , in half of the FOV. The fan-beam sinograms were artificially truncated to 24 cm, 22 cm, and 20 cm FOVs measured at the axis. These FOVs correspond to the central 510, 468, and 426 detectors in the fan-beam sinogram, respectively.

The following terminology is used to clarify each type of image that is studied. Images reconstructed from a full FOV fan-beam sinogram, where the phantom was positioned at the axis, are referred to as *reference images*. Images reconstructed from a full FOV fan-beam sinogram with the phantom positioned at left or right offset positions, are referred to as *offset images*. Images reconstructed from a truncated fan-beam sinogram are referred to as *truncated images*. Images reconstructed from merging two truncated fan-beam sinograms using the sinogram merging technique are referred to as *merged images*. Finally, images reconstructed from augmented sinograms using the iterative sinogram augmentation technique are indicated as *augmented images*.

### **3.3.1 Reference and Truncated Images**

The fan-beam sinograms used to produce the reference and truncated images were acquired with the phantom positioned at the axis using the bore lasers and the alignment markings on the phantom for positioning. Axial and spiral fan-beam sinograms, full and truncated, were re-binned into parallel-beam sinograms and subsequently reconstructed into axial images using FBP. Sagittal and coronal images, reference and truncated, were generated from the set of the axial images produced from spiral fan-beam sinograms.

### **3.3.2 Sinogram Merging**

The sinogram merging technique requires the acquisition of two sets of fan-beam data with the phantom positioned at lateral offset locations. The CIRS 002LFC phantom was scanned at +4 cm and -4cm offset locations (nominal value) and

both axial and spiral fan-beam data were acquired. Since the couch does not move laterally, the phantom was manually shifted to the left and right offset locations on the couch. The sagittal lasers were used for alignment of the laterally shifted phantom. These ceiling mounted lasers permit the user to enter in the desired offset location and they then move to that location.

The CIRS phantom 002H5 was also scanned at lateral offset locations of +4 cm and -4cm and axial fan-beam data was acquired. This homogenous phantom was chosen to better illustrate the effect of the couch in the sinogram merging technique as described in Section 4.2.2.3.

The left and right fan-beam sinograms were each re-binned into parallel-beam sinograms and reconstructed into offset images using FBP. These images were used to determine the offset location using the cross correlation function. For spiral data, a central longitudinal portion of the data was used to reconstruct the offset images to determine the offset.

The left and right fan-beam sinograms were truncated to 24, 22, and 20 cm FOVs. For each truncated FOV, the left and right fan-beam sinograms were merged into a single parallel-beam sinogram (a series of parallel-beam sinograms in spiral acquisition) using the sinogram merging technique. The resulting parallel-beam sinogram(s) were each reconstructed into merged images using FBP.

For spiral data, it is necessary to accurately know the  $z$ -axis position for each scan as these parameters are required for the sinogram merging technique. Also, it is desired to compare merged images to the reference images, and it was therefore necessary to know the  $z$ -axis location of the left and right scans relative to the reference scans. The  $z$ -axis location was determined by the placement of a fiducial marker on the phantom and reconstructing slices at an index of 0.05 cm. The slice number at which the marker is no longer visible was noted between the left and right images relative to the reference image. To reduce any  $z$ -axis positioning error between each pitch at each phantom location, data for all three pitches was acquired after positioning the phantom. The  $z$ -axis position was then the same for each pitch at a given phantom location.

An axial airscan with the couch in the path of the x-ray beam was also performed. The couch remained at the same height as when the phantom was scanned. For spiral scanning, a spiral airscan with the couch in place was generated from the axial airscan. The algorithm for generating a spiral airscan from an axial airscan is:

1. Note the number of non-header rows in the spiral fan-beam sinogram for which a spiral airscan is required.
2. Read in the first non-header row from the spiral fan-beam sinogram and note the detector starting address in this row.
3. Find the row in the axial airscan that corresponds to this detector starting address.
4. Write out the axial airscan starting with this row.
5. Continue to write out the axial airscan data row-by-row until the end of the axial airscan is reached.
6. Return to the first non-header row of the axial airscan and write out the data until the number of rows is complete.

By lining up the detectors between the spiral transmission and spiral airscan data in this manner, variations in the detectors are properly removed by the air normalization. This assumes that the couch is uniform in the longitudinal direction when included in the airscan. Ideally, both the couch position ( $z$  location) and the detectors (source angle) could be lined up between the transmission and airscan sinograms, but this was not possible because the source start angle cannot be specified in spiral scanning mode.

### **3.3.2.1 Lateral Offset Distances**

Two methods were used to determine the lateral offset distances for the shifted phantom in the sinogram merging technique. One was the use of the alignment lasers during the experiment and the second involved cross correlating the offset images after the experiment.

The first method used the sagittal lasers to align the phantom at the left and right offset locations during the experiment. The acquired fan-beam sinograms

were merged using the nominal laser offset value as the offset distance  $(x_c^{(i)}, y_c^{(i)})$  in the sinogram merging technique.

In the second method, the sagittal lasers were used in the same manner but, in addition, the offset images (i.e. left and right non-truncated images) were used to determine the offset distance by performing a cross correlation. The cross correlation of the offset images was performed using MatLab (MathWorks, Natick, MA). The potential use of the cross correlation function to determine the offset distance was investigated using several types of input data. Left and right images that were non-truncated, truncated, and truncated with masked edge artifacts were investigated. Single rows in the left and right parallel-beam sinograms were also investigated, and included non-truncated and truncated sinograms.

The assumption of cross correlation is that the images or sinogram data are essentially identical except for a physical shift. This criterion can only be met if the images or data are non-truncated. As the images or data become truncated, the cross correlation method is unable to accurately measure a shift. Since the data collected from the CT scanner used in this work is physically non-truncated, we were able to use the non-truncated left and right images to determine the offset using the cross correlation method.

### **3.3.3 Iterative Sinogram Augmentation**

The iterative sinogram augmentation technique requires a parallel-beam sinogram as input for the algorithm. The CIRS 002LFC phantom was positioned at the axis using the bore lasers for alignment. The acquired fan-beam sinograms (axial and spiral) were truncated to 24, 22, and 20 cm FOVs and were re-binned into a parallel-beam sinogram (series of parallel-beam sinograms for spiral). Each parallel-beam sinogram was processed using the iterative algorithm to produce an augmented sinogram, which was subsequently reconstructed into an augmented image using FBP.

The parallel-beam sinograms each contain  $180^\circ$  of projection data in  $0.15^\circ$  increments (1200 rows of projection data). The iterative algorithm was performed



using 2 full-iterations ( $M$ ), each with 240 sub-iterations ( $m$ ). Each sub-iteration used 5 sinogram rows in  $36^\circ$  increments. A mathematical phantom was used to specify the start value model,  $\mu_j^0$ . As illustrated in Figure 3-9, the external boundaries of this model are approximately the same as those of the CIRS phantom, and the model has a uniform water equivalent density (value of 1000) inside the boundary and zero density outside.

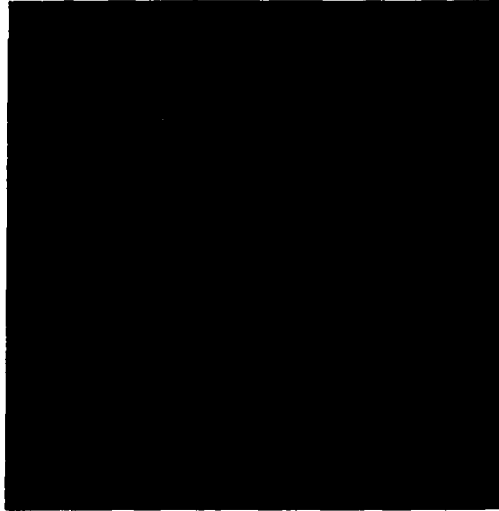


Figure 3-9 – Start value model used in iterative sinogram augmentation technique. The outer boundary is approximately the same as the CIRS phantom. The values inside the boundary are 1000 (HU plus 1000) and zero outside.

### 3.3.3.1 Number of subsets

The choice of the number of sub-iterations to use in the iterative augmentation technique was determined by measuring how well the estimated sinogram,  $\lambda_i^k$ , fit with the measured sinogram,  $\lambda_i$ . A sinogram goodness-of-fit (GOF) parameter was calculated,

$$GOF_{\text{sinogram}} = \frac{1}{N} \sum_i \frac{|\lambda_i^k - \lambda_i|}{\lambda_i}, \quad (2.59)$$

where the summation is over all values of  $i$  for which  $\lambda_i$  is defined (i.e. where  $I_i$  is measured), and  $N$  is the number of terms included in the summation. The variants of the OS-ML-EM algorithm investigated will be denoted by the number

of sub-iterations followed by the number of sinogram rows used in each subset. We investigated 600(2), 240(5), 120(10), 30(40), 10(120), 4(300), and 1(1200). The last variant is the standard ML-EM algorithm, which is a particular case of OS-ML-EM when a single subset includes all projection data. The GOF was calculated after each full-iteration for up to 10 full-iterations.

### 3.4 Analysis

The impact and magnitude of reducing truncation artifacts was evaluated both qualitatively and quantitatively. Qualitative analysis consisted of viewing the merged and augmented images at different window settings to look for artifacts. Profiles were also created through the images and compared to profiles created through reference images. The images were viewed and the profiles created using ImageJ software (National Institutes of Health, Bethesda, MD).

Quantitative analysis of the merged and augmented images was also performed. The results were evaluated using the image GOF and Bias parameters calculated as,

$$\begin{aligned} \text{GOF}_{\text{image}} &= \frac{1}{N} \sum_{DR} \frac{|\mu_j - \mu_j^{\text{ref}}|}{\mu_j^{\text{ref}}}, \\ \text{Bias} &= \frac{1}{N} \sum_{DR} \frac{\mu_j - \mu_j^{\text{ref}}}{\mu_j^{\text{ref}}} \end{aligned} \quad (2.60)$$

where here  $\mu_j$  are the pixel values in the image being analyzed,  $\mu_j^{\text{ref}}$  are the pixel values in a reference image, the summation is only over those pixels within a defined region ( $DR$ ), and  $N$  is the number of pixels in the defined region.

## References

- Crawford, C. R., G. T. Gullberg and B. M. Tsui (1988). "Reconstruction for fan beam with an angular-dependent displaced center-of-rotation." Med Phys 15(1): 67-71.
- McDavid, W. D., R. G. Waggener, W. H. Payne and M. J. Dennis (1977). "Correction for spectral artifacts in cross-sectional reconstruction from x rays." Med Phys 4(1): 54-7.

Redpath, A. T. and T. M. Kehoe (1999). Simulator Computed Tomography. The Modern Technology of Radiation Oncology. J. Van Dyk. Madison, Medical Physics Publishing.

Ruchala, K. J., G. H. Olivera, E. A. Schloesser and T. R. Mackie (1999). "Megavoltage CT on a tomotherapy system." Phys Med Biol **44**(10): 2597-621.

Van Dyk, J. and J. S. Taylor (1999). CT Simulators. The Modern Technology of Radiation Oncology. J. Van Dyk. Madison, Medical Physics Publishing.

No text.

# 4 Results and Discussion

This chapter presents the experimental results of the sinogram merging and iterative sinogram augmentation techniques. Results are compared to truncated images, to demonstrate the benefit of using such techniques, and to non-truncated images, to evaluate how well the techniques perform. The evaluation of the techniques is both qualitative and quantitative. Qualitative evaluation consisted of viewing the images at different window and level settings to look for artifacts created by the techniques, and also comparing profiles through images. Quantitative comparisons of reconstructed images were also performed using the image GOF and Bias measures described in the previous chapter.

This chapter is separated into results obtained from axial (sequential) and spiral scanning. Axial results consist of transverse images ( $x-y$ ) whereas spiral results deal with sagittal ( $z-y$ ) and coronal ( $z-x$ ) images. A detailed discussion of artifacts created by the sinogram merging technique is presented, and includes the effect of positioning errors in the  $x$ - and  $z$ -directions, and the effect of the stationary couch. Also discussed is the number of subsets required in the iterative sinogram augmentation technique. The advantages and disadvantages of each technique are discussed and remarks on the clinical implementation of these techniques are made. Before presenting the results of the two techniques, the results of the source-to-axis distance measurement and the calibration are presented.

## 4.1 Experimental Setup and Parameters

### 4.1.1 Source-to-Axis Distance

Figure 4-1 shows the magnification,  $M$ , of the wire on film as a function of the distance between the wire and film,  $r$ . The error in the length of the wire,  $\sigma_l$ , is negligible since the wire is machined to 0.003 cm accuracy. The error in

measuring the length of the wire,  $\sigma_{l_2}$ , off of the film using a ruler is estimated to be 0.05 cm. The error in the magnification,  $\sigma_M$ , is 0.01 and this value is the ordinate error bars. Simple linear regression gives a fit to the data of,

$$M = (0.0159 \pm 0.002)r + (1.002 \pm 0.003) \quad (2.61)$$

with a correlation coefficient of 0.9997. This corresponds to a source-to-axis distance of  $(62.9 \pm 0.8)$ cm.

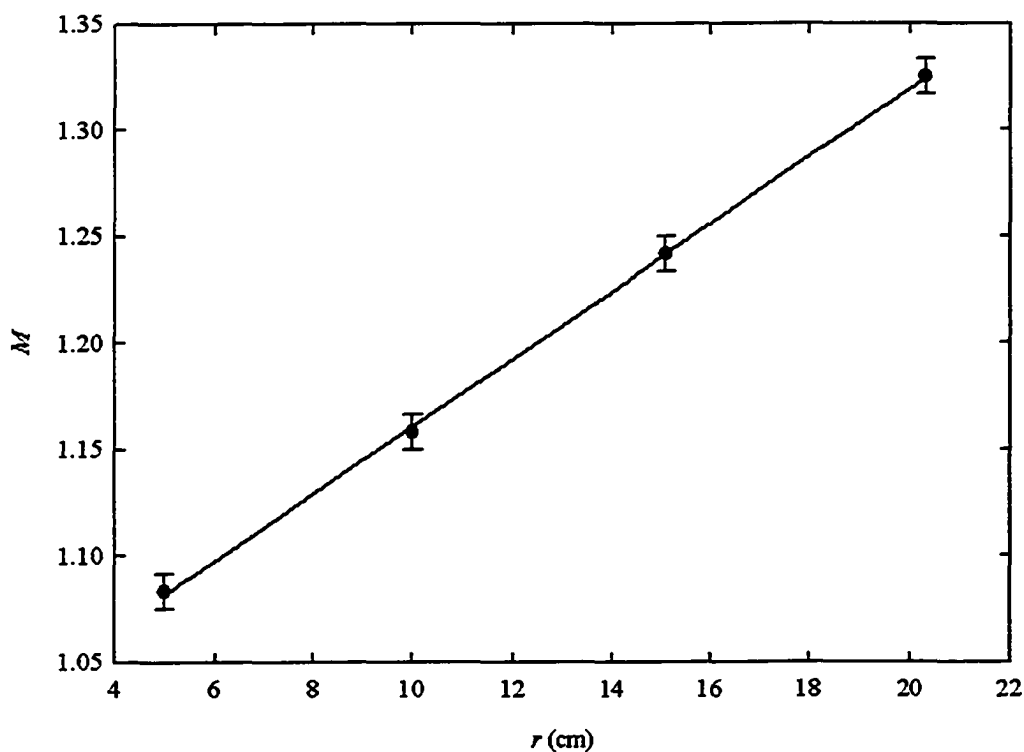


Figure 4-1 – Determination of source-to-axis distance,  $D$ , by measuring the magnification,  $M$ , of a known length of wire on film at a distance  $r$  away.

The source-to-axis distance of 62.9 cm was used to reconstruct a reference image from an acquired sinogram. Subtracting the Picker image from our image, Figure 4-2(a), reveals that the phantom sizes do not match. To obtain the same phantom width in our image as in the Picker's image it is necessary to increase the source-to-axis distance to 64.5 cm. Figure 4-2(b) shows the difference image between the Picker image and our image at this new source-to-axis distance.

Changing the value of the source-to-axis distance  $D$  within this range simply changes the size of the phantom in the image. The radius of the detector ring  $E$ , which is determined from the physical width of the detectors  $\tau$ , also affects the size of the phantom. Instead of modifying the parameters  $\tau$ ,  $E$ , and  $D$  together to obtain the correct phantom size, it was chosen to only modify the experimentally determined value for  $D$ , and the documented parameter  $\tau$ , which determines  $E$ , is taken to be correct. Using the value of  $\tau$  to determine the radius of the detector ring  $E$  assumes there is no space between each of the detector elements which may not be true. However, the image we obtained using the above stated parameters gives an image with good quality and the correct phantom size. It is possible that the Picker scanner uses the value of 64.5 cm as the source-to-axis distance in its reconstruction algorithm in order to obtain the correct phantom size in the image.

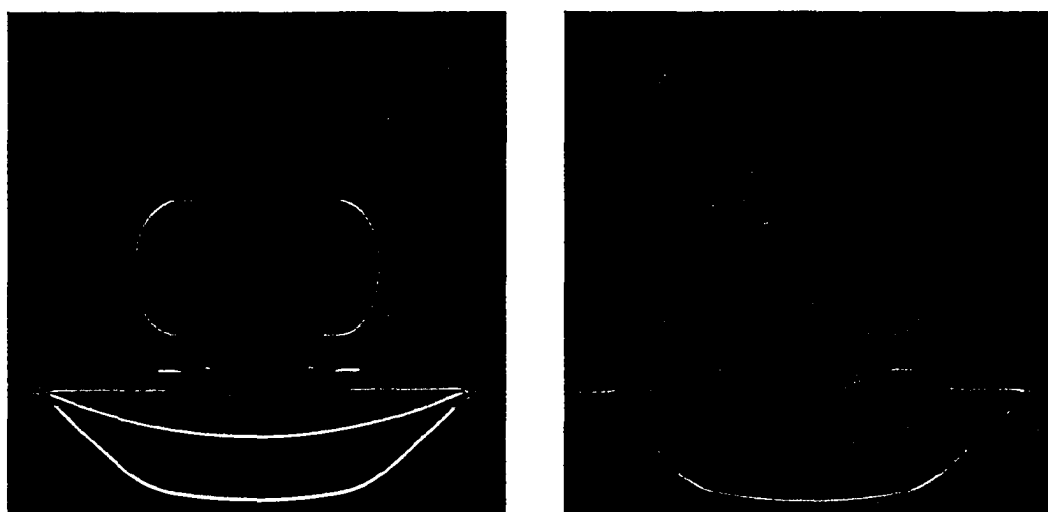


Figure 4-2 – Effect of varying source-to-axis distance  $D$ . Images are the difference between our image at a given  $D$  and the Picker image. (a)  $D = 62.9$  cm (b)  $D = 64.5$  cm.

### 4.1.2 Calibration Curve

Figure 4-3 shows the calibration curve used to convert our normalized image pixel values to values that have the same scaling as those in the Picker images. Our values are converted into HU (plus 1000) using Eq. (2.58). Performing linear

regression indicates that the Picker values  $y$  can be obtained from our values  $x$  by,

$$y = (1.026 \pm 0.004)x - (32 \pm 5). \quad (2.62)$$

The correlation coefficient of this linear fit is 0.9999. Our normalized values are converted to Picker values using this curve so our images have the same intensity scaling as the Picker images. The slope deviates from 1 as a result of the error in estimating  $\mu^m$ . All further reconstructions utilize this calibration curve to give correctly scaled pixel values.

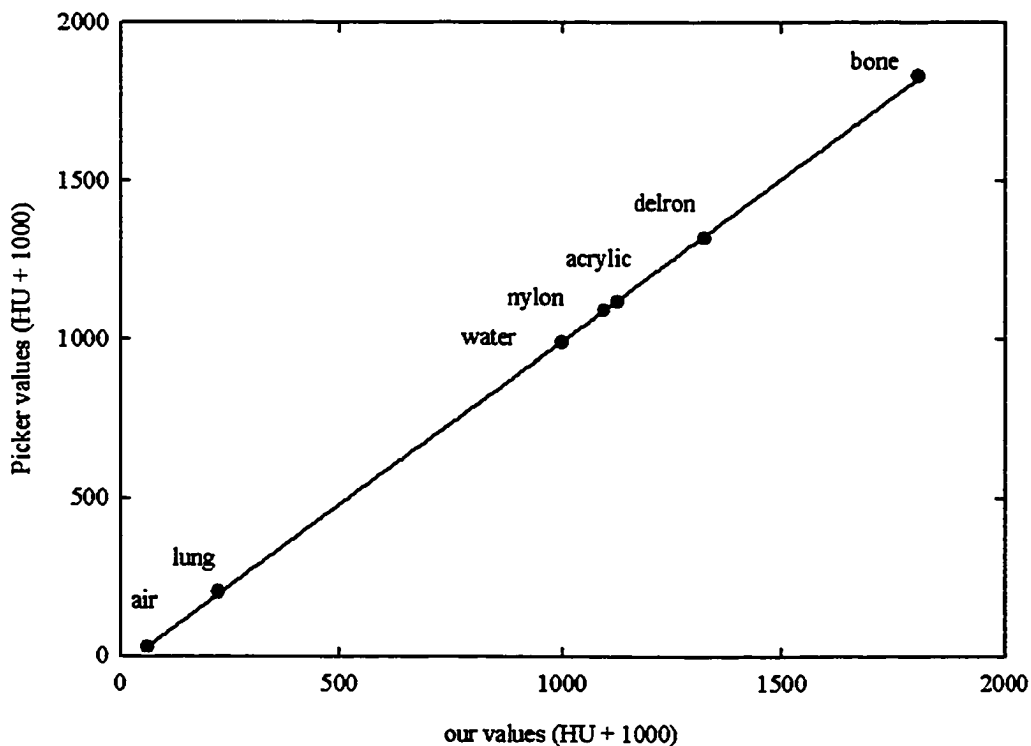


Figure 4-3 – The calibration curve derived from comparing our normalized image to the Picker image. Note that the error bars in the  $x$ - and  $y$ -axes are too small to see.

## 4.2 Axial Results

Figure 4-4 displays the axial reference image used for qualitative and quantitative analysis. The region outlined by the white dotted line is used in the GOF and Bias calculations. The axial slices have dimensions of 512 x 512 pixels (48 cm x



48 cm) but are cropped in the  $x$  and  $y$ -directions to 36 cm x 36 cm for display purposes. All images are displayed using the same window and level, 400 and 1000 (HU + 1000), respectively.

Truncated images for 24, 22, and 20 cm FOVs are illustrated in Figure 4-5. As the FOV becomes smaller and the acquired sinogram more truncated, the bowl artifact becomes more severe. The circular artifact at the edge of the FOV becomes more pronounced and the pixel values within the FOV become more inaccurate. Although the sinogram data is measured correctly within the FOV, the bowl artifact in the image appears as a result of the reconstruction process. The process of FBP requires that all the line integrals be measured over the whole object and at all angles of projection for an accurate reconstruction of the object (Gore and Leeman 1980). This requirement can be explained by the non-local nature of the ramp filter (Noo, Defrise et al. 2002). Parts of the object that are missing at some projection angles are not properly reconstructed, and produce artifacts that extend into the FOV and quantitative errors in the pixel values within the FOV. The severity of the artifacts depends on the amount of sinogram truncation, and can impose limitations on the ability to use the images for qualitative and quantitative purposes.

Merged images for the same FOVs are presented in Figure 4-6. The acquired fan-beam sinograms are merged at +3.94 cm and -3.94 cm. These offset values were determined using the cross correlation on left and right non-truncated images as described in Section 3.3.2.1. The impact of their accuracy on the sinogram merging technique will be discussed in Section 4.2.2.2. The images that are produced using the sinogram merging technique have significantly reduced artifacts compared to their corresponding truncated image. Parts of the object that are not properly reconstructed in the truncated images are visible in the merged images as a result of the increased FOV in the shifted direction. For each image Figure 4-6(a)-(c) the net FOV is illustrated in (d)-(f), respectively. The physical width of the net FOV in Figure 4-6(a), for example, is 31.88 cm (i.e. 24 cm + 2 x 3.94 cm).

In the merged images with FOVs of 24 and 22 cm (Figure 4-6(a) and (b)) there is some clipping of the phantom's platform. This is because the phantom, rather than the phantom/platform combination, was positioned at the vertical center of the FOV. Thus, the bottom of the platform was clipped while the top of the phantom was properly reconstructed. When the FOV is decreased to 20 cm and the offset is only  $\pm 3.94$  cm, the net FOV has a width of only 27.88 cm compared to a phantom width of 30 cm. Since the entire width of the phantom is not covered by the merged scans, a bowl artifact occurs in the reconstructed image (Figure 4-6(c)). The magnitude of this artifact is noticeably less, however, than the bowl artifact seen in Figure 4-5(c).

Images produced using the iterative sinogram augmentation technique are shown in Figure 4-7. These augmented images have significantly less bowl artifact than the truncated images in Figure 4-5. The ring at the edge of the FOV is diminished and the error in the pixel values inside the FOV is decreased. The iterative sinogram augmentation technique reduces artifacts inside the FOV but does not estimate structures outside the FOV very well. To demonstrate the improvement inside the FOV compared to the truncated images, Figure 4-7(d)-(f) displays the augmented images (a)-(c) with a mask that is the size of the corresponding FOV.

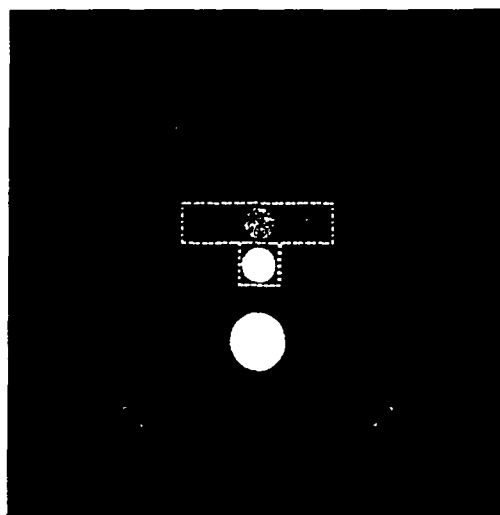


Figure 4-4 – Reference image of the CIRS 002LFC phantom positioned at the axis. The rectangular outline defines the region used in quantitative analysis.

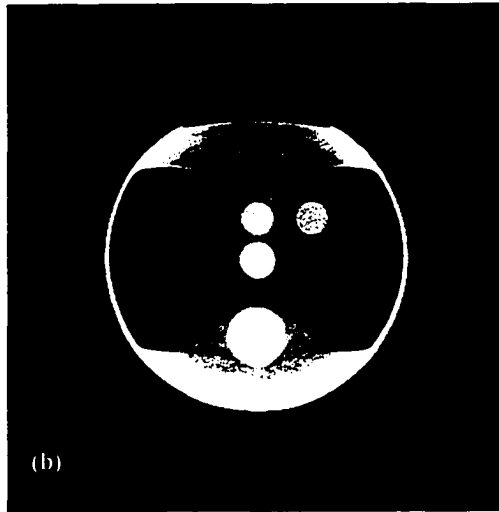
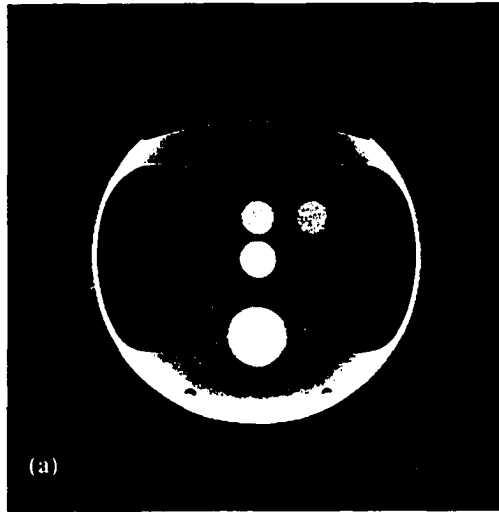


Figure 4-5 – Truncated images for FOVs of (a) 24 cm (b) 22 cm and (c) 20 cm. Images are shown in a window of 400 and level of 1000 (HU + 1000).

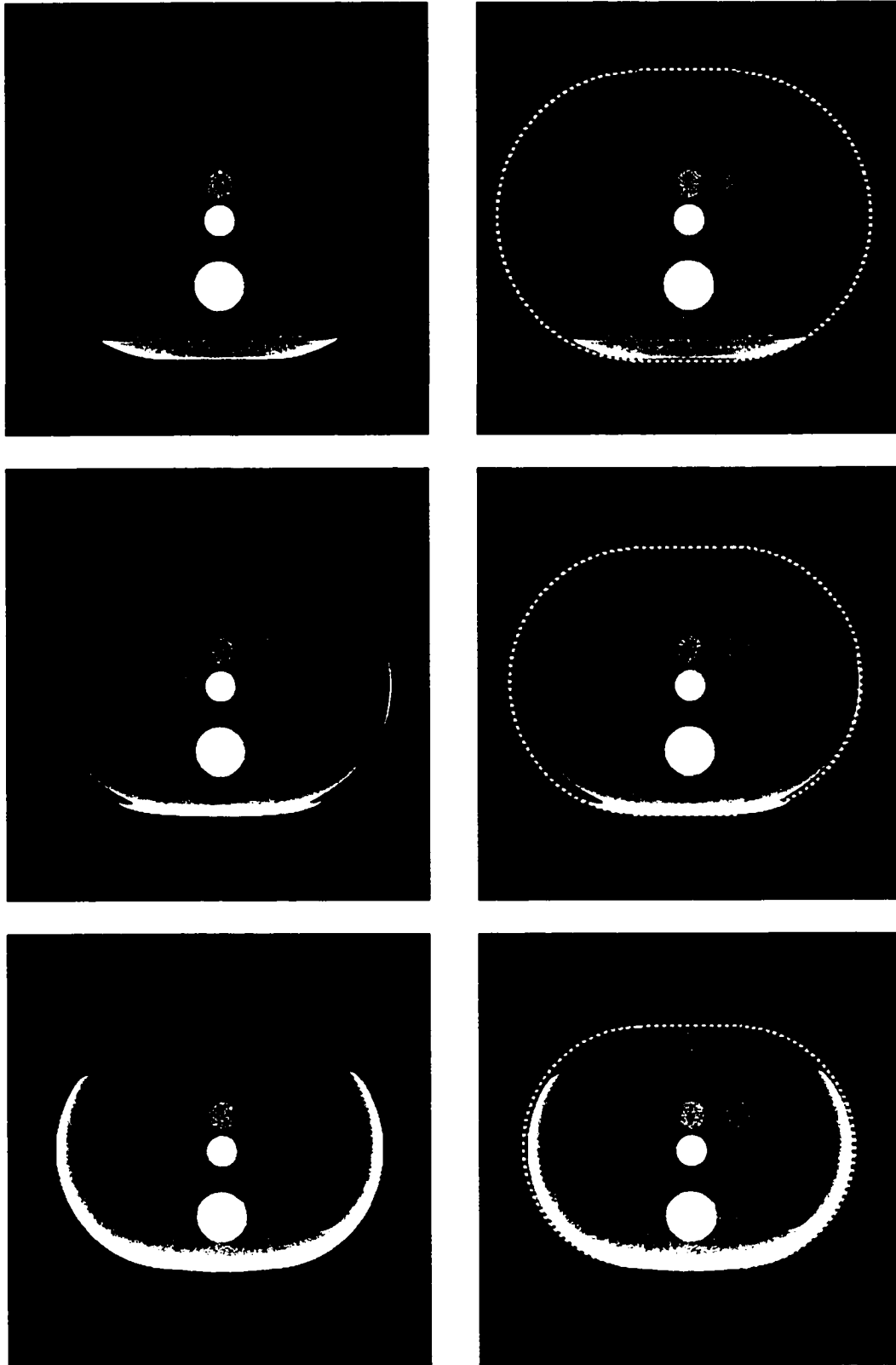


Figure 4-6 – Merged images for FOVs of (a) 24 cm (b) 22 cm and (c) 20 cm. (d)-(f) same as (a)-(c) but overlaid with net FOV. The offset distance is  $\pm 3.94$  cm. Images are shown in a window of 400 and level of 1000 (HU + 1000).

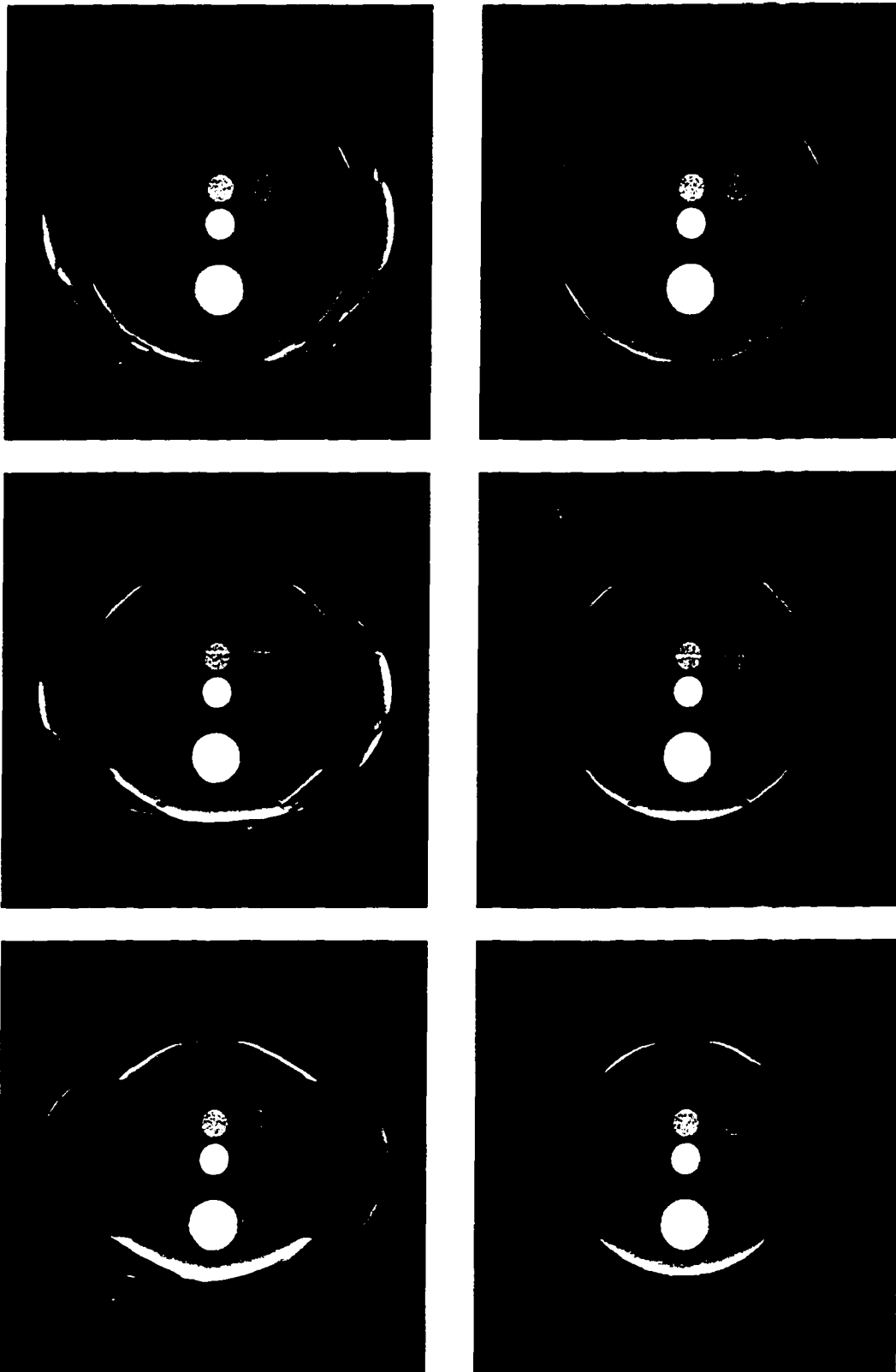


Figure 4-7 – Augmented images for FOVs of (a) 24 cm (b) 22 cm and (c) 20 cm. (d)-(f) same as (a)-(c) but masked to FOV. Images are shown in a window of 400 and level of 1000 (HU + 1000).

## 4.2.1 Analysis

### 4.2.1.1 Profiles

Profiles through each type of image and FOV are plotted in Figure 4-8. Each plot contains profiles through the center (i.e.  $y = 255$ ) of the truncated, merged, and augmented images as well as the reference image (Figure 4-4). For the 24 cm FOV, Figure 4-8(a), the truncated image profile exhibits a sharp rise in pixel values at the edge of the FOV. There is also an increase in pixel values inside the FOV. The merged image profile is significantly improved from the truncated image profile. The net FOV is increased and covers the full extent of the object making the merged image profile almost indistinguishable from the reference image profile. The augmented image profile also closely matches the reference image profile inside the FOV, but pixel values outside of the FOV deviate considerably from the reference profile.

For the 22 cm FOV, Figure 4-8(b), the truncated image profile exhibits slightly increased pixel values in the central portion of the FOV compared to the 24 cm FOV profile. The merged image profile closely resembles that of the reference, apart from the small spike on the right-hand side of the profile. This spike results from the fact that the net FOV width of 29.88 cm is slightly smaller than the 30 cm width of the phantom, and thus the FOV clips the edge of the phantom in the image. The augmented image profile indicates that the iterative augmentation technique performs well inside the FOV but again does not accurately predict regions outside the FOV.

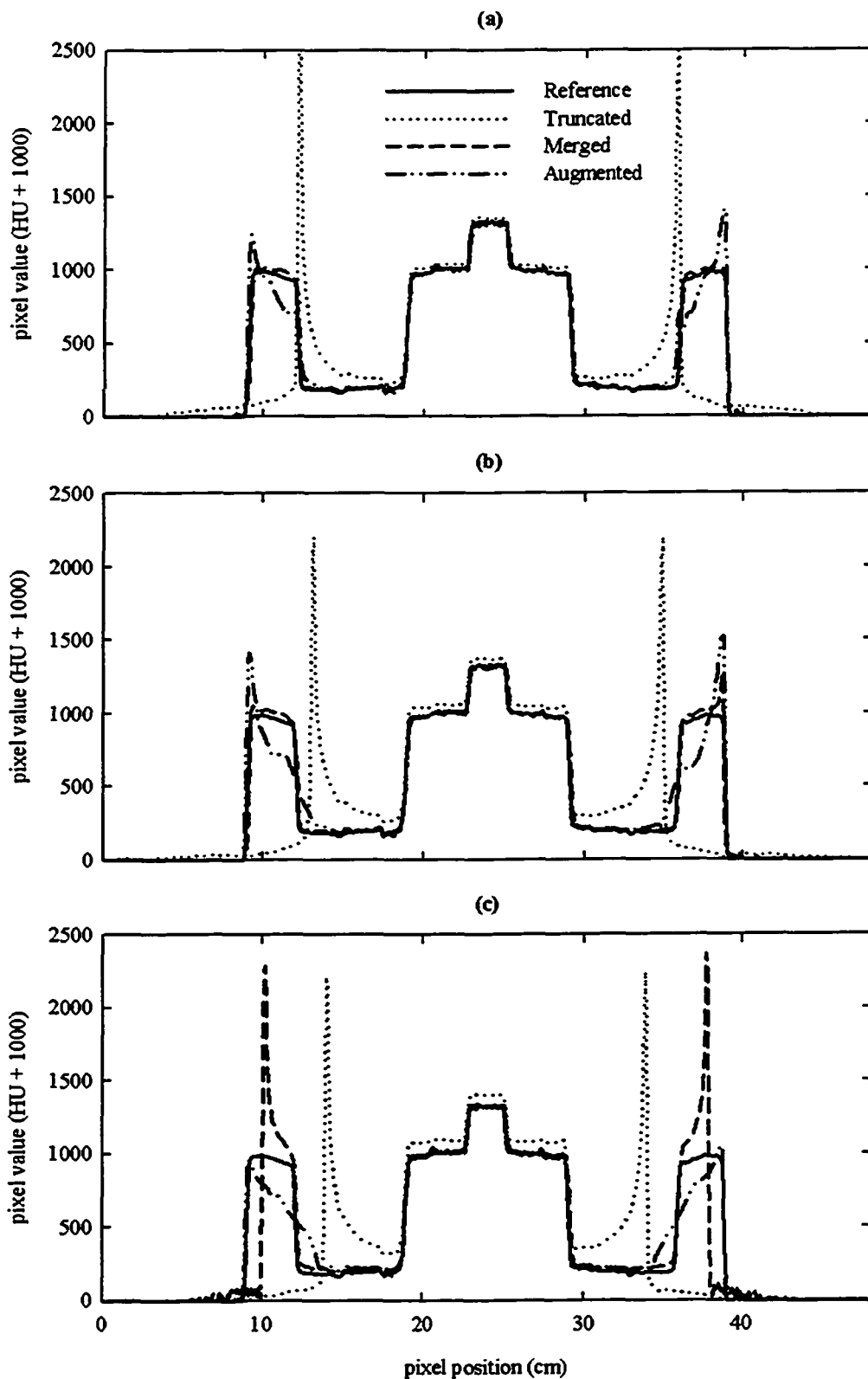


Figure 4-8 – Profiles through each axial image; reference, truncated, merged, and augmented for (a) 24 cm field-of-view (FOV), (b) 22 cm FOV, and (c) 20 cm FOV. Profiles are taken at line  $y = 255$ .

For the 20 cm FOV, Figure 4-8(c), the bowl artifact becomes magnified in the truncated image profile. The pixel values are increased inside the FOV compared to the 22 cm FOV profile, and the rise at the edge becomes more pronounced. The merged image profile closely resembles the reference image profile inside the FOV but due to the size of the FOV (20 cm) and the offset location ( $\pm 3.94$  cm) the net FOV is not increased enough to accurately reconstruct the entire object. Bowl artifacts result at the edge of the 27.88 cm net FOV since the phantom's width exceeds this value. In this case, a larger offset location can be used to increase the net FOV further as shown in Section 4.2.3. The augmented image profile displays accurate pixel values inside the FOV but again the pixel values outside the FOV deviate from the reference image profile.

#### **4.2.1.2 Quantitative Analysis**

Quantitative analysis for axial images is presented in Table 4-1, which contains the image GOF and Bias measures for the truncated images and the images produced from each truncation artifact reduction method. The image GOF and Bias is calculated between the reference image and the corresponding truncated, merged, or augmented image using Eq. (2.60) in the defined region outlined in Figure 4-4. The quantitative accuracy of the pixel values is essential for accurate treatment planning and verification (Ruchala, Olivera et al. 2002b) and these parameters provide a measure of the degree of accuracy.

For the truncated images, the GOF and Bias values both increase with a decreasing FOV. Since the Bias values are the same as the GOF values, at each FOV, all of the pixel values in the defined region of the truncated image are higher than in the reference image. The decrease in GOF values for both the merged and augmented images indicate an improvement from the truncated images, with the augmented images being slightly more improved. For the merged images, the GOF values for the 24 cm and the 22 cm FOVs are approximately the same. Once the net FOV is smaller than the object, however, as in the 20 cm FOV, the GOF value displays a slight increase in the defined region. The Bias values display an increasing trend with a decreasing FOV. As



the FOV decreases, the Bias value begins to match that of the GOF in the merged images. This is because the increase in pixel values (i.e. the bowl artifact) becomes the predominant artifact when the net FOV is smaller than the object. For the augmented images, both the GOF and Bias values increase with a decreasing FOV as the pixel values in the defined region of the augmented image become higher than in the reference image. As the FOV gets smaller, and the bowl artifact is increased, the iterative sinogram augmentation technique does not perform as well.

The GOF may reach a minimum value that is not necessarily zero due to a level of noise in the images. To estimate the level of noise, the GOF is calculated between two different reference images. Note that a reference image is an image reconstructed from a full FOV sinogram where the phantom is positioned at the axis. Two sets of sinogram data were acquired with the phantom positioned at the axis and each was then used to reconstruct an image. The reference images are therefore identical except for the noise in each. The GOF value between the two different reference images was found to be 0.010. The GOF values in Table 4-1 may be measured with respect to this noise baseline. Relative differences in the GOF value between each FOV in the table are not affected by this value.

Table 4-1 – The image goodness-of-fit (GOF) and Bias measures for each type of axial image: truncated, merged, and augmented. The measures are calculated in a defined region, which is outlined in Figure 4-4, for each field-of-view (FOV): 24, 22, and 20 cm.

FOV (cm)	Truncated		Merged		Augmented	
	GOF	Bias	GOF	Bias	GOF	Bias
24	0.127	0.127	0.051	0.010	0.012	0.008
22	0.230	0.230	0.053	0.018	0.023	0.022
20	0.375	0.375	0.066	0.047	0.050	0.050

#### 4.2.1.3 Number of Subsets

In the iterative sinogram augmentation technique, a sinogram GOF can be calculated comparing the estimated sinogram, derived using the OS-ML-EM

algorithm, to the measured sinogram (see Section 3.3.3.1). Sinogram GOF values, as a function of the number of full-iterations, are plotted in Figure 4-9 for up to 10 full-iterations, and for various numbers of sub-iterations per full-iteration. The variants with 120 and 600 sub-iterations per full-iteration are almost identical to the variant with 240 sub-iterations, and are therefore not shown in the figure. It was found that all the variants investigated required essentially the same amount of computer time to process each full-iteration.

As the number of sub-iterations per full-iteration increases, the sinogram GOF values decreases for a fixed number of full-iterations. In particular, while the variant with only 1 sub-iteration per full-iteration (i.e. the basic ML-EM algorithm) converges slowly over a number of full-iterations, the variant with 240 sub-iterations converges quickly and reaches a close-to-optimum GOF value after only 1 or 2 full-iterations.

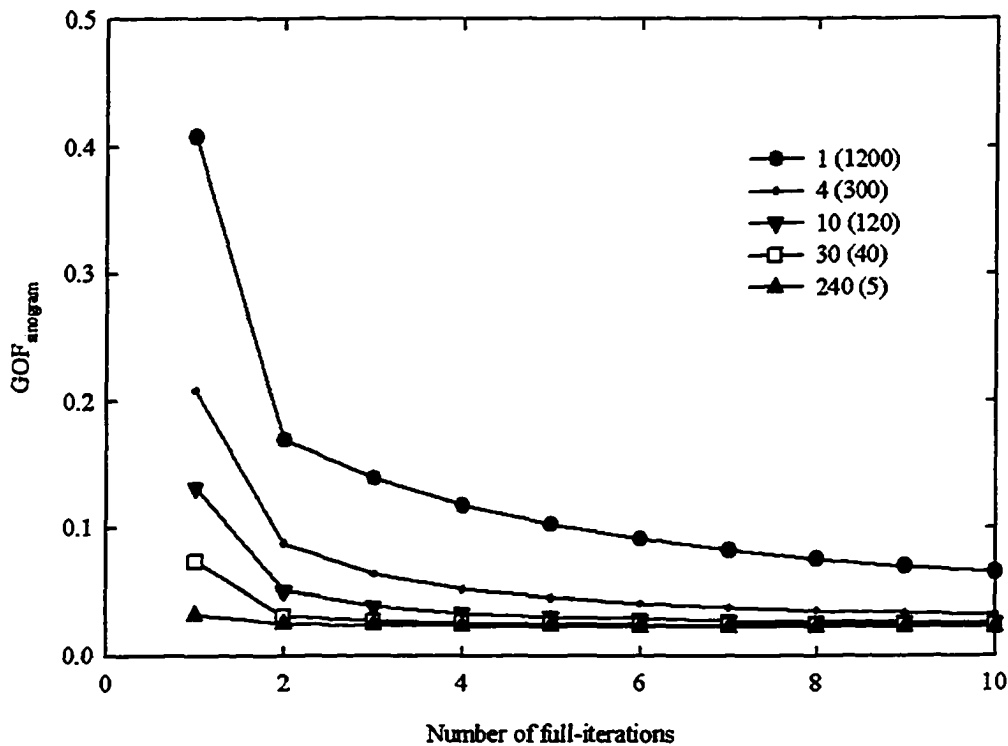


Figure 4-9 – Sinogram goodness-of-fit ( $GOF_{\text{sinogram}}$ ) as a function of the number of full-iterations for various subsets investigated in the iterative sinogram augmentation technique. Legend indicates the number of sub-iterations per full-iteration followed by the number of sinograms rows used in each sub-iteration in parentheses.

## 4.2.2 Sinogram Merging Technique – Artifacts

### 4.2.2.1 General Artifacts

Ideally the sinogram merging technique would produce an image as good as the reference image displayed in Figure 4-4. In comparing the merged image of Figure 4-10 to the reference image, several points may be noted. First, there is clipping of the platform even for the largest FOV of 24 cm. The platform was positioned below the net FOV and thus projection data from parts of the platform were missing from both of the acquired sinograms. This results in a bowl artifact around the edges of the platform. Second, the couch produces an artifact, indicated by the arrow in Figure 4-10, that is symmetric about the  $y$ -axis. The couch, on which the phantom and platform rest, is included in the airscan in order to minimize its affect on the merging algorithm. Its effects on the merging technique will be discussed further in Section 4.2.2.3 below. Lastly, the streak artifacts that are visible in the water equivalent structure are considered to be due to the fan-to-parallel interpolation at high gradient boundaries. Although minor in the reference image, these streak artifacts are amplified in the merged image possibly because of a slight positioning error in the shifted scans.

### 4.2.2.2 Positioning Error

The sinogram merging technique requires two sets of truncated fan-beam sinograms that are acquired with the phantom shifted laterally within the gantry. To merge the acquired sinograms, the technique requires the user to enter the offset location  $(x_c^{(i)}, y_c^{(i)})$  for each sinogram  $i$ . The accuracy of the offset locations is crucial to the success of the merging technique. The effect of a lateral positioning error in the sinogram merging technique is illustrated in Figure 4-11. The acquired fan-beam sinograms were merged at offset values of  $\pm 4.00$  cm rather than  $\pm 3.94$  cm resulting in additional artifacts in the central region of the image, most notably at the interior edge of the lungs and around the bone. Assuming the cross correlation result to be the ‘correct’ offset value ( $\pm 3.94$  cm),

the net lateral offset error in Figure 4-11 is only 0.12 cm (i.e.  $2 \times 0.06$  cm). Although the positioning error is small, the impact of such an error on the merged image is visibly significant.

The finite pixel dimensions of the images cause the offset result from the cross correlation method to be quantized. The cross correlation method only serves to minimize the error in the offset location but does not necessarily reveal the true offset value of the left and right scans. The error in the cross correlation result is estimated to be half the pixel size or  $\pm 0.05$  cm, while the positioning error when using the sagittal lasers is larger at about  $\pm 0.2$  cm. The success of the sinogram merging technique is dependant upon the accuracy of knowing the offsets of the shifted phantom. Therefore, clinical implementation of this technique will require a couch with lateral translation that is, as this work suggests, accurate to 0.05 cm or less.

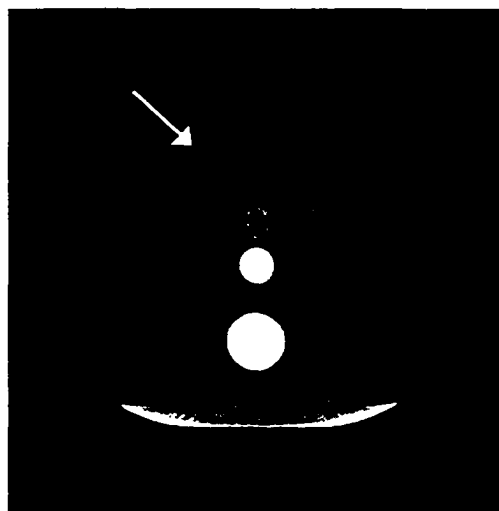


Figure 4-10 – Artifacts produced by the sinogram merging technique. Image is a merged image,  $\pm 3.94$  cm offset and 24 cm field-of-view (FOV). Arrow points to 'couch' artifact.

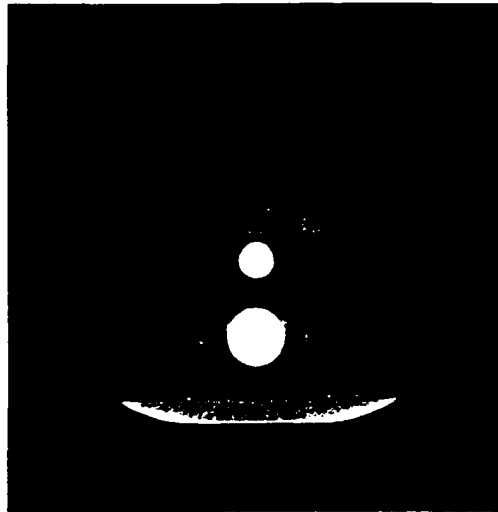


Figure 4-11 – Artifacts produced by a lateral offset error in the sinogram merging technique. Image is a merged image,  $\pm 4.00$  cm offset and 24 cm field-of-view (FOV). Lateral error is  $\sim 0.12$  cm in total.

### 4.2.2.3 Stationary Couch

Figure 4-12 illustrates the effect of the stationary couch on the sinogram merging technique. The homogeneous CIRS 002H5 phantom was chosen so that the effects of the couch can be differentiated from the effects of internal inhomogeneities in the phantom.

The phantom and platform had to be manually positioned at each offset location because the couch in the Picker CT scanner does not move laterally. In order to investigate the effects of the stationary couch the airscan was acquired both with and without the couch in the path of the x-ray beam. The images shown in Figure 4-12 are merged images for 24, 22, and 20 cm FOV and each FOV is shown using (a) the airscan without the couch and (b) the airscan with the couch for normalization. By including the couch in the airscan as in (b) the artifacts due to the couch are reduced. The ‘couch’ artifacts become closer together and begin to overlap as the FOV decreases. This is also observed in Figure 4-6 but is somewhat concealed by the lung. To eliminate these couch artifacts, the couch should translate laterally along with the phantom.



Figure 4-12 – Effect of the stationary couch in the sinogram merging technique. All images are merged images. Top row is 24 cm field-of-view (FOV), middle row is 22 cm FOV, and bottom row is 20 cm FOV. Transmission data normalized to (a) airscan without couch (b) airscan with couch. Images are shown in a window of 400 and level of 1000 (HU + 1000).

### 4.2.3 Improving the Image

When the net FOV is smaller than the phantom, as is the case in Figure 4-6(c), two options are available to improve the image: increase the offset distance, or use the iterative augmentation technique in conjunction with the merging technique. Figure 4-13(a) is identical to Figure 4-6(c), and displays the merged image from two 20 cm FOV scans with offset values of  $\pm 3.94$  cm. In the image displayed in Figure 4-13(b) the offset distance is increased to  $\pm 5.91$  cm and the net FOV is thus increased to 31.82 cm (i.e.  $20 \text{ cm} + 2 \times 5.91 \text{ cm}$ ). The sinogram merging technique recovers the full lateral extent of the phantom. However, since the FOV is only increased in the lateral direction, bowl artifacts still remain at the bottom of the phantom. Also, by increasing the offset distance, the couch artifacts move towards the image's central region.

The other option is to use the iterative augmentation technique to improve the image quality after using the merging technique. Figure 4-13(c) displays an image that is produced by augmenting the parallel-beam sinogram from the merged image shown in Figure 4-13(a). The augmented image displayed in Figure 4-13(c) has a reduced bowl artifact and more of the phantom and platform is recovered. The image shown in Figure 4-13(d) is produced by applying the iterative augmentation technique to the parallel-beam sinogram from the merged image in Figure 4-13(b). This cleans up the bowl artifact at the bottom of phantom so that more of the platform is visible.

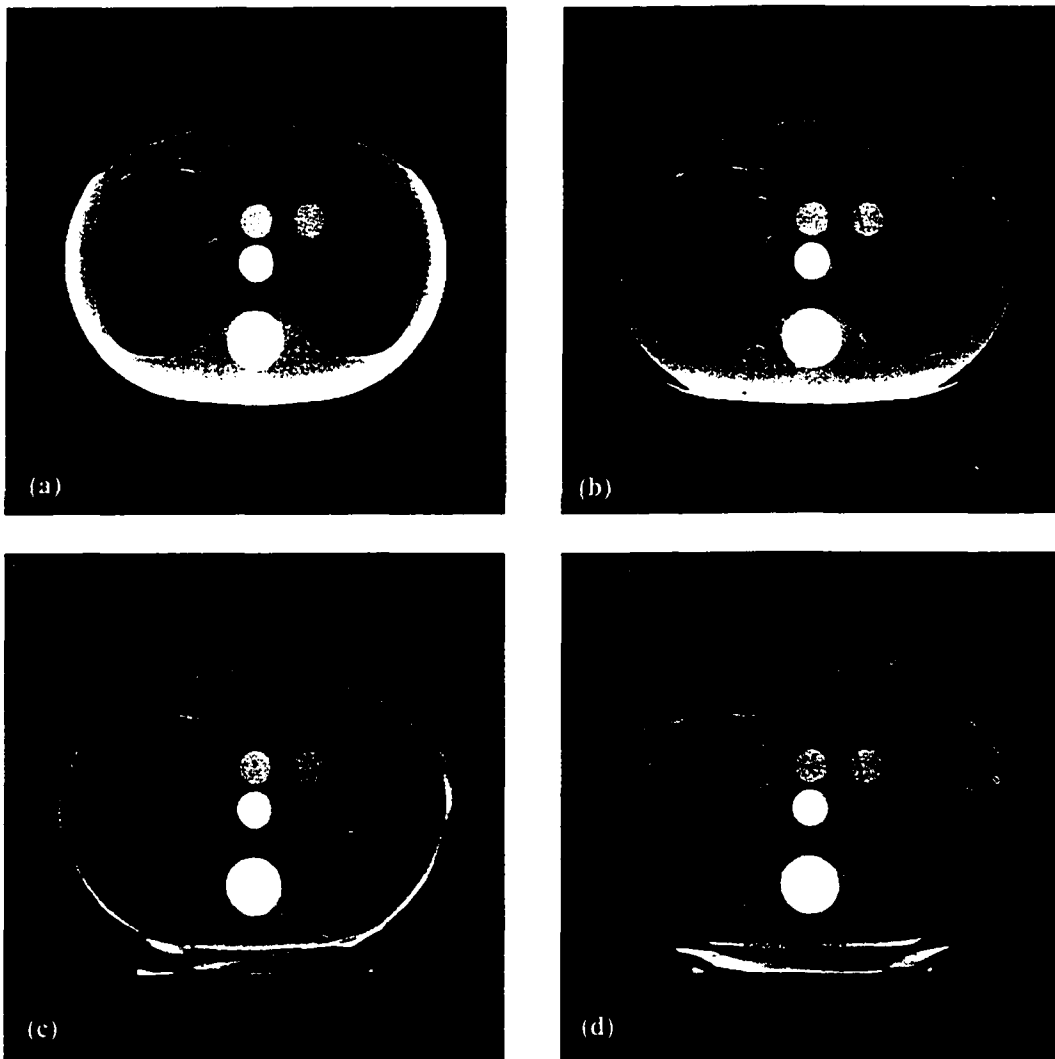


Figure 4-13 – Effect of increasing the offset distance and the complementary use of iterative augmentation to sinogram merging. (a) Merged image,  $\pm 3.94$  cm offset, 20 cm field-of-view (FOV). (b) Merged image,  $\pm 5.91$  cm offset, 20 cm FOV. (c) Augmented image using parallel-beam sinogram from (a). (d) Augmented image using parallel-beam sinogram from (b).

### 4.3 Spiral Results

Figure 4-14 displays the sagittal reference images for pitches of 2, 1.5, and 1. The sagittal slices are generated through the vertical center (i.e.  $x = 255$ ) of a series of axial slices with the orientation shown by the coordinate system in Figure 4-14. These slices have dimensions of 512 x 100 pixels (48 cm x 10 cm) but are cropped in the  $y$ -direction (sagittal) or  $x$ -direction (coronal) for display purposes. All images are displayed using the same window and level, 400 and 1000 (HU + 1000), respectively.



The 2, 1, and 0.5 cm spacer plugs are visible as alternating grey (acrylic) and black (air) spaces along the  $z$ -axis. As the pitch decreases the longitudinal spatial resolution improves. The 0.5 cm spacer plug is clearly distinguishable at all pitches, although longitudinal resolution decreases as pitch increases. Streak artifacts in the  $y$ -direction occur at pitches of 1.5 and 2, and increases in magnitude as the pitch increases. These are caused by pin-wheel artifacts in the series of axial slices (not shown) used to generate the sagittal slice. Artifacts of this type result from inadequate sampling, and the resulting spiral interpolation errors, in the longitudinal direction.

Figure 4-15 illustrates truncated images for a FOV of 20 cm for each pitch. The pixel values in these images are severely distorted as a result of the sinogram truncation. Truncated images are significantly improved by using either the sinogram merging or iterative sinogram augmentation technique. Figure 4-16 and Figure 4-17 display the merged and augmented images, respectively, for the same FOV and pitches as the truncated images.

For the merged images shown in Figure 4-16, two 20 cm FOV sinogram data sets were acquired by scanning the phantom at  $\pm 5.93$  cm offset positions in order to recover the full width of the phantom and reduce artifacts. There is, however, still some clipping of the platform as the FOV is only increased in the  $x$ -direction. Also, the streak artifacts that can be observed throughout the water equivalent structures, at all pitches, result from the error in estimating the offset positions of the left and right scans. Overall, the merged images are in good agreement with the reference images shown in Figure 4-14. Although, the data is truncated and acquired at different offset locations, the sinogram merging technique is capable of producing sagittal images with quality comparable to that of the reference images.

As discussed previously in Section 2.3.1.2, the phase angle between the shifted scans plays a role in the longitudinal resolution of the merged images. For a phase angle of  $\pm 90^\circ$ , the longitudinal resolution is suspected to be improved in the region where the shifted FOVs overlap. However, none of the acquired sinograms have a phase angle close enough to  $90^\circ$  to notice an improvement. The

phase angles for the merged images, in order of decreasing pitch are approximately 10°, 60°, and, 167°. Unfortunately the source start angle, which determines the phase angle, cannot be specified in spiral scanning on the CT scanner used for these experiments.

Figure 4-17 displays the augmented images for a 20 cm FOV and for each pitch investigated. A series of 20 cm FOV parallel-beam sinograms were each processed using the iterative augmentation technique to produce a set of axial images which were subsequently used to generate the sagittal slices shown. These sagittal slices have reduced artifacts compared to the truncated images shown in Figure 4-15. Although the region inside the FOV closely resembles that of the reference images for each pitch, there still exists a significant amount of bowl artifact at the posterior location of the phantom where the platform is not properly estimated by the iterative augmentation technique. There is also a small amount of bowl artifact that can be seen at the anterior location of the phantom. The remaining bowl artifact seen in the sagittal images is consistent with that observed in the axial images in Figure 4-7(c). Inside the FOV, the augmented images are in good agreement with the reference images. The streak artifacts that were visible in the water equivalent structures of the merged images shown in Figure 4-16 do not exist in the augmented images.

Figure 4-18 illustrates coronal slices for the reference, truncated, merged, and augmented images at a pitch of 1.5. The coronal slices are generated through the horizontal center (i.e.  $y = 255$ ) of a series of axial slices, going through the 0.5 cm spacer plug. The reference image displayed in Figure 4-18(a) has accurate pixel values and the full width of the phantom is visible. The FOV of the truncated image shown in Figure 4-18(b) is reduced to 20 cm and limits the amount of the phantom that can be used for clinical evaluation. The bowl artifact obscures the anatomy at the periphery of the FOV and increases in magnitude the central pixel values. Images reconstructed from truncated sinograms are improved using either the sinogram merging technique (Figure 4-18(c)) or the iterative sinogram augmentation technique (Figure 4-18(d)). The merged image has an increased FOV which allows the full width of the phantom to be evaluated.

The augmented image has reduced artifacts inside the FOV but the region outside the FOV is poorly represented. This highlights the main difference between the two techniques. The sinogram merging technique will improve image quality inside an enlarged FOV, while the iterative sinogram augmentation technique will only improve image quality inside the truncated FOV.

## **4.3.1 Analysis**

### **4.3.1.1 Profiles**

Profiles through the sagittal and coronal image slices for each image type are displayed in Figure 4-19. There is negligible difference between profiles at each pitch hence the profiles are only plotted for a pitch of 1.5. The location of the profiles in the sagittal and coronal slices is illustrated in Figure 4-20. For the sagittal image profiles shown in Figure 4-19(a), the truncated image profile exhibits higher pixel values than the reference image profile and large spikes in pixel values at the edges of the FOV. The merged and augmented image profiles differ marginally from the reference profile apart from the predominant spike in pixel values on the right-hand side of the plot (posterior location on phantom). Neither technique improves the image at the posterior end of the phantom where the platform remains clipped in the truncated, merged and augmented images.

Coronal image profiles are shown in Figure 4-19(b). The edges of the 20 cm FOV are indicated by the sharp rise in pixel values at the periphery of the truncated image profile. The merged image profile has an increased FOV and is almost identical to the reference image profile. Structures that are outside of the FOV are properly represented when the sinogram merging technique is utilized. The augmented image profile is indistinguishable inside the 20 cm FOV but pixel values outside the FOV boundary diverge from the reference profile.

### **4.3.1.2 Quantitative Analysis**

The image GOF and Bias values for sagittal and coronal slices are presented in Table 4-2. Both measures are calculated for truncated, merged and augmented

images at each pitch using a rectangular defined region that is 19.5 cm wide x 10 cm high that is centered on each image. The sagittal and coronal slices used as the reference images in the calculation are generated from a series of non-truncated axial images acquired at the same pitch as the image in question. There is no variation in the values across pitches since each calculation, at a given pitch, uses the corresponding reference image at the same pitch.

For the truncated images, the GOF and Bias values are the same value as a result of the positive shift in pixel values (i.e. bowl artifact). The GOF and Bias values from truncated images are higher in the coronal slices than in the sagittal slices because of the dimensions of the phantom. Since the phantom is wider ( $x$ -direction) than it is thick ( $y$ -direction) more of the phantom is truncated in the  $x$ -direction leading to an increase in artifacts in the coronal slices. The GOF and Bias values are reduced in the merged and augmented images for both coronal and sagittal slices, with the coronal slices showing a larger reduction. For the merged images, the coronal slices show more improvement in the GOF and Bias values compared to the sagittal slices because the increase in the FOV is in the  $x$ -direction, which is represented in the coronal slice. The pixel values in the defined region of the merged images display a slight positive bias. For the augmented images, the GOF and Bias values are equal, which indicates that all pixel values inside the defined region of the augmented image are higher than in the reference image. Both artifact reduction techniques, merging and iterative augmentation, quantitatively improve the pixel values inside the FOV.

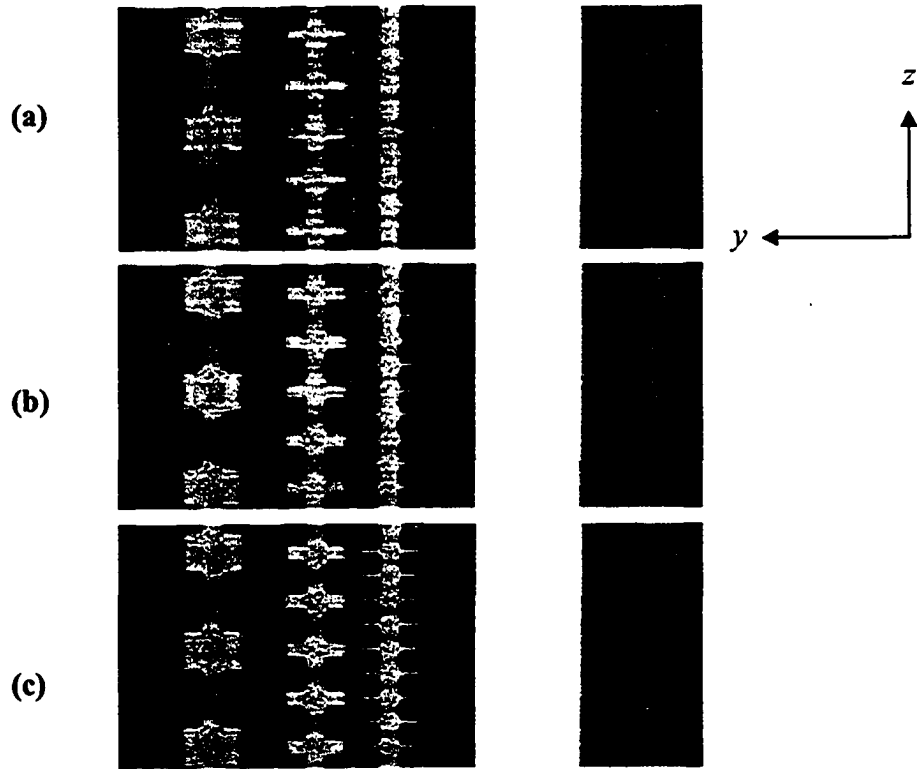


Figure 4-14 – Sagittal slices of reference images at a pitch of (a) 2, (b) 1.5, and (c) 1.0. Images are displayed using window of 400 and a level of 1000.

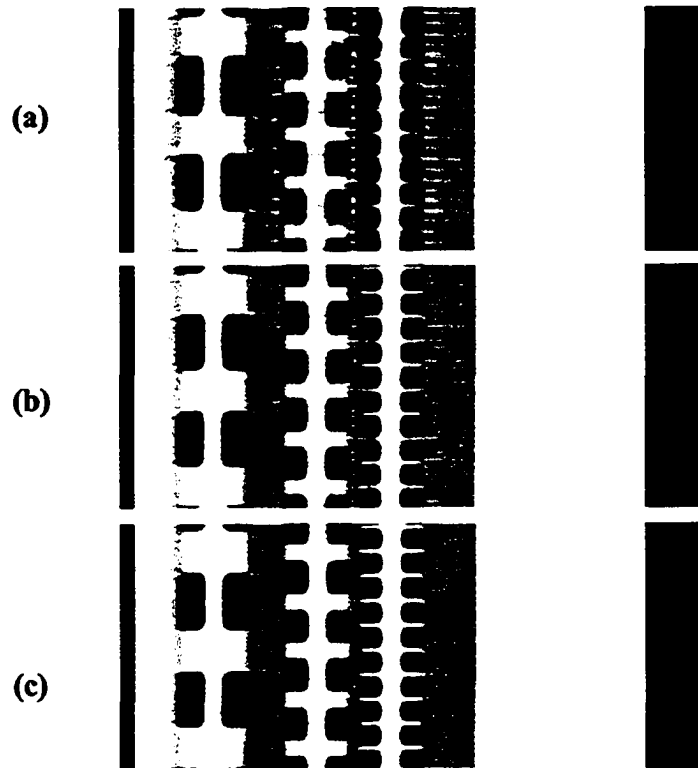


Figure 4-15 – Sagittal slices of truncated images with a 20 cm FOV at a pitch of (a) 2, (b) 1.5, and (c) 1.0. Images are displayed using window of 400 and a level of 1000.

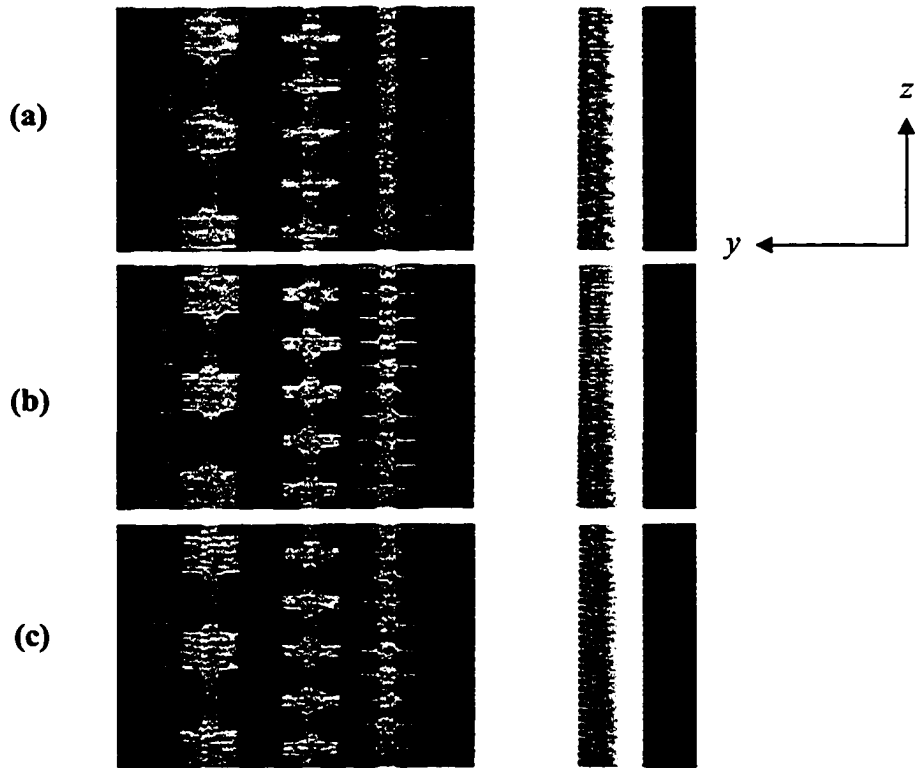


Figure 4-16 – Sagittal slices of merged images for 20 cm FOV and  $\pm 5.93$  cm offset at a pitch of (a) 2, (b) 1.5, and (c) 1.0. Images are displayed using window of 400 and a level of 1000.

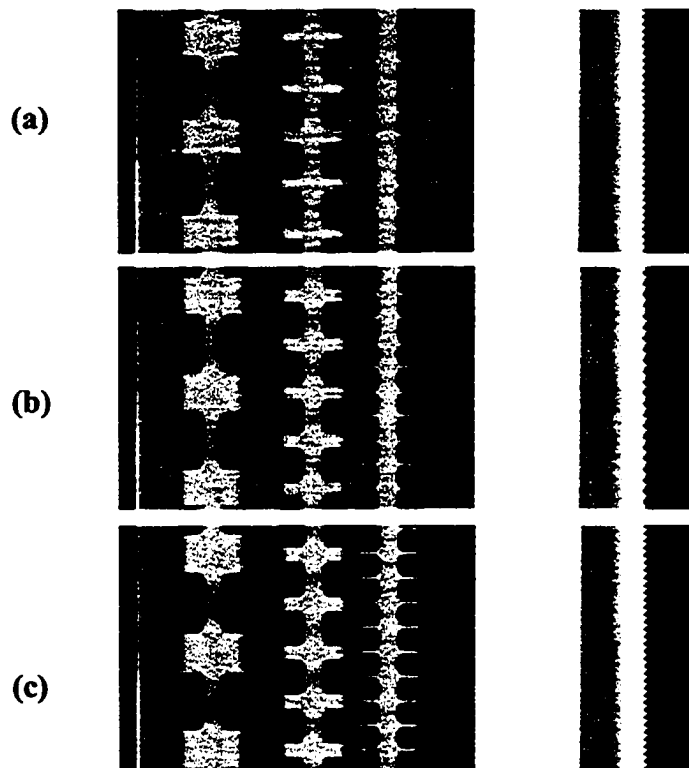


Figure 4-17 – Sagittal slices of augmented images with a 20 cm FOV at a pitch of (a) 2, (b) 1.5, and (c) 1. Images are displayed using window of 400 and a level of 1000.

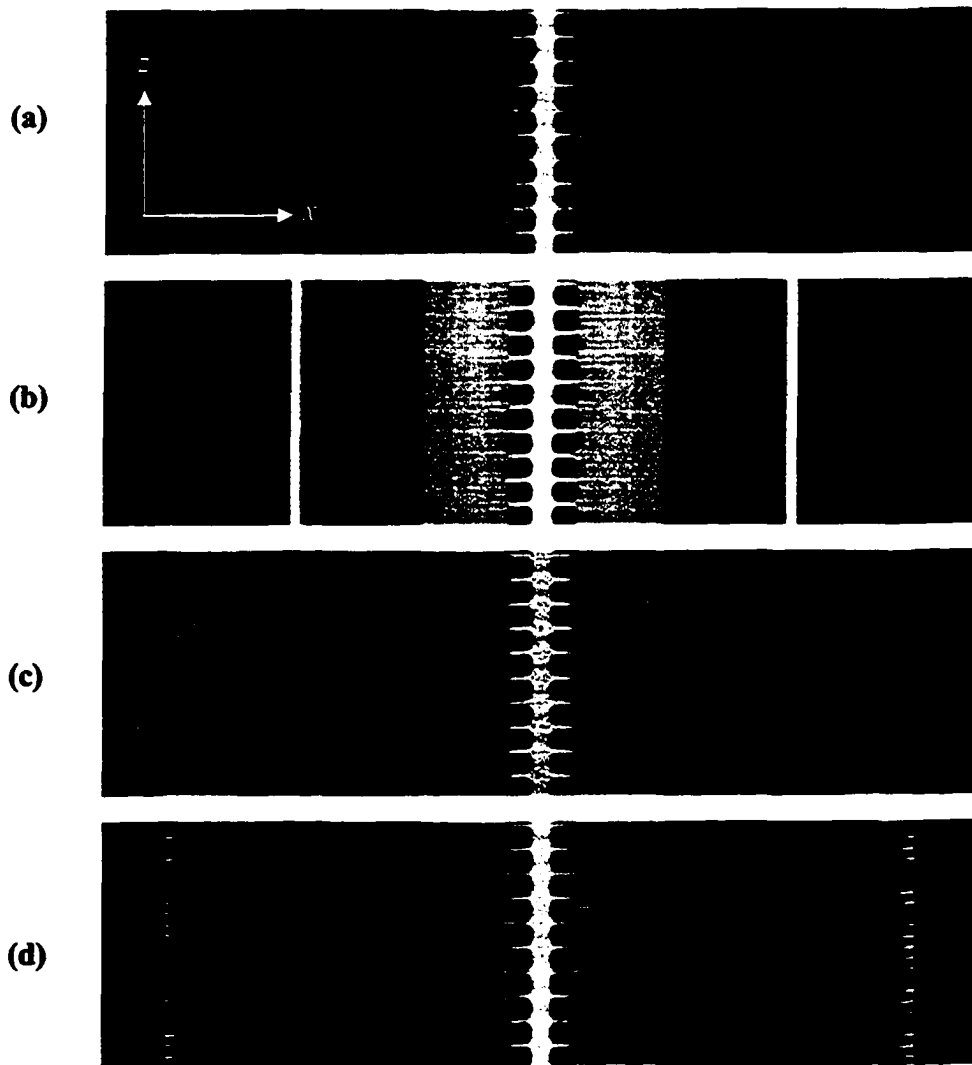


Figure 4-18 – Coronal slices of merged images at a pitch of 1.5. (a) Reference image. (b) Truncated image, 20 cm field-of-view (FOV). (c) Merged image,  $\pm 5.93$  cm offset, 20 cm FOV. (d) Augmented image, 20 cm FOV. Images are displayed using window of 400 and a level of 1000.

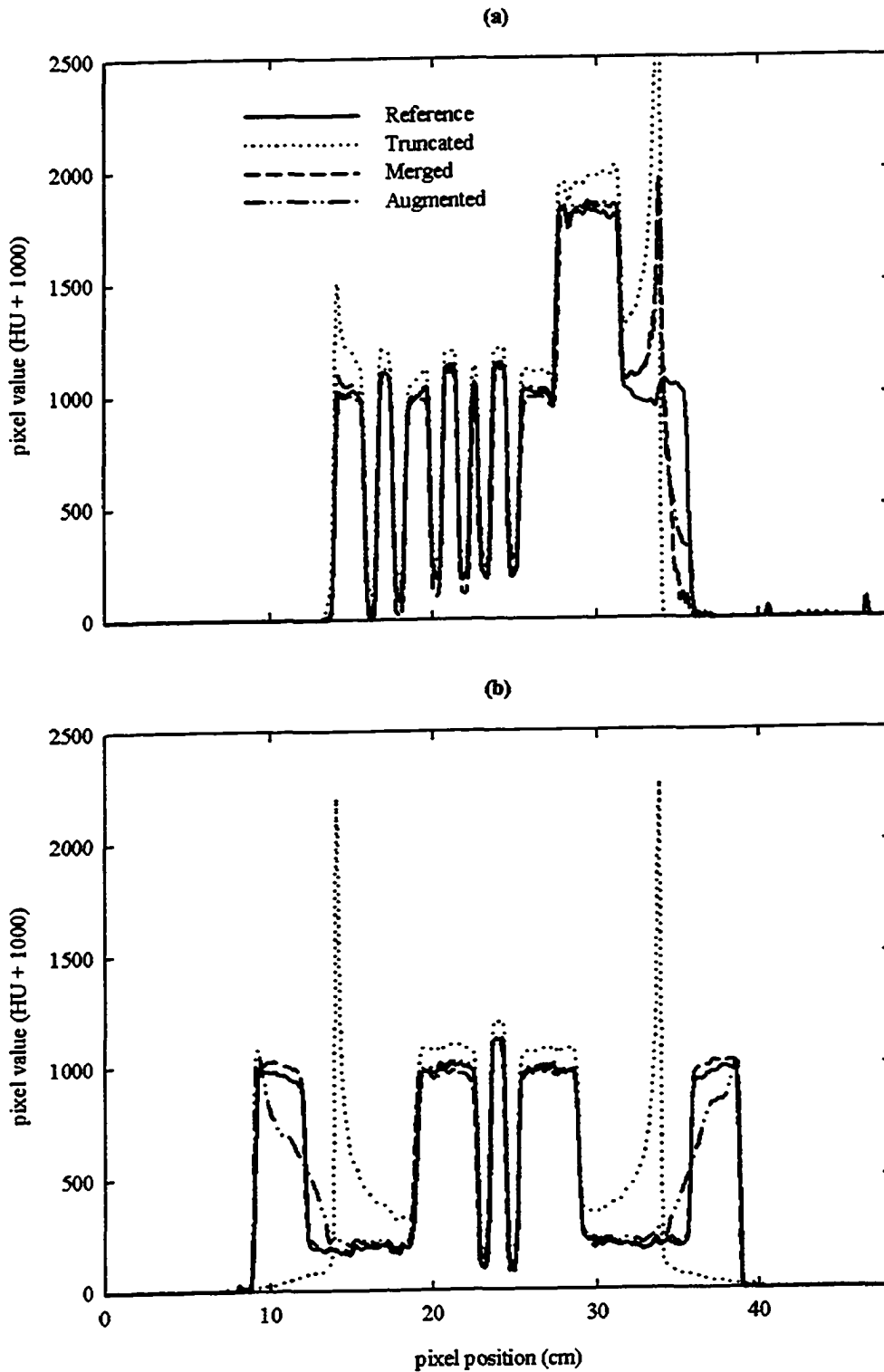


Figure 4-19 – Profiles through (a) sagittal and (b) coronal slices for each image type: reference, truncated, merged, and augmented, at a pitch of 1.5. Profile locations are illustrated in Figure 4-20.



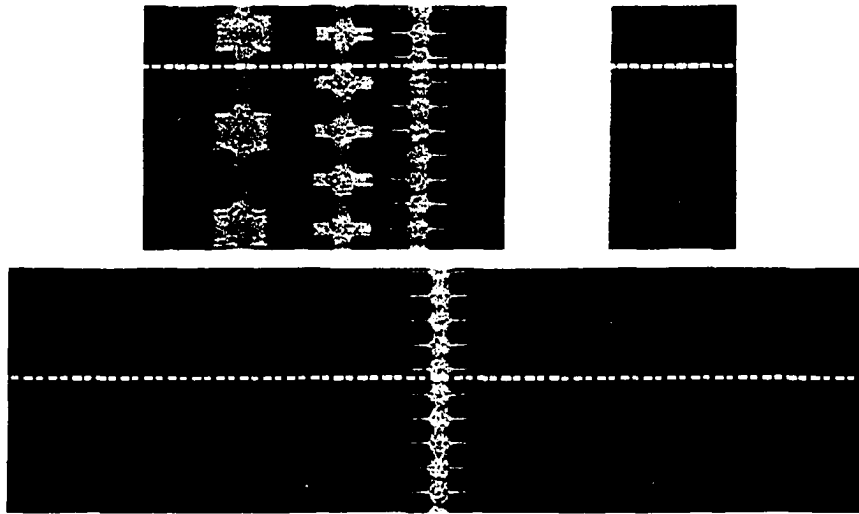


Figure 4-20 – Profiles in Figure 4-19 are taken at line  $z = 25$  and  $z = 46$  for sagittal and coronal slices, respectively.

Table 4-2 – The goodness-of-fit (GOF) and Bias measures for sagittal and coronal slices: truncated, merged, and augmented, at each pitch. The measures are calculated in a 19.5 cm wide x 10 cm high rectangular defined region, which is centered in the image.

**Sagittal Slices**

Pitch	Truncated		Merged		Augmented	
	GOF	Bias	GOF	Bias	GOF	Bias
2	0.270	0.270	0.089	0.039	0.047	0.047
1.5	0.271	0.271	0.082	0.022	0.048	0.048
1	0.267	0.267	0.093	0.036	0.047	0.047

**Coronal Slices**

Pitch	Truncated		Merged		Augmented	
	GOF	Bias	GOF	Bias	GOF	Bias
2	0.803	0.803	0.065	0.029	0.076	0.076
1.5	0.804	0.804	0.066	0.027	0.078	0.078
1	0.807	0.807	0.071	0.033	0.077	0.077

### 4.3.2 Positioning Error

The sinogram merging technique can reduce or eliminate truncation artifacts and can produce an image with quality comparable to that of a non-truncated image. However, accurate positioning in the both the lateral (or shift direction) and the longitudinal directions is a critical step in obtaining such comparable image quality. Figure 4-21 illustrates the effect of both types of positioning errors on the

merging technique for a pitch of 1.5. Merged images are shown for sagittal and coronal slices with a 20 cm FOV and offset locations of  $\pm 5.93$  cm. The slices shown in Figure 4-21(a) are merged images with minimal positioning error. The offset positions are determined using the cross correlation method and are considered to be accurate within  $\pm 0.05$  cm.

The effect of a lateral positioning error is displayed in Figure 4-21(b). The positioning error in the left spiral fan-beam sinogram is minimal, but the positioning error in the right spiral fan-beam sinogram is 0.2 cm in the  $x$ -direction, where the errors are measured with respect to the cross correlation value. Offset values of +6.13 cm and -5.93 cm for the right and left spiral fan-beam sinograms (rather than +5.93 cm and -5.93 cm) were entered as input parameters into the sinogram merging technique. This 0.2 cm positioning error produces an artifact consisting of horizontal light and dark stripes that are most obvious in the water equivalent structures. The edges of the air spaces in the plug also become uneven and notched.

Figure 4-21(c) displays the effect of a longitudinal positioning error on the merging technique. A 0.2 cm positioning error in the  $z$ -direction is introduced into the right spiral fan-beam sinogram while the error in the left is minimal. The result is a blurring in the longitudinal direction that causes the acrylic spaces to become indistinct in the 0.5 cm spacer plug. This error also results in stripe artifacts similar to those seen with the lateral positioning error.

The image GOF and Bias measures were used to quantify the effect of positioning errors on the sinogram merging technique. Table 4-3 displays the image GOF and Bias values for sagittal and coronal slices at each pitch investigated for: minimal error in both the  $x$ - and  $z$ -directions, 0.2 cm error in the  $x$ -direction, and 0.2 cm error in  $z$ -direction. The measures were calculated using the same criteria as used in Section 4.3.1.2. Both types of positioning error lead to an increase in the GOF values in sagittal and coronal slices compared to the merged images with minimal positioning error.

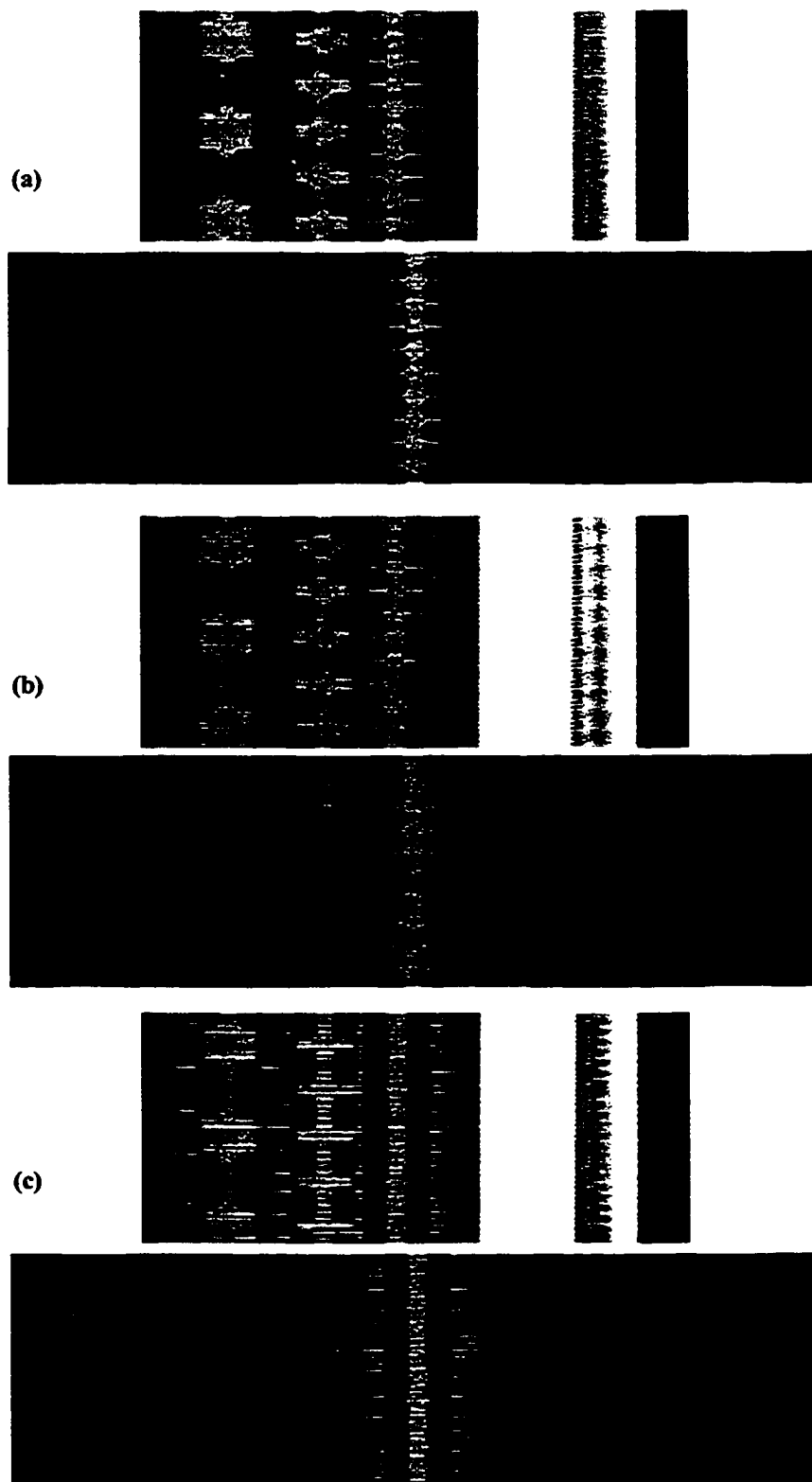


Figure 4-21 – Effect of positioning error in the sinogram merging technique. Sagittal and coronal slices at a pitch of 1.5 for merged images with (a) minimal positioning error,  $\pm 5.93$  cm offset, 20 cm field-of-view (FOV), (b) 0.2 cm lateral error in right scan, and (c) 0.2 cm longitudinal error in right scan. Images are displayed using window of 400 and a level of 1000.

Bias values for sagittal images with  $x$ -direction positioning error are similar to those from images with minimal positioning error. However, Bias values for coronal images with  $x$ -direction error are slightly increased compared to the values for images with minimal error.

GOF and Bias values for sagittal and coronal images with  $z$ -direction positioning error increase as the pitch decreases. At a pitch of 2, the errors due to the longitudinal interpolation of projection values probably mask the 0.2 cm longitudinal positioning error, but as the pitch decreases this positioning error has a greater impact on image quality.

Table 4-3 – The image goodness-of-fit (GOF) and Bias measures for merged sagittal and coronal images with minimal positioning error, 2 mm lateral ( $x$ -direction) error, and 2 mm longitudinal ( $z$ -direction) error. The measures are calculated in a 19.5 cm wide x 10 cm high rectangular defined region, which is centered in the image.

**Sagittal Slices**

Pitch	Merged (minimal error)		Merged ( $x$ error)		Merged ( $z$ error)	
	GOF	Bias	GOF	Bias	GOF	Bias
2	0.089	0.039	0.114	0.034	0.153	0.057
1.5	0.082	0.022	0.114	0.021	0.182	0.095
1	0.093	0.036	0.124	0.028	0.193	0.105

**Coronal Slices**

Pitch	Merged (minimal error)		Merged ( $x$ error)		Merged ( $z$ error)	
	GOF	Bias	GOF	Bias	GOF	Bias
2	0.065	0.029	0.094	0.050	0.092	0.035
1.5	0.066	0.027	0.094	0.050	0.101	0.050
1	0.071	0.033	0.098	0.055	0.115	0.061

## 4.4 General Comments

The iterative sinogram augmentation technique performs well inside the truncated FOV and if viewing this area is all that is required then this technique is sufficient for reducing truncation artifacts. If one requires the image outside the truncated FOV for viewing then the sinogram merging technique can be used. However, this work revealed that accurate positioning of the shifted phantom (error  $\leq \pm 0.05$  cm) is necessary for this technique to perform well. The use of the sagittal lasers for alignment did not provide enough accuracy. The offsets determined by cross correlating non-truncated images led to better merged images; however, this would not be a realistic option in a truly truncated FOV system. To accurately measure the offsets using the cross correlation requires that the images be non-truncated. In our case, these images were available because the projection data acquired from the CT scanner used for experimentation was physically non-truncated.

On a physically truncated system, such as the megavoltage CT in TomoTherapy, non-truncated data would not be available and the positioning accuracy would rely on the sagittal lasers alone. In this work, the laser positioning systems have been shown to be too inaccurate for merging conventional (kV) CT sinograms. The spatial resolution in megavoltage CT is less than in conventional CT, however, and therefore may not require the positioning accuracy to be as high.

Also, scanning at higher pitch tends to hide longitudinal positioning errors. In this work, scans with a 2 mm longitudinal positioning error produced fewer and less severe image artifacts at a pitch of 2 compared to scans at a lower pitch where longitudinal spatial resolution is higher. Hence, the sinogram merging technique may be less sensitive to positioning error when performed on a megavoltage CT system and at a higher pitch. The application of this technique to megavoltage CT needs to be investigated and analyzed.

## References

Gore, J. C. and S. Leeman (1980). "The reconstruction of objects from incomplete projections." Phys Med Biol **25**(1): 129-36.

Noo, F., M. Defrise, R. Clackdoyle and H. Kudo (2002). "Image reconstruction from fan-beam projections on less than a short scan." Phys Med Biol **47**(14): 2525-46.

Ruchala, K. J., G. H. Olivera, J. M. Kapatoes, P. J. Reckwerdt and T. R. Mackie (2002). "Methods for improving limited field-of-view radiotherapy reconstructions using imperfect a priori images." Med Phys **29**(11): 2590-605.

## 5 Conclusions

The aim of this work was to experimentally investigate, using phantom studies, the sinogram merging and the iterative sinogram augmentation technique which are used to reduce truncation artifacts caused by a limited FOV. Experimental sinogram data was collected from a conventional (kV) CT scanner that has a full FOV. The required limited FOV was simulated by the appropriate deletion of projection values. Axial and spiral sinogram data was collected and used to verify the techniques.

Since these techniques require the use of raw sinogram data, it was necessary to gain access to the data and determine the file format. The file format was deduced to allow processing of the data through the various algorithms. The geometrical parameters specific to the scanner were also determined as these are required for the fan-beam to parallel-beam re-binning algorithm.

The problem of reconstructing images from a set of truncated projections using FBP is that the images contain a bowl shaped artifact. In the truncated images, the bowl artifact obscures the anatomy at the edge of the FOV and misrepresents tissue densities inside the FOV. As the FOV decreases, the collected projections are more truncated and the severity of the bowl artifact in the reconstructed image increases.

Images reconstructed from a merged or augmented sinogram show a qualitative and quantitative improvement compared to images reconstructed from a truncated sinogram. The sinogram merging and the iterative sinogram augmentation techniques improve the truncated images by qualitatively reducing the pronounced ring at the periphery of the FOV and quantitatively improving pixel values inside the FOV.

In the sinogram merging technique, the bowl artifact will be removed if the net FOV covers the entire phantom. Hence the FOV circles forming the net FOV should be positioned to cover the full phantom or patient. The technique is very sensitive to positioning error in the shift and longitudinal directions and

requires the user to accurately know the location of the shifted phantom. The effect of the phase angle on the longitudinal resolution could not be investigated due to the limitations of the scanner used in this work. Although a phase angle equal to  $90^\circ$  is suspected to improve the longitudinal resolution, this would be difficult to achieve in practice because the accuracy of the phase angle is determined by the accuracy of the longitudinal positions. Using a couch that permits accurate lateral translations will increase the positioning accuracy of the shifted phantom in both the lateral and longitudinal directions and further reduce artifacts caused by a stationary couch. If lateral translations are accomplished using a translating platform on a stationary couch, the couch artifacts were shown to be reduced if the couch is included in the airscan. The overall benefit of successfully using the sinogram merging technique is that it reduces truncation artifacts by effectively increasing the FOV. The larger net FOV is desirable if structures outside of the truncated FOV need to be visible in the image.

There are, however, several limitations to the sinogram merging technique. Multiple scan procedures reduce the truncation artifacts by increasing the FOV, but result in an increase in procedure time and dose. The FOV is not increased in the direction orthogonal to the shift direction and, depending on the shape of the patient, truncation artifacts may still remain which would require additional scans to reduce. To ensure that the FOV circles completely cover the patient, the overall dimensions of the patient should be known prior to the scan procedure so that the number and location of the scans can be planned.

A major disadvantage of the sinogram merging technique is that it requires the shift locations to be very accurately known. The image quality was significantly degraded with even a small amount of positioning error ( $\geq 0.1$  cm). Hence, accurate positioning is required in both the shift direction and the longitudinal direction. This limitation could be mitigated by using a couch with lateral translation that is, as suggested by this work, accurate to 0.05 cm or less. Even with accurate lateral movement, the success of the technique would require the patient to remain almost motionless during repositioning. The technique is suspected to be less sensitive to positioning errors in megavoltage CT where the



spatial resolution is less than in conventional CT. The impact of longitudinal positioning error (0.2 cm) on the images was shown to be reduced at a higher pitch and this may improve the feasibility of the sinogram merging technique in megavoltage CT imaging. Further investigation needs to be performed in the application of this technique to megavoltage CT.

The iterative sinogram augmentation technique reduces truncation artifacts and improves the quantitative accuracy of the reconstructed image inside the truncated FOV but does not accurately predict structures outside the FOV. The OS-ML-EM algorithm converges quickly and produces good results after only a few iterations. This technique requires the knowledge of patient boundary information for use in the start value model. A uniform mathematical start value model was used in this work, but if this technique was used in TomoTherapy's megavoltage CT then a uniform start value model could be estimated from the outline of an aligned, non-truncated planning CT image.

The benefits of this technique over the sinogram merging technique are that it does not require the collection of additional sinogram data and it can be applied after the scan procedure if improvements to the truncated image are necessary. It does however only improve the image quality inside the truncated FOV whereas the sinogram merging technique improves imaging quality inside an enlarged FOV.

The complementary use of the iterative augmentation technique to the merging technique was also investigated. The merging technique may be used to effectively increase the FOV and the iterative augmentation technique can be subsequently applied to clean up any remaining bowl artifacts in the image.

No text.

# Bibliography

- Anastasio, M. A., D. Shi, X. Pan, C. Pelizzari and P. Munro (2003). "A preliminary investigation of local tomography for megavoltage CT imaging." Med Phys **30**(11): 2969-80.
- Chen, G. H. (2003). "A new framework of image reconstruction from fan beam projections." Med Phys **30**(6): 1151-61.
- Cho, P. S., R. H. Johnson and T. W. Griffin (1995). "Cone-beam CT for radiotherapy applications." Phys Med Biol **40**(11): 1863-83.
- Crawford, C. R., G. T. Gullberg and B. M. Tsui (1988). "Reconstruction for fan beam with an angular-dependent displaced center-of-rotation." Med Phys **15**(1): 67-71.
- Crawford, C. R. and K. F. King (1990). "Computed tomography scanning with simultaneous patient translation." Med Phys **17**(6): 967-82.
- Daube-Witherspoon, M. E. and G. Muehlechner (1986). "An Iterative Image Space Reconstruction Algorithm Suitable for Volume ECT." IEEE Trans Med Imag **MI-5**(2): 61-6.
- De Pierro, A. R. (1987). "On the Convergence of the Iterative Image Space Reconstruction Algorithm for Volume ECT." IEEE Trans Med Imag **MI-6**(2): 174-75.
- Faridani, A., D. Finch, E. Ritman and K. Smith (1997). "Local tomography II." J Appl Math **57**(4): 1095-127.
- Faridani, A., E. Ritman and K. Smith (1992). "Local tomography." J Appl Math **52**(2): 459-84.
- Feldkamp, L. A., L. C. Davis and J. W. Kress (1984). "Practical cone-beam algorithm." J Opt Soc Am **1**: 612-9.
- Gore, J. C. and S. Leeman (1980). "The reconstruction of objects from incomplete projections." Phys Med Biol **25**(1): 129-36.
- Herman, G. T. and R. M. Lewitt (1981). "Evaluation of a preprocessing algorithm for truncated CT projections." J Comput Assist Tomogr **5**(1): 127-35.

Hooper, H. R. and B. G. Fallone (2002). "Technical note: Sinogram merging to compensate for truncation of projection data in tomotherapy imaging." Med Phys **29**(11): 2548-51.

Hooper, H. R. and B. G. Fallone (2003). An Iterative Procedure to Reduce Truncation Artifacts in Tomotherapy Imaging - A Simulation Study. Alberta Cancer Board Annual Research Meeting, Banff, Alberta.

Hsieh, J., E. Chao, J. Thibault, B. Grekowicz, A. Horst, S. McOlash and T. J. Myers (2004). "A novel reconstruction algorithm to extend the CT scan field-of-view." Med Phys **31**(9): 2385-91.

Huang, S. C., M. E. Phelps and E. J. Hoffman (1977). Effect of out-of-field objects in transaxial reconstruction tomography. Reconstruction Tomography in Diagnostic Radiology and Nuclear Medicine. M. M. Ter-Pogossian, M. E. Phelps, G. L. Brownell, J. R. Cox, D. O. Davis and R. G. Evens. Baltimore, University Park Press.

Hudson, H. M. and R. S. Larkin (1994). "Accelerated Image Reconstruction Using Ordered Subsets of Projection Data." IEEE Trans Med Imag **13**(4): 601-9.

Kak, A. C. (1979). "Computerized tomography with x-ray emission and ultrasound sources." Proc IEEE **67**: 1245-72.

Kak, A. C. and M. Slaney (1987). Principles of Computerized Tomographic Imaging. New York, IEEE Press.

Kalender, W. A. and A. Polacin (1991). "Physical performance characteristics of spiral CT scanning." Med Phys **18**(5): 910-5.

Kalender, W. A., W. Seissler, E. Klotz and P. Vock (1990). "Spiral volumetric CT with single-breath-hold technique, continuous transport, and continuous scanner rotation." Radiology **176**(1): 181-3.

Kapatoes, J. M., G. H. Olivera, P. J. Reckwerdt, E. E. Fitchard, E. A. Schloesser and T. R. Mackie (1999). "Delivery verification in sequential and helical tomotherapy." Phys Med Biol **44**(7): 1815-41.

Kapatoes, J. M., G. H. Olivera, K. J. Ruchala, J. B. Smilowitz, P. J. Reckwerdt and T. R. Mackie (2001). "A feasible method for clinical delivery verification and dose reconstruction in tomotherapy." Med Phys **28**(4): 528-42.

Karp, J. S., G. Muehllehner and R. M. Lewitt (1988). "Constrained Fourier Space Method for Compensation of Missing Data in Emission Computed Tomography." IEEE Trans Med Imag **7**(1): 21-5.

Kim, J. H., K. Y. Kwak, S. B. Park and Z. H. Cho (1985). "Projection Space Iteration Reconstruction-Reprojection." IEEE Trans Med Imag **MI-4**(3): 139-43.

Lange, K. and R. Carson (1984). "EM reconstruction algorithms for emission and transmission tomography." J Comput Assist Tomogr **8**(2): 306-16.

Lewitt, R. M. (1979). "Processing of incomplete measurement data in computed tomography." Med Phys **6**(5): 412-7.

McDavid, W. D., R. G. Waggener, W. H. Payne and M. J. Dennis (1977). "Correction for spectral artifacts in cross-sectional reconstruction from x rays." Med Phys **4**(1): 54-7.

McLachlan, G. J. and T. Krishnan (1997). The EM Algorithm and Extensions. New York, John Wiley & Sons, Inc.

Medoff, B. P., W. R. Brody, M. Nassi and A. Macovski (1983). "Iterative Convolution Backprojection Algorithms for Image Reconstruction from Limited Data." J Opt Soc Am **73**(11): 1493-500.

Midgley, S., R. M. Millar and J. Dudson (1998). "A feasibility study for megavoltage cone beam CT using a commercial EPID." Phys Med Biol **43**(1): 155-69.

Nalcioğlu, O., P. V. Sankar and J. Sklansky (1979). "Region-of-interest x-ray tomography (ROIT)." SPIE **206**: 98-102.

Noo, F., M. Defrise, R. Clackdoyle and H. Kudo (2002). "Image reconstruction from fan-beam projections on less than a short scan." Phys Med Biol **47**(14): 2525-46.

Nuyts, J., B. De Man, P. Dupont, M. Defrise, P. Suetens and L. Mortelmans (1998). "Iterative reconstruction for helical CT: a simulation study." Phys Med Biol **43**(4): 729-37.

Ohnesorge, B., T. Flohr, K. Schwarz, J. P. Heiken and K. T. Bae (2000). "Efficient correction for CT image artifacts caused by objects extending outside the scan field of view." Med Phys **27**(1): 39-46.

Ollinger, J. M. and J. S. Karp (1988). "An Evaluation of Three Algorithms for Reconstructing Images from Data with Missing Projections." IEEE Trans Nucl Sci **35**(1): 629-34.

- Oppenheim, B. E. (1977). Reconstruction Tomography from Incomplete Projections. Reconstruction Tomography in Diagnostic Radiology and Nuclear Medicine. M. M. Ter-Pogossian, M. E. Phelps, G. L. Brownell, J. R. Cox, D. O. Davis and R. G. Evens. Baltimore, University Park Press.
- Pan, S. X. and A. C. Kak (1983). "A computational study of reconstruction algorithms for diffraction tomography: Interpolation vs. filtered-backpropagation." IEEE Trans Acoust Speech Signal Processing ASSP-31: 1262-75.
- Parker, D. L. (1982). "Optimal short scan convolution reconstruction for fanbeam CT." Med Phys 9(2): 254-7.
- Polacin, A., W. A. Kalender and G. Marchal (1992). "Evaluation of section sensitivity profiles and image noise in spiral CT." Radiology 185(1): 29-35.
- Radon, J. (1917). "Über die Bestimmung von Funktionen durch ihre Integralwerte längs gewisser Mannigfaltigkeiten." Berichte über die Verhandlungen der Sächsischen Akademien der Wissenschaften, Leipzig. Mathematisch-physische Klasse 69: 262-7.
- Redpath, A. T. and T. M. Kehoe (1999). Simulator Computed Tomography. The Modern Technology of Radiation Oncology. J. Van Dyk. Madison, Medical Physics Publishing.
- Ruchala, K. J., G. H. Olivera and J. M. Kapatoes (2002a). "Limited-data image registration for radiotherapy positioning and verification." Int J Radiat Oncol Biol Phys 54(2): 592-605.
- Ruchala, K. J., G. H. Olivera, J. M. Kapatoes, P. J. Reckwerdt and T. R. Mackie (2002b). "Methods for improving limited field-of-view radiotherapy reconstructions using imperfect a priori images." Med Phys 29(11): 2590-605.
- Ruchala, K. J., G. H. Olivera, E. A. Schloesser and T. R. Mackie (1999). "Megavoltage CT on a tomotherapy system." Phys Med Biol 44(10): 2597-621.
- Sankar, P. V., O. Nalcioglu and J. Sklansky (1983). "Undersampling Errors in Region-of-Interest Tomography." IEEE Trans Med Imag MI-1(3): 168-73.
- Sato, T., S. J. Norton, M. Linzer, O. Ikeda and M. Hirama (1981). "Tomographic image reconstruction from limited projections using iterative revisions in image and transform spaces." Appl Opt 20(3): 395-99.
- Shepp, L. A. and Y. Vardi (1982). "Maximum Likelihood Reconstruction for Emission Tomography." IEEE Trans Med Imag MI-1(2): 113-123.

Siltanen, S., V. Kolehmainen, S. Jarvenpaa, J. P. Kaipio, P. Koistinen, M. Lassas, J. Pirttila and E. Somersalo (2003). "Statistical inversion for medical x-ray tomography with few radiographs: I. General theory." Phys Med Biol **48**(10): 1437-63.

Stark, H., J. W. Woods, I. Paul and R. Hingorani (1981). "An investigation of computerized tomography by direct Fourier inversion and optimum interpolation." IEEE Trans Biomed Eng **28**(7): 496-505.

Swindell, W. and S. Webb (1988). X-ray Transmission Computed Tomography. The Physics of Medical Imaging. S. Webb. Bristol, Institute of Physics Publishing.

Tam, K. C., J. W. Eberhard and K. W. Mitchell (1990). "Incomplete-Data CT Image Reconstructions in Industrial Applications." IEEE Trans Nucl Sci **37**(3): 1490-99.

Tam, K. C. and V. Perez-Mendez (1981a). "Tomographical imaging with limited-angle input." J Opt Soc Am **71**(5): 582-92.

Tam, K. C. and V. Perez-Mendez (1981b). "Limited-angle three-dimensional reconstructions using Fourier transform iterations and Radon transform iterations." Opt Eng **20**(4): 586-89.

Titterington, D. M. (1987). "On the Iterative Image Space Reconstruction Algorithm for ECT." IEEE Trans Med Imag **MI-6**(1): 52-6.

Tofts, P. S. and J. C. Gore (1980). "Some sources of artefact in computed tomography." Phys Med Biol **25**(1): 117-27.

Van Dyk, J. and J. S. Taylor (1999). CT Simulators. The Modern Technology of Radiation Oncology. J. Van Dyk. Madison, Medical Physics Publishing.

Wagner, W. (1979). "Reconstructions from restricted region scan data - new means to reduce the patient dose." IEEE Trans Nucl Sci **NS-26**(2): 2866-9.

Walden, J. (2000). "Analysis of the direct Fourier method for computer tomography." IEEE Trans Med Imaging **19**(3): 211-22.

Wang, G. and M. W. Vannier (1994). "Longitudinal resolution in volumetric x-ray computerized tomography--analytical comparison between conventional and helical computerized tomography." Med Phys **21**(3): 429-33.

Yen, S. Y., C. H. Yan, G. D. Rubin and S. Napel (1999). "Longitudinal sampling and aliasing in spiral CT." IEEE Trans Med Imaging **18**(1): 43-58.